DOKUZ EYLÜL UNIVERSITY
GRADUATE SCHOOL OF NATURAL AND APPLIED SCIENCES

DESIGN AND IMPLEMENTATION OF A MEASUREMENT SYSTEM TO MEASURE RESIDUAL STRESS IN ALUMINUM CASTED VEHICLE PARTS

Onur ÖZAYDIN

February, 2026

İZMİR

DESIGN AND IMPLEMENTATION OF A MEASUREMENT SYSTEM TO MEASURE RESIDUAL STRESS IN ALUMINUM CASTED VEHICLE PARTS

A Thesis Submitted to the
Graduate School of Natural and Applied Sciences of Dokuz Eylül University
In Partial Fulfillment of the Requirements for the Degree of Doctor of Philosophy in Department of Mechanical Engineering, Machine Theory and Dynamics Program

by

Onur ÖZAYDIN

February, 2026

İZMİR

Ph.D. THESIS EXAMINATION RESULT FORM

We have read the thesis entitled **"DESIGN AND IMPLEMENTATION OF A MEASUREMENT SYSTEM TO MEASURE RESIDUAL STRESS IN ALUMINUM CASTED VEHICLE PARTS "** completed by **ONUR ÖZAYDIN** under supervision of **ASSOC.PROF.DR. AYTAÇ GÖREN** and we certify that in our opinion it is fully adequate, in scope and in quality, as a thesis for the degree of Doctor of Philosophy.

Assoc.Prof.Dr. AYTAÇ GÖREN

Supervisor

Assoc. Prof. Dr. Esra DOKUMACI ALKAN

Thesis Committee Member

Assoc. Prof. Dr. Gökçe Mehmet GENÇER

Thesis Committee Member

Prof. Dr. Kutlay SEVER

Examining Committee Member

Assoc. Prof. Dr. Gözde SARI

Examining Committee Member

Prof. Dr. Abdullah SEÇGİN

Director

Graduate School of Natural and Applied Sciences

ACKNOWLEDGMENT

First and foremost, I would like to express my sincere thankfulness to my supervisor, Assoc. Prof. Dr. Aytaç GÖREN, for giving me the opportunity to carry out this study and for his continuous support throughout every stage of my doctoral research. I am deeply thankful for the trust he placed in me and for his inspiring guidance at every step of this journey. I am truly grateful for the opportunity to learn from him, not only through his technical expertise but also through his exemplary character.

I would also like to thank the members of my doctoral thesis committee, Assoc. Prof. Dr. Esra DOKUMACI ALKAN and Assoc. Prof. Dr. Gökçe Mehmet GENÇER, for their valuable contributions to the direction and improvement of this study.

I am sincerely grateful to Mert KİP for his continuous support during the experimental stages of my thesis, as well as to the members of DEU ACRL— A. Batuhan GÜNALTAY, Mert İZCİ, and İ. Samed BATMAZ — and to all members of DEU ACRL and Solar Team Solaris for their contributions and teamwork.

I would also like to thank my colleagues A. Yiğit KAYA, S. Fatih KIRMIZIGÖL, T. Batuhan KORKUT, and Y. Nur AYDIN. Although we work under different organizations, I am confident that we will always remain a team.

I would like to thank Döktaş Dökümcülük Tic. ve San. A.Ş. and Yiğit ÇATAL, as well as to BİAS Engineering and Hüseyin FIRTINA for their technical support and another special thanks to Snapmaker for their memorable support to DEÜ ACRL.

My heartfelt thanks go to my beloved wife, Elif ÖZAYDIN, whose unconditional love has always been with me, whether near or far. I consider myself truly fortunate to have you as the light of my life and the greatest source of my strength.

Finally, I am deeply grateful to my sister Sevil ÖZAYDIN, my mother Emel ÖZAYDIN, and my father Osman ÖZAYDIN, who have always believed in me and supported me at every stage of my life. I owe them more than words can express.

Onur ÖZAYDIN

DESIGN AND IMPLEMENTATION OF A MEASUREMENT SYSTEM TO MEASURE RESIDUAL STRESS IN ALUMINUM CASTED VEHICLE PARTS

ABSTRACT

This study investigates the influence of casting and heat treatment processes on the microstructure, mechanical properties, and residual stress development in AlSi11Mg aluminum alloy wheels produced via low-pressure die casting (LPDC). The research aims to optimize wheel manufacturing processes to enhance mechanical performance, minimize residual stress-induced failures, and ensure compliance with industrial and automotive standards.

The study employed a comprehensive methodology encompassing material characterization, experimental testing, and numerical simulations. The chemical composition of the AlSi11Mg alloy was verified using optical emission spectroscopy (OES), confirming compliance with both literature-reported limits and industry specifications. Macrostructural analysis revealed uniform grain distribution, while microstructural evaluation demonstrated a transformation from coarse dendritic structures in as-cast wheels to refined and spheroidized silicon particles after T6 heat treatment. These microstructural changes directly influenced the mechanical behavior of the alloy.

Mechanical testing, including tensile and Brinell hardness measurements, was performed on critical wheel regions, such as the inner flange, outer flange, and spoke. Results indicated that as-cast wheels exhibited the lowest ultimate tensile strength, yield strength, and hardness, whereas T6-treated wheels showed significant improvements. Among the heat treatment variations, T6 treatment with 120 minutes of artificial aging provided the most balanced combination of strength, hardness, and elongation. Partially aged wheels exhibited moderate improvements, while as-cast wheels remained relatively weak. These findings highlight the importance of controlled heat treatment in achieving optimal mechanical performance.

Residual stress evaluation combined numerical simulations using the Magmastress module of Magmasoft with experimental hole drilling methods. Analytical and experimental results consistently showed that T6-treated wheels developed higher residual stresses following quenching, which were partially relieved during artificial aging. The hub and hub–spoke regions emerged as critical zones with higher stress concentration, emphasizing the need for targeted stress-relief strategies. Stress-relief annealing and optimized aging were effective in reducing residual stresses, improving component durability without compromising mechanical properties.

Overall, this research establishes a clear link between casting parameters, heat treatment schedules, microstructural evolution, mechanical performance, and residual stress development. The study provides practical guidelines for optimizing wheel production, ensuring safety, reliability, and performance in automotive applications. Future work may include evaluating alternative alloy compositions, full-field residual stress mapping, predictive modeling, and in-service performance assessment under operational conditions. The findings contribute to both academic understanding and industrial practice, advancing the knowledge of aluminum wheel manufacturing and heat treatment optimization.

Keywords: AlSi11Mg alloy, low-pressure die casting, heat treatment, residual stress, mechanical properties, microstructure, T6 treatment

ALÜMİNYUM DÖKÜM ARAÇ PARÇALARINDA KALINTI GERİLMEYİ ÖLÇMEK İÇİN BİR ÖLÇÜM SİSTEMİNİN TASARIMI VE UYGULAMASI

ÖZ

Bu doktora çalışması, alçak basınçlı döküm (LPDC) yöntemiyle üretilen AlSi11Mg alüminyum alaşımlı jantlarda döküm ve ısıl işlem süreçlerinin mikro yapı, mekanik özellikler ve kalıntı gerilmeler üzerindeki etkilerini incelemektedir. Çalışmanın amacı, jant üretim süreçlerini optimize ederek mekanik performansı artırmak, kalıntı gerilmelerden kaynaklanan arızaları en aza indirmek ve endüstriyel ile otomotiv standartlarına uyumu sağlamaktır.

Araştırma, malzeme karakterizasyonu, deneysel testler ve sayısal simülasyonları kapsayan kapsamlı bir metodoloji ile yürütülmüştür. AlSi11Mg alaşımının kimyasal bileşimi, optik emisyon spektroskopisi (OES) ile doğrulanmış ve literatürde belirtilen sınırlar ile endüstri spesifikasyonlarına uygunluğu tespit edilmiştir. Makroyapı analizleri, tanelerin homojen dağılımını ortaya koyarken, mikroyapı incelemeleri, as-cast jantlarda görülen kaba dendritik yapıların T6 ısıl işlem sonrası daha ince ve spheroidize Si parçacıklarına dönüştüğünü göstermiştir. Bu mikro yapısal değişimler, alaşımın mekanik davranışını doğrudan etkilemiştir.

Çekme ve Brinell sertlik testleri, jantın kritik bölgeleri olan iç flanş, dış flanş ve spoke bölgelerinde gerçekleştirilmiştir. Sonuçlar, döküm sonrası jantların en düşük çekme dayanımı, akma dayanımı ve sertliğe sahip olduğunu, T6 işlem görmüş jantların ise belirgin iyileşmeler gösterdiğini ortaya koymuştur. Isıl işlem varyasyonları arasında, 120 dakikalık yapay yaşlandırma uygulanan T6, en dengeli kombinasyon olan dayanım, sertlik ve uzama değerlerini sağlamıştır. Kısmi yaşlandırma uygulanan jantlar orta düzeyde iyileşme gösterirken, döküm sonrası jantlar göreceli olarak zayıf kalmıştır. Bu bulgular, kontrollü ısıl işlemin optimal mekanik performans için önemini vurgulamaktadır.

Kalıntı gerilme değerlendirmesi, Magmastress modülü ile sayısal simülasyonlar ve deneysel delik delme yöntemini birleştirerek yapılmıştır. Analitik ve deneysel

sonuçlar, T6 işlemli jantlarda quenching sonrası daha yüksek kalıntı gerilmelerin oluştuğunu, yapay yaşlandırma sırasında ise kısmen rahatladığını göstermiştir. Göbek ve göbek–kol bölgeleri, yüksek gerilme yoğunluğu oluşan kritik alanlar olarak öne çıkmış ve hedefli gerilme giderme stratejilerinin önemini vurgulamıştır. Gerilme giderme tavlaması ve optimize edilmiş yaşlandırma, mekanik özellikleri koruyarak kalıntı gerilmeleri azaltmada etkili olmuştur.

Sonuç olarak, bu araştırma döküm parametreleri, ısıl işlem koşulları, mikro yapı değişimi, mekanik performans ve kalıntı gerilmeler arasında açık bir ilişki ortaya koymaktadır. Çalışma, jant üretimini optimize etmeye yönelik pratik rehberler sunmakta, otomotiv uygulamalarında güvenlik, dayanıklılık ve performansı artırmaktadır. Gelecek çalışmalar, alternatif alaşım kompozisyonları, tam alan kalıntı gerilme ölçümleri, öngörücü modelleme ve operasyonel koşullarda performans değerlendirmelerini içerebilir. Bu bulgular, hem akademik bilgi birikimine hem de endüstriyel uygulamalara katkı sağlamaktadır.

Anahtar kelimeler: AlSi11Mg alaşımı, düşük basınçlı döküm, ısıl işlem, kalıntı gerilme, mekanik özellikler, mikro yapı, T6 işlemi

CONTENTS

Page

Ph.D. THESIS EXAMINATION RESULT FORM ii
ACKNOWLEDGMENT iii
ABSTRACT iv
ÖZ vi
CONTENTS viii
LIST OF FIGURES xi
LIST OF TABLES xvi
ABBREVIATIONS xvii
LIST OF SYMBOLS xviii

CHAPTER ONE - INTRODUCTION 1

1.1 Overview 1
1.2 Motivation 1
1.3 Aims and Objectives 3
1.4 Originality of the Research 3
1.5 Structure of Thesis 4

CHAPTER TWO - PREVIOUS STUDIES 5

2.1 Historical Background 5
2.2 State of the Art and Literature Review 15
2.2.1 Aluminum Alloys and Heat Treatment 16
2.2.2 Residual Stress and Measurement Methods 23

CHAPTER THREE - MATERIALS AND METHODS 36

3.1 Materials 36
3.2 Methods 43
3.2.1 Casting 44
3.2.1.1 Melting 45
3.2.1.2 Low Pressure Die Casting 49

3.2.1.3 Heat Treatment Process 55
3.2.1.4 Machining 56
3.2.1.5 Coating 58
3.2.2 Heat Treatment 59
3.2.3 Residual Stress Measurement System 62
3.2.3.1 Destructive Measurement Techniques 64
3.2.3.1.1 Hole Drilling Method 65
3.2.3.1.2 Ring-Core Method 69
3.2.3.1.3 Deep Hole Drilling Method 70
3.2.3.1.4 Contour Method 70
3.2.3.1.5 Sectioning Method 71
3.2.3.2 Non-Destructive Measurement Techniques 72
3.2.3.2.1 XRD: X-Ray Diffraction Method 72
3.2.3.2.2 Ultrasonic Method 74
3.2.3.2.3 Neutron Diffraction Method 74
3.2.3.3 Analytical Techniques 74

CHAPTER FOUR - EXPERIMENTAL STUDY 78

4.1 Material and Casting 79
4.2 Heat Treatment Applications 83
4.3 Residual Stress Calculation and Measurement 85
4.3.1 Residual Stress Calculation: Analytical Technique and Simulations . 86
4.3.2 Residual Stress Measurement: Hole Drilling Method on Aluminum Cast Parts 90
4.3.2.1 Gravity-Cast Preliminary Specimens 91
4.3.2.2 Low-Pressure Cast Wheel Specimens 100
4.3.2.3 Data Acquisition System 105

CHAPTER FIVE - RESULTS AND DISCUSSION 108

5.1 Material and Heat Treatment Results 109
5.1.1 Chemical Analysis Results 109
5.1.2 Microstructure and Macrostructure 110

5.1.3 Hardness and Tensile Test Results 113
5.2 Residual Stress Results 120
5.2.1 Analytical Method Results 120
5.2.2 Hole Drilling Method Results 128

CHAPTER SIX - CONCLUSIONS 142

REFERENCES 146

LIST OF FIGURES

Page

Figure 1.1 Structure of thesis 4

Figure 3.1 The aluminum-silicon phase diagram (Askeland et al., 2011) 37

Figure 3.2 Microstructures of AlSi11 a) As-cast 150X, (b) As-cast 750X (c) As-cast modified, 150X (b) As-cast modified, 1200X (Warmuzek, 2015) 38

Figure 3.3 Aluminum alloy wheel production process flowchart 45

Figure 3.4 Mold sample for aluminum alloy wheel (Aydın et al., 2021) 50

Figure 3.5 Illustration of the low pressure die casting process (Duan, 2016) 51

Figure 3.6 Low-pressure die casting machine (Özaydın, 2019) 52

Figure 3.7 Example of a heat treatment facility (Özaydın, 2019) 56

Figure 3.8 Schematic view of Helium leakage test (Grubisic, 2017) 57

Figure 3.9 Typical geometry of a rosette (Akbari et al., 2014) 65

Figure 3.10 Schematic view of hole drilling method (Özaydın et al., 2025) 66

Figure 3.11 Hole drilling rosettes (ASTM, 2020) 66

Figure 3.12 Schematic view of the ring-core method (Özaydın et al., 2025) 69

Figure 3.13 Schematic cross-section of the ring-core method (Özaydın et al., 2025) 69

Figure 3.14 Schematic view of an I-Profile in the sectioning method (Özaydın et al., 2025) 71

Figure 3.15 Detailed schematic view of an I-Profile in the sectioning method (Özaydın et al., 2025) 72

Figure 3.16 The x-ray spectrometer (Cullity & Stock, 2014) 73

Figure 4.1 Gravity-cast preliminary specimens (Personal archive, 2026) 80

Figure 4.2 Low-pressure as-cast wheel specimen - Option #1 (Personal archive, 2026) 81

Figure 4.3 Inner flange, outer flange and spoke on cross-section of wheel 82

Figure 4.4 Gravity-cast preliminary specimens with different cooling conditions (Personal archive, 2026) 83

Figure 4.5 Low-pressure T6 heat treated wheel specimens - Option #2, #3, #4 (Personal archive, 2026) 84

Figure 4.6 Low-pressure artificial aged wheel - Option #5 (Personal archive, 2026) 84

Figure 4.7 Casting simulation process steps (Özaydın, 2019) 87

Figure 4.8 Results definition in Magmasoft software - Magmastress module (Özaydın, 2019) 89

Figure 4.9 Gravity-cast preliminary specimens (Personal archive, 2026) 93

Figure 4.10 Surface preparation (Personal archive, 2026) 93

Figure 4.11 Surface-prepared (top left) and non–surface-prepared (bottom right) specimen (Personal archive, 2026) 94

Figure 4.12 Uniaxial strain gauges (Personal archive, 2026) 95

Figure 4.13 Snapmaker Artisan 3-in-1 device (Snapmaker, n.d.) 95

Figure 4.14 Primary experimental set-up for machining parameters (4 Samples + 1 Dummy) (Personal archive, 2026) 96

Figure 4.15 Snapmaker Artisan 3-in-1 machine with CNC Module (Personal archive, 2026) 96

Figure 4.16 Temperature measurement after trial machining (Personal archive, 2026) 97

Figure 4.17 Machining Plan #1: Cutting speed 18000 rpm and feed rate 0.2 mm/min (Personal archive, 2026) 98

Figure 4.18 Gravity Specimen #5 is added to measure (Personal archive, 2026) 99

Figure 4.19 Gravity Specimen #6 and #7 (Personal archive, 2026) 100

Figure 4.20 Rosette strain gauge -Vishay, CEA-06-062UM-120 (Personal archive, 2026)..... 101

Figure 4.21 Prepared surface area for rosette strain gauges (Personal archive, 2026) 101

Figure 4.22 Rosette strain gauge on the wheel (Personal archive, 2026) 102

Figure 4.23 Strain gauge terminal near the rosette strain gauges (Personal archive, 2026)..... 103

Figure 4.24 Wiring of rosette strain gauge on the wheel (Personal archive, 2026). 103

Figure 4.25 Mounting the wheel on the lab scale CNC machine (Personal archive, 2026)..... 104

Figure 4.26 Positioning the drilling head onto the rosette strain gauge (Personal archive, 2026)..... 104

Figure 4.27 After hole drilling process (Personal archive, 2026)..... 105

Figure 4.28 Wheatstone bridge (Kip et al., 2025)..... 106

Figure 4.29 The wiring diagram of the measuring system (Kip et al., 2025)..... 107

Figure 5.1 Macrostructure of wheel cross-section and regions (Personal archive, 2026) 110

Figure 5.2 Results of UTS [MPa], YS [MPa] and Elongation [%]..... 115

Figure 5.3 Results of Hardness Brinell [HB]..... 117

Figure 5.4 Results of Ultimate Tensile Strength (UTS) [MPa] 117

Figure 5.5 Results of Yield Strength (YS) [MPa]..... 118

Figure 5.6 Results of Elongation [%]..... 118

Figure 5.7 Suspected hub & hub/spoke area for cracks (Personal archive, 2026)... 121

Figure 5.8 The effect of handling process on residual stress (Option #1) 122

Figure 5.9 The results of Option #2 on various steps (a)After solution treatment, (b)After quenching, (c)After aging. 124

Figure 5.10 The results of Option #4 on various steps (a) After solution treatment, (b)After quenching, (c)After aging. 125

Figure 5.11 The results of Option #5 after stress relief annealing 128

Figure 5.12 Gravity Specimen No.1 - Cutting Speed: 18000 rpm - Feed Rate: 0.2 mm/min 131

Figure 5.13 Gravity Specimen No.2 - Cutting Speed: 18000 rpm - Feed Rate: 0.3 mm/min 131

Figure 5.14 Gravity Specimen No.3 - Cutting Speed: 12000 rpm - Feed Rate: 0.2 mm/min 132

Figure 5.15 Gravity Specimen No.4 - Cutting Speed: 12000 rpm - Feed Rate: 0.3 mm/min 132

Figure 5.16 Gravity Specimen No.5 - Cutting Speed: 18000 rpm - Feed Rate: 0.2 mm/min 133

Figure 5.17 Comparing Gravity Specimen No.1 (Air Cooling)–No.5 (Water Cooling)–Uniaxial SG 134

Figure 5.18 Comparing Gravity Specimen No.6 (Air Cooling)–No.7 (Water Cooling)–Rosette SG 135

Figure 5.19 Vout / time for as cast wheel 137

Figure 5.20 Vout / time for T6 wheel 137

Figure 5.21 Vout / time for artificial aged wheel 138

Figure 5.22 Residual Stress / depth for as cast wheel 138

Figure 5.23 Residual Stress / depth for T6 wheel 139

Figure 5.24 Residual Stress / depth for artificial aged wheel 139

Figure 5.25 Comparing all wheels 140

LIST OF TABLES

Page

Table 3.1 Chemical Composition of AlSi11Mg Aluminum Alloy (Rheinfelden Alloys, 2016)..... 39

Table 3.2 Mechanical Properties of AlSi11Mg Aluminum Alloy (Rheinfelden Alloys, 2016)..... 39

Table 4.1 Heat treatment application 85

Table 4.2 Machining parameters and experimental set ups for gravity-cast preliminary specimens 92

Table 5.1 Chemical Analysis of Cast AlSi11Mg Aluminum Alloy..... 110

Table 5.2 Microstructures of All Options 111

Table 5.3 Mechanical Properties of AlSi11Mg Aluminum Alloy on Different Areas 114

ABBREVIATIONS

CAD : Computer Aided Design

AI : Artificial Intelligence

CAGR : Compound Annual Growth Rate

ECCS : European Convention for Constructional Steelworks

ASTM : American Society for Testing and Materials

SAE : Society of Automotive Engineers

XRD : X-Ray Diffraction

USD : United States Dollar

LPDC : Low Pressure Die Casting

HB : Hardness Brinell

DIC : Digital Image Correlation

FEA : Finite Element Analysis

CMM : Contour Measurement Machine

UK : United Kingdom

CT : Computed Tomography

HTC : Heat Transfer Coefficient

ACRL : Automatic Control and Robotics Labs

ADC : Analog-to-Digital Converter

GF : Gauge Factor

LIST OF SYMBOLS

σ : Stress

ε : Strain

ν : Poisson's Ratio

E : Young Modulus

δ_{ij} : Kronecker delta

V_{ex} : Excitation voltage

V_{out} : Output voltage

R : Electrical resistance of the wire

L : Length of the wire

ρ : Resistivity of the material

A : Cross-sectional area of the wire

ΔR : Change in resistance of the wire

a : radius of the drilled hole

r : distance between the strain gauge and the center of the hole

θ : angle between strain gauge and the direction of the first principal stress

λ : Wavelength

T : Temperature

α : Thermal expansion coefficient

CHAPTER ONE
INTRODUCTION

1.1 Overview

In recent years, the demand for sustainable, accessible, cost-effective, and environmentally conscious materials has been steadily increasing in the manufacturing industry. These demands, combined with technical requirements such as high strength, low weight, ease of manufacturability, and the ability to enhance mechanical properties through heat treatment, have led to the growing prominence of lightweight metals in the automotive, aviation, marine, and defense industries. In this context, aluminum alloys have gained significant importance because of their various applications and their potential for further improvement.

In aluminum casting components, which are widely used in the automotive sector, temperature variations that occur during the casting process and subsequent heat treatments lead to the formation of residual stresses within the material. These stresses can adversely affect the mechanical strength and service life of the component, posing reliability risks during operation. Therefore, accurate measurement and modeling of residual stress is of critical importance for improving production quality and ensuring product reliability.

In this study, various experimental and analytical approaches for determining thermally induced residual stresses in aluminum cast components were investigated, and selected methods were evaluated in detail. The findings are discussed with respect to the origins, effects, and possible mitigation strategies of residual stresses. Ultimately, this study provides a comprehensive perspective on the risks associated with residual stresses formed during production and heat treatment processes in aluminum alloy cast parts used in the automotive industry, along with their areas of influence and potential preventive measures.

1.2 Motivation

Increasing environmental concerns, the pursuit of lower carbon footprints, and the tightening emission standards in the automotive industry have significantly enhanced

interest in lightweight metals. This trend, combined with the growing emphasis on sustainable manufacturing and cost-effective production, has led to a notable rise in the use of lightweight materials and related research activities. In this context, aluminum alloy casting materials have attracted substantial attention in both academic and industrial fields due to their high strength-to-weight ratio, ease of machinability, and recyclability. This growing interest constitutes one of the primary motivations of the present study.

Aluminum alloy cast components used in the automotive industry are often safety-critical elements. The failure of such parts, particularly in applications such as wheels, can pose serious safety risks. Today, these components—especially in fatigue testing—are typically analyzed using numerical simulations based on the finite element method (FEM), which are subsequently validated through experimental testing. However, CAD-based numerical models generally fail to account for thermal effects that occur during the casting process and the resulting residual stresses within the material. This limitation can lead to discrepancies between numerical predictions and experimental results. More importantly, structural lightweighting and design modifications carried out without considering tensile residual stresses within the material may cause components to reach their fatigue limits earlier than expected. This study aims to address these risks during both the manufacturing and design stages, providing insights and recommendations to enhance product safety.

This research emphasizes that the effects of residual stresses are often overlooked in current industrial practices and thoroughly examines the potential risks associated with this oversight. The study focuses on the analytical and experimental investigation of thermally induced residual stresses in aluminum alloy cast parts. By identifying the influence of temperature gradients during casting on residual stress formation, the research proposes preventive measures that can improve manufacturing processes and design approaches. In this regard, the study seeks to contribute valuable insights to both academic literature and industrial applications within the automotive sector.

Guided by these motivations, this dissertation presents a comprehensive investigation into the measurement and analysis of residual stresses in aluminum cast

components. The fundamental objectives and methodology of the research are described in detail in the following section.

1.3 Aims and Objectives

The primary aim of this study is to design and implement a measurement system for evaluating residual stress in aluminum alloy cast components used in the automotive industry.

To achieve this aim, the processes responsible for residual stress formation in these components and the associated risks were first analyzed. In order to assess these risks in a clearer, quantitative, and reliable manner, an experimental measurement setup was developed. Existing residual stress measurement techniques were comprehensively reviewed, and based on this evaluation, a measurement system suitable for aluminum alloy cast components was designed. The reliability of the developed system is intended to be verified through comparison with alternative measurement methods and analytical calculations.

Ultimately, this study aims to establish a practical, repeatable, and validated measurement system for aluminum alloy cast components, providing a reliable basis for residual stress assessment in industrial applications.

1.4 Originality of the Research

This study makes novel contributions in two main areas: the application of heat treatments to aluminum alloy cast components and the design and implementation of a customized measurement system.

The aluminum alloy used in this research is commonly employed in industrial wheel production, where heat treatment is typically not applied. However, in this study, heat treatments were carried out under different conditions, taking advantage of the alloy's high castability, fluidity, and mold-filling capability. The effects of these treatments on residual stress formation were systematically investigated. By applying heat treatments to a material that is generally not subjected to them in wheel applications, this research offers a new perspective not only for wheel components but also for other cast parts.

Regarding the measurement system, an innovative setup was specifically designed and implemented for aluminum alloy cast components, tailored to the material and product characteristics. The system's versatility and its integration into residual stress assessment provide a unique and practical approach, offering valuable insights for both academic researchers and industrial stakeholders.

1.5 Structure of Thesis

This thesis is divided into six sections. The first chapter conveys the overall background of the research, including its motivation, objectives, originality, and structure. The second chapter reviews and summarizes previous studies and the relevant literature on aluminum alloys and residual stress. The third chapter describes the materials used, the measurement methods, and the analytical and experimental setups employed in this study. The fourth chapter presents experimental investigations, focusing on material and casting processes, heat treatment, and residual stress measurements. The fifth chapter discusses and analyzes the results obtained in detail. Finally, the sixth and concluding chapter provides a general discussion, draws conclusions, and offers recommendations for future work (Figure 1.1).



Figure 1.1 Structure of thesis

CHAPTER TWO
PREVIOUS STUDIES

2.1 Historical Background

Aluminum has a relatively short history, having been discovered in the nineteenth century, yet its use has expanded significantly from the time of its discovery through the nineteenth and twentieth centuries to the present day. Its commercial utilization began in the late nineteenth century and continued to grow with the development of advanced aluminum alloys. Particularly due to its high specific strength, excellent thermal conductivity, corrosion resistance, and recyclability, aluminum has found widespread industrial applications throughout the twentieth century and into modern times. Additionally, despite its relatively low production cost, its high scrap value, continuously expanding recycling market, and increasing global demand indicate that aluminum will maintain its importance both today and future (Ashkenazi, 2019).

Aluminum production technologies were established in 1886, when Hall and Héroult independently patented the electrolytic reduction of alumina to produce metallic aluminum. In 1887, the process for obtaining pure alumina from bauxite was significantly improved through the Bayer process, developed by Carl Josef Bayer. Together, the Hall–Héroult and Bayer processes formed the basis of modern commercial aluminum production and remain the core methods used in the industry today (Buffington, 2012).

In addition to traditional manufacturing methods such as casting, forming, forging, rolling, and extrusion, ongoing technological advancements have led to the development of advanced manufacturing technologies, including powder metallurgy and additive manufacturing methods.

The industrial use of aluminum initially developed in the aviation sector and subsequently expanded into the automotive industry as improvements in production technologies reduced manufacturing costs. In 1903, Wilbur and Orville Wright (the Wright Brothers) utilized a lightweight and robust engine containing aluminum components—an uncommon material selection at the beginning of the twentieth century—for their innovative aircraft (Williams & Starke, 2003).

This early adoption and subsequent advancement of aluminum in the aviation industry eventually transferred to the automotive sector as aluminum production technologies became more extensive and manufacturing costs decreased. One of the most important metrics for evaluating the condition of the national economy and predicting trade expansion is the automotive industry.

In the global economy, the automotive industry brings in over USD 2.5 trillion annually. About 5% of the overall value generated by the automobile industry comes from the aluminum sector (Vaz et al., 2017). According to the sectoral research "Future of Aluminium in the Transportation Sector: An Industry Analysis with Forecasts to 2027" released by Al Circle in 2023, both the worldwide aluminum consumption values for the transportation sector in 2022 and the predicted values for 2027 were presented. According to the survey, the amount of aluminum used in passenger cars is expected to increase from 16,588,000 tons in 2022 to 19,948,000 tons by 2027. For the years 2022–2027, this amounts to a Compound Annual Growth Rate (CAGR) of 3.8%. This growth rate is consistent with wider market predictions when compared to general trends in aluminum demand (Al Circle, 2023).

One of the most significant milestones in the historical development of aluminum was the introduction and widespread use of aluminum alloys. The ability to tailor castability, forgeability, microstructural characteristics, and mechanical properties through different alloying compositions accelerated the industrial advancement of aluminum. Among the most widely used alloying elements are silicon, magnesium, copper, manganese, tin, and zinc, each contributing certain characteristics that increase the material's application across various engineering fields.

The historical development of aluminum alloys can be related back to the early nineteenth century, when the concept of isolating the aluminum element was presented by Sir Humphry Davy. However, the first concrete achievement was realized two decades later, in 1827, when Friedrich Wöhler successfully isolated aluminum through his experimental studies (Mazzolani, 2004).

In 1921, the first commercial Al–Si–Mg (S51) alloys were introduced, followed by the development of the heat-treatable, medium-strength, and corrosion-resistant

commercial alloy 61S (later designated as 6061) in 1935. Owing to its excellent corrosion resistance, 6061 aluminum alloy found widespread application in the railway and marine industries. The use of 61S/6061 alloys has continued to expand over the decades, and they remain widely utilized today in various engineering applications. This alloy is commonly employed in automotive and truck wheels, rods, bars, tubing, and automotive drive shafts (Sanders, 2001).

In 1921, Archer and Jeffries developed Alloy No. 195, a castable and heat-treatable composition that marked a significant advancement in aluminum casting technology. Early applications of this alloy were mostly in architectural components and building facades. By the early 1920s, aluminum cast pistons and aviation engine blocks had also begun to develop. Aluminum casting alloys began to be used more widely in home appliances in 1928, such as food processing equipment, vacuum cleaner housing, and washing machine parts. A major development in casting alloys occurred with the introduction of the A356 alloy. Lemon and Hunsicker improved castability and mechanical performance by reducing the iron content to minimize the formation of insoluble intermetallic compounds. This refinement produced a cleaner microstructure with enhanced ductility and corrosion resistance, thereby expanding the commercial applicability of aluminum casting alloys. Today, as in the past, die casting, permanent mold casting, and sand casting remain the predominant processes for manufacturing structural components, with engines, transmissions, and cast wheels representing a substantial portion of total casting production (Sanders, 2001).

After the Second World War, aluminum and aluminum alloys found extensive and successful applications in the transportation sector, including the railway industry (various specialized wagons), the automotive industry (car and truck bodies), and the marine sector (civil and military vessels, motorboats, and sailing boats). In parallel with these developments, aluminum alloys also began to be used in civil engineering structures (Mazzolani, 2004). From a cultural perspective, aluminum during this period came to symbolize modernity, and its widespread use —ranging from architectural structures to simple household items— was widely noted (Ashkenazi, 2019).

In the early 1950s, the first prefabricated building systems utilizing aluminum alloys began to appear across Europe. However, the limited standardization and the lack of comprehensive specifications during that period hindered the effective use and further development of aluminum alloy structural applications. To overcome these limitations, the ECCS Aluminium Structures Committee launched its first initiative in 1971, aiming to establish design approaches for aluminum alloy structures comparable to the well-established standards, specifications, and safety principles already in place for steel construction (Mazzolani, 2004). These research efforts resulted in 1978 with the publication of the European Recommendations for Aluminium Alloy Structures under the leadership of Prof. Mazzolani of Italy, representing the ECCS Aluminium Structures Committee. This work aimed to position aluminum alloy structures as supporting systems alongside steel structures. Subsequently, in 1992, G. Valtinat from Germany published the European Recommendations for Fatigue Design of Aluminium Alloy Structures (ECCS, 2015). Following the release of the initial European recommendations for aluminum alloy structures, individual European countries began issuing or updating their own national material standards throughout the 1980s. Examples include the British (BS), Italian (UNI), Swedish (SVR), French (DTU), German (DIN), and Austrian (ON) specifications, all of which were progressively developed and revised to accommodate aluminum alloy applications (Mazzolani, 2004).

The Aluminum Association's numerical alloy classification system was first established in 1954 and was subsequently adopted as the American National Standard in 1957. On 15 December 1970, the recommendation was officially adopted by the "International Signatories of the Declaration of Accord" (The Aluminum Association, 2009). The Aluminum Association classifies aluminum alloys according to two principal production methods: wrought aluminum alloys, and cast aluminum alloys, which are produced through casting processes.

The Aluminum Association classifies wrought aluminum alloys using a four-digit numerical system. The 1xxx series represents commercially pure aluminum, containing between 98.9% and 99.99% Al by weight, it is frequently referred to as the pure aluminum group as a result. Owing to their excellent corrosion resistance and

high electrical and thermal conductivity, these alloys are widely used in the chemical and electrical industries. The 2xxx series consists of aluminum–copper alloys and is typically available in profiles, plates, and pipes. Although commonly used as fasteners in the aerospace industry, these alloys require protection in aggressive corrosive environments. The 3xxx series comprises aluminum–manganese alloys, which exhibit superior mechanical properties compared to the 1xxx series but have limited heat-treatability. Their corrosion resistance makes them suitable for applications such as roofing panels. The 4xxx series includes aluminum–silicon alloys, which share similar characteristics with the 3xxx series and are primarily employed as welding wires. The 5xxx series contains aluminum–magnesium alloys. Despite being non-heat-treatable, these alloys provide superior mechanical properties compared to the previous series and are extensively used in marine applications due to their high corrosion resistance. The 6xxx series consists of aluminum–magnesium–silicon alloys, which are heat-treatable. In these alloys, yield strengths may reach up to 250 MPa, with elongations up to approximately 12%. They are generally produced in extruded form. The 7xxx series comprises aluminum–zinc alloys, which are also heat-treatable and available as extruded or rolled products. Through secondary alloying additions (Mg and/or Mg–Cu), these alloys can achieve a wide range of mechanical properties. Finally, the 8xxx series consists of aluminum–iron–silicon alloys, which are commonly used in packaging applications but have also found use in the construction sector due to their fabrication advantages (Ashkenazi, 2019), (Mazzolani, 2004).

Cast aluminum alloys began to be standardized using a three-digit coding system around the 1950s, following an approach similar to that used for wrought aluminum alloys. At that time, several prefix letters were employed to identify material types, yet the rules governing alloy designation were limited and not fully consistent. The system currently in use was adopted around the 1980s and was structured to define alloy series based on their chemical composition as well as to provide information regarding the form in which the alloy was produced (e.g., ingot). For instance, an alloy previously designated as A356 was reclassified as A356.0. More substantial changes occurred for alloys that had originally been placed in incorrect series. For example, an alloy once identified as 108 was reclassified as 208.0, and alloy 43 was redesignated as 443.0. All

alloys can be systematically tabulated, including their corresponding ASTM and SAE specifications (Kaufman, 2000).

The prefix letters placed before the three-digit designation indicate certain variations within cast aluminum alloys, while maintaining overall consistency in the classification system. For example, the previously mentioned alloy A356.0 is a controlled variant of alloy 356.0; the prefix “A” signifies that tighter limits are applied on iron and other impurity levels. Quantitatively, both alloys are widely used; however, alloy 356.0 permits higher impurity contents—for instance, up to 0.6% Fe—which is known to adversely affect ductility and toughness in cast components. In contrast, alloy A356.0 restricts iron and other impurities to lower values (e.g., a maximum of 0.2% Fe), resulting in castings with enhanced ductility and toughness (Kaufman, 2000).

The currently accepted three-digit system is further extended with a decimal designation. For example, the suffix “.0” identifies the cast alloy, while “.1” and “.2” indicate the composition of the ingot (Davis, 2001). Similarly, the ingots of a given alloy may be designated as A356.1 or A356.2, reflecting stricter compositional control during the ingot stage (Kaufman, 2000).

When defining series, cast aluminum alloys were organized into groups in a manner similar to the classification system originally developed for wrought aluminum alloys.

The 1xx.x series represents essentially pure, non-heat-treatable compositions and is commonly used in rotor manufacturing. The 2xx.x series consists of aluminum–copper alloys. The 3xx.x series is primarily alloyed with silicon and may also include elements such as magnesium and/or copper. Alloys in the 3xx.x series account for approximately 90% of total casting production (Davis, 2001). The 4xx.x series is silicon-alloyed, while the 5xx.x series is alloyed with magnesium. The 6xx.x series is generally not used, whereas the 7xx.x series is alloyed with zinc and may include additional elements such as copper and magnesium, similar to the 3xx.x series. The 8xx.x series is tin-alloyed. Finally, the 9xx.x series includes alloys with various other elements. Among these series, the 2xx.x, 3xx.x, and 7xx.x alloys are heat-treatable (Davis, 2001).

Aluminum–silicon (Al–Si) alloys have found wide application, particularly in the automotive and aerospace industries, due to their excellent castability, high mechanical properties, weldability, high thermal conductivity, and superior corrosion resistance. Aluminum–silicon–magnesium (Al–Si–Mg) alloys, obtained by the addition of magnesium, are strengthened by the formation of Mg_2Si precipitates. This type of alloy is also utilized in advanced manufacturing techniques, such as additive manufacturing, in the form of AlSi10Mg alloys containing 0.4–0.6 wt.% Mg (Kempen et al., 2012).

The literature first used the term "residual stress" in 1841. Neumann was the first to provide quantitative references to residual stresses, and since then, a lot of research has been done on the subject (Macherauch, 1987).

Following the conceptual definition, the first measurements of residual stresses were carried out in the 1930s (Alzyod & Ficzere, 2022). During the 1950s, residual stress measurement techniques were further developed and explored from multiple perspectives. Over the past few decades, these techniques have been continuously refined to improve the accuracy of residual stress prediction and calculation, with the goal of achieving values that closely approximate actual stresses (Al-Olabi, 1994).

The evolving measurement techniques can initially be classified into three categories: destructive, semi-destructive, and non-destructive methods. Based on the specific techniques involved, destructive experimental methods include hole-drilling, ring-core, deep hole drilling, contour, layer removal (or curvature), and sectioning techniques. Non-destructive experimental methods encompass X-ray diffraction (XRD), ultrasonic, neutron diffraction, and magnetic techniques. Analytical approaches involve the measurement or estimation of residual stresses through analytical calculations and finite element models.

Among destructive measurement techniques, the hole-drilling method is the most commonly used due to its simplicity and rapid application. The German scientists Mathar originally suggested this successful technique in 1934. The technique is based on placing a strain gauge at the point of interest on the workpiece surface and drilling a hole at the measurement location to assess the residual stress. The American Society

for Testing and Materials (ASTM) introduced the test method in 1981 and published it as ASTM E837-1981 (Guo et al., 2021). Following several revisions in 2008, the standard was updated to ASTM E837-08 and subsequently published in 2015 as a standard test procedure by ASTM (X. Li et al., 2024).

In 1950, significant improvements were made to the accuracy and reliability of strain measurements in the hole-drilling method. Around the same period, in 1951, Milbradt introduced the ring-core method, marking further development in destructive measurement techniques (Guo et al., 2021). In 1971, Finnie proposed the slitting method, which was later refined by Cheng. The contour method was introduced in 2000 and subsequently published in 2001 (X. Li et al., 2024).

Regarding non-destructive measurement methods, diffraction techniques have become widely recognized for residual stress assessment without damaging the specimen. The use of X-ray diffraction (XRD) for stress determination in crystals began during the 20th century (X. Li et al., 2024). However, the application of XRD specifically for residual stress measurements commenced in 1959. The advantages of X-ray techniques include the ability to achieve measurements at varying depths, enhancing their applicability (Guo et al., 2021).

In 1953, Hughes and Kelly formulated the theory of acoustoelasticity, and in 1959, Benson and Realson introduced a method using polarized ultrasonic waves to determine uniaxial stresses in isotropic materials, laying the foundation for ultrasonic residual stress measurement techniques (X. Li et al., 2024). During the 1960s, advancements in laser technologies and nanotechnology further enhanced these methods. A relatively recent approach, the magnetic method, was developed in 1994 by Doubov (Guo et al., 2021).

More recently, numerical techniques have been used to measure residual stress. While destructive and non-destructive experimental techniques were initially the primary approaches for residual stress analysis, the increasing costs associated with measurement instruments, setup, and time in industrial applications have driven the development and adoption of analytical and finite element models. The main advantage of numerical methods lies in their relatively short processing times and the

absence of costs for measuring equipment and setup. However, a key limitation is that they cannot fully replicate all real-world conditions.

In 1976, internal stresses were calculated using numerical methods through the Finite Element Method (FEM) (Rigdahl, 2006). The development of numerical modeling techniques has led to an increase in the use of numerical methods in recent research, both for preliminary evaluations before physical measurements and for comparison with experimental data. In addition to providing pre-evaluation capabilities prior to carrying out experimental measurements, these investigations aim to evaluate the correctness of calculated values against experimental data, thereby enhancing the dependability of numerical forecasts (Menne et al., 2007), (Johnson et al., 2012), (P. Li et al., 2007b).

The use of aluminum alloys in the automotive industry has expanded not only due to reduced costs associated with the widespread adoption of manufacturing technologies, but also in parallel with the historical demands of the automotive sector.

The energy and oil crisis that began in 1973 positively shifted the demand for lightweight components in the automotive industry. This demand has increased up to this point because of the ongoing increase in fuel and energy prices. Today, the automotive industry's ongoing requirements for fuel efficiency and eco-friendly manufacturing indicate that the use of aluminum alloys will continue to grow from past to future.

The term "fuel efficiency" refers to weight reduction strategies aimed at decreasing fuel consumption and enhancing overall operational efficiency. Consequently, the use of lightweight materials with high strength-to-weight ratios becomes essential. The term "eco-friendly", on the other hand, denotes the requirement to reduce emissions from both vehicles and their manufacturing processes. Hence, non-toxic materials and low-emission production methods are preferred (Gupta & Singhal, 2022).

Considering all these requirements, aluminum casting alloys—being lightweight, possessing high strength-to-weight ratios, and offering high recyclability—are well suited to meet the evolving demands of the automotive industry.

By the 1980s, Al–Si casting alloys had become standard materials for engine components. In the specific case of aluminum alloy wheels, Al–Si–Mg alloys are preferred due to the small additions of magnesium, which promote age hardening. Their ability to undergo heat treatment, particularly the T6 temper, provides significant increases in yield strength and excellent corrosion resistance, further reinforcing their suitability. Although their early development was based on sand casting, permanent mold casting techniques are predominantly used today (Polmear, 2006).

Aluminum alloy wheels are unique now due to features like lightweight design and recyclability, but their original use in automotive applications was mainly motivated by the need to give cars a unique and luxurious look. At first, high-end car models were the ones with aluminum alloy wheels (European Aluminium Association, 2011).

The production history of aluminum alloy wheels began in 1948 with forged aluminum wheels manufactured by ALCOA. When Otto Fuchs' forged aluminum alloy wheel was used in the construction of the Porsche 911 in 1962, it was an especially significant advance in Europe. This use is regarded as an important turning point in the evolution of aluminum alloy wheels (European Aluminium Association, 2011).

Cast aluminum alloy wheels started to be available as factory-installed parts on mass-produced cars in the 1970s. A significant development in manufacturing methods was reached in 1979 when Toyota Motor Company in Japan began producing automobile wheels using the squeeze casting process (Polmear, 2006). Low-pressure die casting (LPDC) is currently the most common manufacturing method. It is supplemented to less extent by gravity permanent mold casting and to a much smaller amount by squeeze casting, counter-pressure die casting, casting–forging hybrid processes, and thixocasting. Applying flow-forming to the rim section following low-pressure die casting is another more modern method. One-piece cast and forged aluminum alloy wheels, multi-piece wheel designs, and magnesium alloy wheels are a few examples of how manufacturing technologies are expected to keep developing in the future (European Aluminium Association, 2011).

In the early 2000s, the market share of aluminum alloy wheels in Europe was approximately 30–35%. According to a report published in 2011, this share had increased to 50% (European Aluminium Association, 2011). According to a research published in November 2025, the market share reached in 2024 at 81.6%. According to the same analysis, the global wheel market is projected to increase from its 2024 valuation of 3.17 billion USD to 4.58 billion USD by 2033. This corresponds to an expected 4.2% compound annual growth rate (CAGR) during that time (Grand Review Research, n.d.).

2.2 State of the Art and Literature Review

The literature review presented in this chapter is structured under two main sub-headings that are directly related to the scope of this study: “Aluminum Alloys and Heat Treatment” and “Residual Stress and Measurement Methods.”

In the first subsection, titled “Aluminum Alloys and Heat Treatment,” the classification of cast aluminum alloys is presented, with particular emphasis on the 3xx.x series, which accounts for approximately 90% of all shaped castings produced from castable aluminum alloys (Davis, 2001). Additionally, typical industrial cast parts made from this alloy series are presented. Within the scope of this study, the alloys historically and currently used in the production of aluminum wheels are reviewed in terms of their properties, heat-treatability, and commonly applied heat-treatment procedures. The advantages and limitations of the AlSi11Mg casting alloy employed in this work are outlined, and the heat-treatment practices reported in the literature for both primary and secondary alloys—including soft annealing and T6 heat treatment—are summarized together with their effects on mechanical properties. This comprehensive overview provides the basis for establishing the experimental framework of the present study by revealing the range of possible heat-treatment strategies and their anticipated influences, thereby guiding the selection of the approach adopted in the experimental design.

In the second subsection, titled “Residual Stress and Measurement Methods,” the concept of residual stress is first defined, followed by a structured review of destructive, semi-destructive, and non-destructive measurement techniques as

presented in the literature. Within this framework, commonly used destructive experimental methods—such as the hole-drilling method, ring-core method, deep-hole drilling method, contour method, and sectioning method—are discussed. Likewise, non-destructive experimental techniques including X-ray diffraction (XRD), ultrasonic methods, neutron diffraction, and magnetic methods, along with analytical approaches involving analytical formulations and finite element–based residual stress evaluation, are examined with respect to their application domains. The subsection reviews studies that focus on residual stress measurements in aluminum cast components, paying particular attention to the impact of geometric complexity, heat-treatment parameters, and casting conditions on the measured residual stress distributions.

2.2.1 Aluminum Alloys and Heat Treatment

According to the classification of castable aluminum alloys, 3xx.x alloys containing Al-Si-Mg are widely preferred in automotive applications due to their excellent castability, high mechanical strength, high thermal conductivity, outstanding corrosion resistance, and favorable wear resistance.

Davis reported that 3xx.x alloys are preferred for automotive components such as engine blocks and wheels because their mechanical properties can be enhanced by alloying not only with silicon but also with elements such as magnesium and/or copper (Davis, 2001).

High silicon content alloys in the 3xx.x series have several advantages when it comes to castability; high silicon content is associated with beneficial properties like outstanding fluidity and mold-filling ability. He emphasized that for large and geometrically complicated castings, the 3xx.x series is frequently chosen (Kaufman, 2000).

For aluminum alloy wheel applications, excellent mold-filling capacity, resistance to die adhesion, low susceptibility to hot tearing and shrinkage defects, high impact strength, ductility, excellent corrosion resistance, and high fatigue performance are just a few of the crucial parameters that the chosen alloy must fulfill. Hypoeutectic Al–Si

casting alloys (Si concentration < 12.6 wt%) are preferred as wheel materials when they meet these parameters (European Aluminium Association, 2011).

According to the European Aluminium Association, AlSi11Mg alloys with 11–12% Si were widely used in Germany and Italy up until the 1980s. They noted that although this alloy had considerable benefits in terms of mold filling and shrinkage behavior, it had limitations in terms of strength and fatigue limits (European Aluminium Association, 2011).

Today, Sr-modified AlSi7Mg0.3 (A356) and AlSi11Mg alloys constitute the standard aluminum casting alloys used for wheel manufacturing (European Aluminium Association, 2011). In recent years, driven particularly by the need to improve fuel efficiency, there has been a continuous increase in demand for lighter yet mechanically stronger components. To meet these requirements, the application of additional processes to aluminum cast components has become essential. For aluminum alloy wheels in particular, heat-treatment processes are employed to achieve the required levels of mechanical strength and toughness. For example, the T6 heat-treatment process significantly increases tensile and yield strengths, thereby improving mechanical performance and toughness; this results in superior outcomes under fatigue and impact testing conditions. Considering these two alloys, which have become standardized in industrial applications, AlSi7Mg0.3 alloys offer advantages in terms of heat-treatability.

Tarkun explained that due to the two alloys' magnesium contents differ, AlSi11Mg alloys are not heat treated during the manufacturing of industrial wheels. Tarkun reported that, in industrial practice, the Mg content of AlSi11Mg alloys is approximately 0.1% lower than that of AlSi7Mg alloys, and that the higher Mg level in AlSi7Mg alloys leads to the formation of a greater amount of Mg_2Si precipitates during heat treatment. These precipitates contribute significantly to strength enhancement, thereby making AlSi7Mg alloys more responsive to heat-treatment-based strengthening (Tarkun, 2015).

Campbell noted that main engineering casting alloys used in industry are based on Al–Si alloys, and the addition of Mg encourages the precipitation of the Mg_2Si phase during precipitation-hardening heat treatments (Campbell, 2011).

Pedersen and Arnberg noted that a high eutectic fraction and thus a larger quantity of silicon crystals capable of diffusing excess silicon are produced by the significant amount of Si contained in the aluminum matrix of Al-11Si-Mg alloys. According to their findings, silicon that is more than what is needed to generate Mg2Si precipitates can remain in solid solution, increasing the deviation from equilibrium (Pedersen & Arnberg, 2001).

Similarly, in AlSi11Mg alloys, the high silicon content diminishes the effectiveness of magnesium and silicon (Mg_2Si) required for precipitation hardening. The excessive silicon within the microstructure contributes to the formation of a hard and brittle matrix. Such brittleness restricts the improvement of toughness and ductility after heat treatment, preventing these properties from reaching the desired levels.

Based on these findings in the literature, it can be inferred that the high silicon content in AlSi11Mg alloys necessitates the addition of magnesium to enable the formation of Mg_2Si precipitates and to achieve effective precipitation hardening. Accordingly, while the Mg content in AlSi7Mg0.3 alloys is typically around 0.3 wt.%, For AlSi11Mg alloys to have equivalent hardening potential, the magnesium level needs to be raised.

Despite the limitations of AlSi11Mg alloys in terms of heat-treatability, their excellent castability has led to growing industrial interest in heat-treated AlSi11Mg alloys in recent years. Owing to their superior fluidity and mold-filling capability, these alloys have increasing potential not only in aluminum wheel production but also in various other automotive cast applications, particularly for components featuring complex and complex geometries.

Dahle et al. investigated the influence of grain refiner additions (AlTi5B1 master alloy) on the fluidity of AlSi7Mg and AlSi11Mg casting alloys, which are widely used in automotive wheel production. The AlSi11Mg alloy demonstrated a longer spiral fill length than the AlSi7Mg alloy in fluidity testing using the Archimedean spiral mold

method, showing improved fluidity. The increased silicon concentration of the AlSi11Mg alloy, which increases the heat released during solidification and allows simpler dendritic structure dispersion, was the reason given by the researchers for this behavior. The study highlighted that AlSi11Mg has a greater capacity to fill mold during casting and concluded that fluidity is controlled by a variety of factors (Dahle et al., 1996).

Both T5 and T6 heat treatments are used to AlSi11Mg alloys, according to the "Primary Aluminum Casting Alloys" study from Rheinfelden Alloys, a well-known company in the sector. The T6 heat treatment process consists of solution treatment (520–535 °C for 6–10 hours), quenching (at 20 °C), and artificial aging (130–170 °C for 6–8 hours). The report also provides mechanical properties obtained for permanent mold cast components in both as-cast and T6 conditions. For castings with wall thicknesses up to 20 mm, the T6 heat treatment results in increases of 50% in yield strength (YS), 17% in tensile strength (UTS), 27% in hardness, and 15% in fatigue strength compared to the as-cast condition (Rheinfelden Alloys, 2016).

In industrial applications, AlSi11Mg alloys, as aluminum–silicon alloys close to the eutectic composition (12.6 wt.% Si), are preferred due to their high castability and low tendency to crack. However, the irregular and sharp-edged eutectic silicon precipitates present in these alloys reduce impact strength (Elmahti et al., 2023) (Özaydın, Armakan, et al., 2019). According to the literature, soft annealing can refine and round these precipitates, thereby enhancing the ductility of the material (Özaydın & Kaya, 2019).

Jarco investigated the effects of soft annealing on the mechanical properties of the EN AC-AlSi11 alloy. The annealing process was carried out within a temperature range of 280–370 °C and for durations of 2–8 hours. The obtained results indicated that the best performance was achieved with annealing at 370 °C for 8 hours. The annealing process significantly increased the impact strength while decreasing the Brinell hardness (HB). Under ideal conditions (370 °C, 8 hours), the impact strength increased by 71%, whereas the Brinell hardness decreased by 20%. These findings demonstrate that the annealing process is an effective method to achieve a balance between ductility and hardness (Jarco, 2017).

In another study conducted by Jarco and Pezda, a typical T6 heat treatment was applied instead of soft annealing to the same EN AC-AlSi11 alloy. The effects of the T6 heat treatment and its optimization on the mechanical characteristics and microstructure of the Fe-containing AlSi11 alloy were examined in this work, with a focus on industrial applications. The results of the experimental studies, which were conducted with various combinations of temperature and time, showed that the most effective ranges were 165–200 °C for aging and 510–545 °C for solution treatment. These results demonstrate how crucial it is to optimize the T6 heat treatment in order to improve microstructural properties and mechanical performance (Jarco & Pezda, 2021).

Vuksanović et al. examined how the T6 heat treatment affected the mechanical characteristics of the AlSi11 alloy. The applied heat treatment consisted of solution treatment at 520 °C for 6 hours, followed by water quenching at 70 °C, and finally artificial aging at 205 °C for 7 hours. Ultimate tensile strength (UTS) and elongation (%) only slightly increased following the treatment, but hardness significantly decreased. According to the researchers, the low magnesium content, the shape of the eutectic silicon, and the existence of harmful intermetallic phases were the main causes of this limited improvement and the decrease in hardness (Vuksanović et al., 2021).

Pedersen and Arnberg investigated the effects of T6 heat treatment on four different compositions of Al-Si-Mg casting alloys, including Al-11Si-0.2Mg and Al-11Si-0.6Mg. The T6 heat treatment consisted of solution treatment at 540 °C for 1, 4, and 24 hours, followed by quenching in water, air, or oil at room temperature, and finally artificial aging at 150 °C for 4 hours. According to the results, the alloy with the highest ultimate tensile strength (UTS) had a magnesium concentration of 0.6%. Nevertheless, the maximal strength was reached after 60 minutes, and longer solution treatment times (240–1440 minutes) did not result in further improvement. Because of the high silicon concentration, the AlSi11Mg alloys' ductility remained restricted, and their elongation (%) was much lower than that of the AlSi7Mg alloys. While slower cooling (air 1.8 K/s, oil 12 K/s) resulted in a loss in strength because of the reduction of Mg_2Si precipitates, quick cooling (water, average 97 K/s) produced increased strength during

quenching. Slower quenching may improve ductility, however in high-silicon alloys, this impact was still restricted (Pedersen & Arnberg, 2001).

Abdelaziz et al. investigated how heat treatment and various alloying elements affected the mechanical characteristics of AlSi11-based alloys. The alloy with 0.4% Mg showed tensile strength (UTS) performance similar to that attained with about 3% Cu addition, according to the study's comparison of Mg and Cu additions. The T6 heat treatment applied in the study consisted of solution treatment at 510 °C for 8 hours, followed by quenching at 60 °C, and finally artificial aging at 155, 180, 200, 220, and 240 °C for 5 hours. The highest tensile strength was obtained after artificial aging at 180 °C. Examining the impacts of alloying elements, it was found that Sr enhanced ductility through modifying the silicon particles, whereas Mg and Cu increased strength by precipitation hardening. However, the combined use of Sr and Mg was reported to reduce modification efficiency, and the resulting intermetallic phases could act as potential crack initiation sites (Abdelaziz et al., 2019).

Altınel utilized Sr-modified AlSi11Mg alloy as an automotive wheel material and investigated its mechanical behavior under various testing conditions. The mechanical properties of the specimens were evaluated in this investigation after they were aged at eight different temperatures, ranging from −50°C to 200°C. The specimens were next aged for doubled time as long at 150°C and 0°C in accordance with the earlier experimental settings, and the outcomes were examined. According to the results, tensile strength did not significantly alter at room temperature, but it did decrease as the temperature increased. Yield strength reached its maximum value at room temperature. Additionally, elongation increased rapidly above 150 °C, while a slight decrease was observed below 0 °C. These results demonstrate the critical influence of temperature and aging duration on the mechanical performance of Sr-modified AlSi11Mg alloy (Altınel, 1999).

There are few sources of information about T6 heat treatment's industrial uses in the literature because of its limited impact on AlSi11Mg alloy. While this highlights the significance of the present study in terms of addressing a research gap and providing originality, it also complicates direct comparisons with similar industrial studies. Therefore, AlSi10Mg casting alloys, which are widely used in the automotive

industry and exhibit chemical compositions similar to AlSi11Mg, have also been investigated.

Neuser et al. investigated the effects of solidification rates on the microstructure and mechanical properties of AlSi10Mg casting alloy, which is widely used in the automotive industry, under different thicknesses and heat treatment conditions to enhance its mechanical performance. In this study, mechanical properties, specifically tensile strength and Brinell hardness, were evaluated in AlSi10Mg plates with thicknesses of 2-4 mm under both as-cast and T6 heat-treated conditions. The findings showed that improving the microstructure through higher solidification rates or the application of modification components was required for thicknesses of 3 mm and higher. These results show that the mechanical performance of Al-Si-Mg alloys is significantly influenced by thickness and solidification rate parameters (Neuser et al., 2022).

Menteşe et al. conducted a study on the optimization of the T6 heat treatment for AlSi10Mg cast components used in industrial applications, particularly for engine brackets. The study considered variations in part dimensions and thickness. The implementation led to a 28% increase in overall production capacity and a 24% improvement in energy efficiency by identifying and implementing the ideal processing parameters. These findings demonstrate that optimizing T6 heat treatment parameters is crucial both for enhancing mechanical performance and for improving efficiency in industrial production (Menteşe et al., 2019).

Beder et al. applied a T6 heat treatment to AlSi10Mg cast alloy, which included air cooling, quenching, and aging stages. Yield strength (YS) increased by 70%, ultimate tensile strength (UTS) increased by 115%, and wear resistance improved after the T6 treatment. These results demonstrate that T6 heat treatment significantly enhances both the mechanical and tribological performance of AlSi10Mg cast alloys (Beder et al., 2024).

Although numerous heat treatment applications have been reported for AlSi7Mg0.3 (A356) alloy wheels (Özaydın, 2019), (Özaydın, 2022), (Kaya, 2024), (Kutsal et al., 2024), (Pezda, 2022), applications for heat treatment of AlSi11Mg alloy wheels are

almost absent. This highlights a clear gap in the literature, which the present study aims to address by investigating the heat treatment of AlSi11Mg alloy wheels.

The significant temperature gradients that form during the T6 process might lead to crack formation in crucial areas of the component, despite all the benefits of heat treatment. These cracks could compromise the product's structural integrity, especially if they appear as micro or macro defects. Microcracks present a greater risk to product reliability because they can spread during service and result in delayed failures, whereas macrocracks are typically identifiable using traditional inspection and testing techniques. Therefore, it is crucial to investigate the reasons why temperature gradients during the heat treatment process generate cracks. It should be mentioned that residual stresses in the material may be the cause of cracks that develop following heat treatment procedures with high temperature gradients.

2.2.2 Residual Stress and Measurement Methods

Residual stresses, also referred to in literature as trapped or locked stresses, can be defined as non-uniform elastic stresses that develop within a material because of various manufacturing processes or heat treatment applications. Their formation is influenced by both mechanical and thermal effects. Production processes like machining, plastic forming, additive manufacturing, and welding can result in mechanically generated residual stress. Thermally induced residual stresses, on the other hand, originate from diverse heat treatment processes, rapid cooling conditions, and multiple thermal cycles. The ability of residual stresses remains within the material even in the absence of any external mechanical or thermal load that distinguishes them apart from other types of stress. For this reason, residual stresses are considered a critical material parameter that significantly affects service performance as well as key properties such as fatigue behavior, dimensional stability, and crack formation (Tabatabaeian et al., 2022) (Hibbeler, 2014).

In industrial applications of aluminum cast engine blocks, residual stresses within the material, arising under tensile or compressive loads during service, can compromise structural integrity by initiating microcracks or promoting the propagation of existing cracks. This phenomenon may adversely affect the

component's overall reliability by significantly decreasing its fatigue life, especially under high cycle loading conditions (Alipooramirabad et al., 2024; Carrera et al., 2007).

Depending on the service conditions to which a cast component is subjected, tensile or compressive residual stresses can cause the actual stress state within the material to deviate from the predicted values under nominal loading conditions. Tensile residual stresses can accelerate crack initiation and propagation in components subjected to fatigue loading, significantly reducing the service life of the part. In contrast, compressive residual stresses can suppress crack propagation under the same loading conditions, thereby enhancing fatigue performance. The distribution of residual stresses within a component can vary significantly depending on both the geometric characteristics of the design and the applied manufacturing and heat treatment processes; indeed, it is possible for some regions of a single part to experience tensile residual stresses while other regions exhibit compressive residual stresses. Therefore, accurate, reliability, and high-precision determination of residual stresses is critical for both the optimization of component design and the proper selection of manufacturing and heat treatment parameters. Moreover, the influence of residual stresses on dimensional stability makes these measurements an integral part of industrial production processes. Essentially, residual stresses cannot be measured directly; rather, they are calculated indirectly by measuring the elastic deformations they cause within the material. This approach forms the fundamental basis of the experimental techniques employed in residual stress analysis.

Various methodologies and terminologies are used in the literature to categorize residual stress measuring techniques. Some researchers categorize these methods as "destructive," "semi-destructive," and "non-destructive" measurement techniques (Tabatabaeian et al., 2022), while others consider semi-destructive techniques within the scope of destructive measurement methods (Rossini et al., 2012). In terms of the techniques involved, destructive experimental methods include hole-drilling, ring-core, deep hole drilling, contour, and sectioning techniques. Non-destructive experimental methods encompass X-ray diffraction (XRD), ultrasonic, neutron diffraction, and magnetic techniques. In addition, analytical methods, which aim to

calculate residual stress using analytical approaches and finite element modeling, are considered a significant measurement approach in the literature (Rossini et al., 2012). Despite the differences in classification approaches, analytical measurement methods, which enable the determination of residual stresses using analytical approaches and finite element models, can increasingly be regarded as a component of the "non-destructive" measurement category in both classification schemes, reflecting their growing importance in recent years.

Metallic, ceramic, and composite systems are just a few of the materials utilized in industrial applications that can be measured for residual stress. (Reid & Paskaramoorthy, 2009) (Olson et al., 2022). Among them, metallic materials are the most frequently used for residual stress measurements, followed in frequency by metal matrix composites (MMC), ceramics, and polymers (Kandil et al., 2001). In addition, R&D and academic studies on a sectoral basis show that residual stress measurements find extensive applications in the aerospace, energy and power generation, and automotive industries. Automobile engine pistons, engine cylinder blocks and heads, and suspension parts are a few examples of these industry-specific uses (K. Li et al., 2008).

In a report published by Kandil et al., the frequency of use of the residual stress measurement techniques employed by UK industrial groups was ranked. According to the report, the most widely used method, at 30%, is the hole-drilling technique. This is followed by X-ray diffraction (XRD) at 26%. These two methods stand out as the most often used examples of non-destructive and destructive measurement techniques, respectively. Other approaches include neutron diffraction (19%), layer removal (16%), and magnetic and ultrasonic procedures (9%) (Kandil et al., 2001). These data offer important insights into the preferences for residual stress measuring techniques across several industrial sectors, even though they represent the practices of industrial companies in the United Kingdom.

Various terms are used in literature to refer to the hole-drilling method. Shokrieh and Ghasemi K. define the technique as "central or blind hole drilling" (Shokrieh & Ghasemi K., 2007), whereas Ghasemi et al. classify it as "incremental or deep hole drilling" (Ghasemi et al., 2014).

Because of its ease of use and rapidity, the hole-drilling method is the most popular destructive measurement method. According to Rossini et al., this method is sometimes categorized as a semi-destructive technique in some sources because the holes drilled for measurement are small (about 1.8 mm in diameter and at most 2.0 mm in depth) and easily repairable. The primary advantages of the hole-drilling method include high accuracy, reliability, standardized testing procedures, and practical applicability (Rossini et al., 2012).

Magnier et al. have used this technique for plastic materials, however it is most frequently used for metallic materials in industrial settings (Magnier et al., 2017). Additionally, Wu et al. applied the hole-drilling method to hybrid materials, such as metal–carbon fiber reinforced plastics (Wu et al., 2020).

Flaman pointed out that the observed total stresses might be greatly impacted by possible errors, especially when drilling at a low speed. Consequently, due to its superior performance, the use of a high-speed drill (up to 400000 rpm) is preferred in the hole-drilling method (Flaman, 1982). Scafidi et al. emphasized that eccentricity is one of the major sources of error in the analysis. Errors resulting only from eccentricity can be more than 10% under normal experimental settings. However, the operator's skill is thought to be the most important element influencing measurement accuracy. (Scafidi et al., 2011).

In a standard based on various studies in literature (ASTM E837-20: Standard Test Method for Determining Residual Stresses by the Hole-Drilling Strain-Gage Method), the requirements for the hole-drilling method are defined in a standardized manner. The common hole drilling method uses high-speed air turbine or electric motor-driven carbide drills or end mills that can rotate at rates between 20000 and 400000 rpm, and it works with most materials except the hardest ones (ASTM, 2020).

According to Li et al., recent advancements in measurement technology have provided significant improvements for the hole-drilling technique. However, there are certain limitations associated with strain gauges. These limitations include an extended setup procedure, a limited number of measurement points, and accuracy problems

brought on by slight misalignments in the hole's location within the rosette during the hole-drilling operation (X. Li et al., 2024).

Trebuňa et al. investigated the effects of production processes such as casting, rolling, welding, and stamping—which are known to induce residual stresses affecting fatigue behavior and component safety—using the hole-drilling method. High amounts of residual stress can form in welded areas, according to measurements made in compliance with the ASTM E837 standard. When these stresses are combined with service loads, the structural lifetime may be shortened (Trebuna et al., 2008).

Arabul and Lunt developed and validated a low-cost, fully open-source measurement system for residual stresses, combining the hole-drilling method with digital image correlation (DIC). The device was designed to overcome the disadvantages of traditional strain-gauge rosettes, such as high cost, complex setup, and long preparation times. It integrates hole-drilling with microscopic imaging via a two-axis motion mechanism. This approach provides advantages in production cost and preparation time and was validated against conventional strain-gauge measurements, with the measured stress values matching theoretical predictions within ±30 MPa. The open-source system represents a significant alternative for low-cost, rapid, and reliable residual stress measurements in both academic research and industrial applications (Arabul & Lunt, 2022).

Cione et al. investigated residual stress in aluminum alloy wheels in response to the introduction of residual stress evaluation requirements in product specifications, manufacturing procedures, and quality control processes. Residual stress fields and distributions on the wheel were measured using the hole-drilling method with rosette strain gauges in a commercially available measurement system. The measured values in the regions identified as critical for residual stress closely corresponded to results obtained via finite element analysis (FEA). The average residual stress across the entire wheel was calculated to range between 80 and 145 MPa (Cione et al., 2012).

In another study, Cione et al. measured residual stresses in aluminum alloy wheels using destructive (hole-drilling), non-destructive (X-ray diffraction, XRD), and analytical (finite element analysis, FEA) methods, and compared the results. The

measurements and calculations revealed that the residual stress values on the aluminum wheel were 195.3 MPa, 186.4 MPa, and 175.0 MPa for the hole-drilling, XRD, and FEA methods, respectively (Cione et al., 2016).

A variant of the hole-drilling approach is the ring-core method. While the ring-core approach removes material in the shape of a ring around the strain gauge, the hole-drilling method drills a hole in the middle of the strain gauge. The residual stresses are determined by measuring the resulting deformations. The ability to detect larger deformations, which enables the measurement of higher residual stress levels, is the main advantage of the ring-core approach over the hole-drilling technique. However, compared to the hole-drilling approach, it is less frequently utilized because of the higher harm done to the measured material and the practical challenges of implementation.

Baldi emphasized that the ring-core method's principle-based reusability—the strain gauge rosette can be reinstalled after the core is removed—is a key benefit. Compared to other methods, this property enables the method to measure residual stresses at deeper depths and achieve higher strain measurement accuracy. However, Baldi emphasized that implementing this approach in practice is quite challenging. Specifically, the repetitive installation and wiring of the strain-gauge rosettes presents significant experimental challenges as the measurement depth increases. Baldi therefore suggested using an optical measurement approach to preserve the ring-core method's depth advantage (Baldi, 2016).

Masláková et al. provided a detailed, step-by-step explanation of strain-gauge applications for determining residual stresses using the ring-core method. They pointed out that this technique's greater sensitivity in comparison to the hole-drilling method is one disadvantage. Nonetheless, the ring-core technique has an advantage over hole-drilling in that it is less sensitive to small errors in hole diameter or eccentricity. However, the damage to the specimen is inevitably higher because the ring depth is deeper than in the hole-drilling approach (Masláková et al., 2012).

The deep-hole drilling method can be considered an intermediate form between the hole-drilling and ring-core techniques. This approach involves drilling a hole all the

way through the workpiece and measuring the hole's original diameter. The material surrounding the hole is then removed in an annular shape, much like in the ring-core procedure. The hole diameter is measured once more after the conclusion of the process, and the residual stress is computed using the difference between the original and final diameters.

To create stresses that were either equal to or greater than the yield strength, Hosseinzadeh et al. quenched stainless-steel cylinders and rings with water. Neutron diffraction and two mechanical stress-relieving techniques, incremental center-hole drilling and deep-hole drilling, were used to assess the residual stresses. The measurements showed that, although the trends were like the cooling predictions obtained from finite element analysis, there was only limited agreement in terms of stress magnitudes. Measurements using reconstructed stresses, however, showed stronger connection. It is interesting to note that they also found excellent agreement between measurements of neutron diffraction and deep-hole drilling (Hosseinzadeh et al., 2014).

The contour method was first proposed by Prime in the early 2000s (Prime, 2001) and was applied to evaluate residual stresses in two dimensions.

Hacini et al. highlighted in their study that welded components are subjected to high levels of residual stresses around the welded seams, which could be a potential cause of premature cracking. In their lab, originally stress-free austenitic stainless steel 304L specimens were subjected to compressive residual stresses using a robotic hammering system. The residual stresses were then assessed using the contour method (Hacini et al., 2009).

Brown et al. detected residual stresses in a welded cylinder and contrasted the contour method's findings with neutron diffraction. The results showed that stress levels obtained using the contour method were around 50 MPa higher than those obtained using the neutron diffraction method (D. W. Brown et al., 2011).

Wang et al. proposed a novel method for contour measurement using a 3D scanner to determine section residual stresses in structural components with complex geometries. The axial residual stress distribution in a welded pipe with different

properties was assessed using this method, and the outcomes were validated by comparing them with data from a reference contour measurement machine (CMM). In terms of both observed contours and calculated residual stresses, the comparison showed a strong quantitative agreement between the two approaches. Furthermore, compared to the reference approach, the suggested method reduced the measurement time by around 99% (Wang et al., 2020).

The sectioning technique is a destructive residual stress measurement method based on measuring the deformations that occur as residual stresses are released when a specific mass or volume is removed from the test specimen.

In order to determine the residual stresses generated along the cutting line, Rossini et al. used the sectioning technique, which involves making cuts on a plate whose physical dimensions have already been measured and documented. It was highlighted in the study that the cutting procedure must not cause temperature effects or plastic deformation, as these could change the initial residual stress state at the cut surface and lower measurement accuracy. Strain gauges are used to record the strains released during the cutting process (Rossini et al., 2012).

Ekmekçi, in his study, outlined the sectioning approach as a strategy built on the idea of "cutting a stressed object to release internal stresses." The amount of material removed in each example defines the average deformations that occur, and the magnitude of these deformations directly determines the amount of residual stress that is released (Ekmekçi, 2004).

The analysis of elastic deformations caused within the material is the essential foundation of non-destructive methods. These methods' main benefit is their capacity to evaluate residual stresses without physically harming the specimen. X-ray diffraction (XRD), ultrasonic techniques, neutron diffraction, and magnetic approaches like Barkhausen noise analysis are some of the most used non-destructive residual stress measuring methods in both the literature and industrial applications.

Robinson and Redington measured near-surface residual stresses using the XRD method and correlated these stresses with the strength and hardness properties of heat-treated aluminum alloys. A similar residual stress distribution across the thickness was

seen in all of the aluminum alloys under investigation, with compressive stresses predominating close to the surface and tensile stresses predominating in the inner areas. The measured residual stress magnitudes varied according to the strength of the alloys. Additionally, it was discovered that the residual stresses at the surface showed a linear relationship with the strength and hardness (Vickers) values obtained after quenching (Robinson & Redington, 2015).

Ramana et al. used X-ray diffraction (XRD) to assess residual stress distributions in several metals, including maraging steel and quenched-and-tempered medium-carbon steel alloys (Ramana et al., 2010).

In ultrasonic methods, the velocities of ultrasonic waves, which change in response to the stress condition within the solid material, can be used to measure residual stresses.

Javadi et al. investigated the evaluation of residual stresses along the thickness of welded austenitic stainless-steel plates using finite element analysis and ultrasonic methods. The finite element model's output was first compared to measurements made using the hole-drilling method, and then the model was verified using data collected using the ultrasonic approach (Javadi et al., 2013).

Zhan et al. conducted experimental and numerical simulation studies on the measurement of residual stresses using the laser ultrasonic method. The ABAQUS software's function module was used to model welding-induced residual stresses in the specimen using a predetermined stress field in the numerical simulation. There was a good degree of agreement between the experimental data and the finite element analysis results (Zhan et al., 2017).

A review of the literature indicates that the ultrasonic method is particularly widely used for measuring residual stresses in welded components and those induced by the welding process.

Like the X-ray diffraction approach, the neutron diffraction method changes in the distance between atomic planes inside the crystal structure of the material to estimate residual stresses.

As mentioned earlier, Brown et al. used the contour approach and the neutron diffraction methodology to compare residual stresses in a welded component. According to the findings, stress levels from the neutron diffraction approach were about 50 MPa lower than those from the contour method (D. W. Brown et al., 2011). The main cause of this difference is the methodological approach: the neutron diffraction method uses volumetric averaging of the findings, whereas the contour method computes a stress distribution based on the deformation occurring throughout the whole section. Larger variances may result from this different method, especially in areas with varying material densities or high intergranular stress.

Similar to Brown's study, Smith et al. used both the neutron diffraction and contour methods to compare the residual stresses in nickel-based alloys used in compressor and turbine applications after friction welding. The study highlighted the substantial potential for improving accuracy and lowering measurement errors in residual stress assessments carried out using the neutron diffraction technique (Smith et al., 2017).

The main approaches for residual stress analysis are described as destructive and non-destructive experimental methods. However, the widespread development and implementation of analytical and finite element-based models have resulted from the rising costs of measuring equipment, setup, and time in industrial applications. These techniques' primary benefits are their comparatively quicker processing times and the removal of setup and measurement equipment expenses. However, their inability to replicate every aspect of actual working conditions is its worst weakness.

Analytical measurement methods have been more popular in recent years because of their comparatively low cost, which comes from quick setup and measurement durations as well as the lack of equipment and setup needs. The dependability of results has also improved due to developments in the finite element technique (FEM). Johnson et al. analyzed the occurrence of residual stresses in a gray cast iron specimen during the casting process using the Magmastress software package. To create residual stress within the component, a unique geometry known as the "Stress lattice" was used in the design of the sample parts. A thermo-elasto-plastic material model with temperature-dependent thermophysical characteristics was used in their simulations. A thermo-

elasto-plastic material model with temperature-dependent thermophysical characteristics was used in their simulations (Johnson et al., 2012).

In some of Ford's R&D engine projects, Menne et al. underlined the use of finite element modeling to forecast the final mechanical properties, residual stress distribution, and possible flaws in the casting and heat treatment processes. The study got to the conclusion that simulating the casting process using the finite element method as part of computer-aided engineering before engine block manufacture could increase product quality and durability while reducing costs and time by up to 50%. The analysis was conducted using Magmasoft software and other CAE tools; nevertheless, the report did not address specifics like modeling parameters, boundary conditions, or material attributes. However, by contrasting analysis with real test results for various aluminum casting parts, correlations were shown (Menne et al., 2007).

Long et al. compared a simulation model made with Magmasoft casting simulation software with strain gauge data obtained in a high-pressure die casting (HPDC) mold. The von Mises stresses derived from the simulation model were compared with measurements made during the casting cycle. There were differences of 10 and 40 MPa between the experimental and simulation values at the relevant locations in this investigation, which employed two rosette strain gauges. It was shown that the effects of additional factors that could not be simulated (such as mold clamping force and liquid metal pressure) on the mold were minimal (Long et al., 2013).

Jiang et al. investigated into how residual stress affected steel wheels' fatigue life. ABAQUS software was used to simulate residual stress that developed on the steel wheel's surface during rolling, and the results were compared with measurements of residual stress that were really obtained from the surface. The predicted and observed regions of stress concentration agreed well, according to the modeling results (Jiang et al., 2022).

Heger et al. used the Magmasoft and Magmastress modules to examine residual stresses resulting from non-uniform cooling produced by different wall thicknesses in large vehicle engines made up of cast iron. Through software simulations, they have

recently shown advances in forecasting stress production following material solidification, cooling, and heat treatment procedures by contrasting several design variations with the original design (Heger et al., 2019).

A considerable amount of residual stresses in aluminum cast components have been found to develop during the heat treatment process, despite the fact that residual stresses might result from a variety of manufacturing and welding techniques (Tabatabaeian et al., 2022). In heat treatment procedures consisting of solution treatment – quenching – artificial aging (e.g., T6) (Özaydın, Dokumaci, et al., 2019), residual stresses can develop within the material structure, particularly due to the high temperature gradient occurring in the short time interval between solution treatment and quenching (Tabatabaeian et al., 2022).

Li et al. investigated residual stress, microstructure, and service conditions as factors influencing the fatigue life of T6 heat-treated A356 automotive wheels. In particular, a model centered on the quenching stage was created with respect to residual stress. The areas with the greatest temperature differential during quenching were found to have the highest residual stresses. The wheel model indicates that the spoke/hub area experienced about 90 MPa (P. Li et al., 2007a).

Li et al. investigated the impact of residual stresses on fatigue life by simulating T6 heat-treated A356 automotive wheels. They contrasted the outcomes of the sectioning procedure with the obtained analysis. They observed that the machining method decreased residual stress by 10% to 20% following heat treatment. Nevertheless, they found that the fatigue life was reduced by the residual stress on the surface following machining (P. Li et al., 2007b).

Cai et al. aimed to assess the residual stress that formed in the AlSi7Cu0.5Mg (A356) aluminum alloy's T4 and T6 heat-treated stages. All approaches were similarly effective for T4-treated alloys, however the contour method and incremental hole drilling were best suited for T6-treated alloys, according to analyses utilizing various measurement techniques. They also observed the largest difference in areas with macro-porosity when comparing an analytical model with average surface displacement data (Cai et al., 2024).

Kutsal et al. simulated the T6 heat treatment process of AlSi7Mg0.3 aluminum alloy wheels and numerically calculated the residual stress values developing at different stages of the process. In the first phase of the study, microstructural examinations and mechanical tests were performed under three different conditions: as-cast, quenching, and artificial aging. Additionally, dimensional changes in three distinct regions were analyzed at each heat treatment step based on data obtained from a 3D scanner. It was observed that, following the quenching step, compressive stresses predominantly developed on the wheel surface, whereas the artificial aging step resulted in only a limited and insufficient reduction in residual stresses (Kutsal et al., 2024).

Demir et al. investigated the residual stresses developing in cylinder heads of T6 heat-treated aluminum alloy castings using the X-ray diffraction (XRD) method under different quenching media. In the study, water, polymer-modified water, and air were used as quenching environments. As expected, the highest residual stress values were observed in water-quenched specimens, while air quenching resulted in the lowest residual stress levels. Despite the advantages of air quenching, its practical applicability in industrial settings remains questionable (Demir et al., 2007).

In a report published by Alutec Belte A.G., the quenching of a V10 cylinder head subjected to T6 heat treatment was carried out in water, polymer-modified water, and a medium coded as HISAQ (High Speed Air Quenching). Residual stresses were measured experimentally using strain gauges via the hole-drilling method and were also compared analytically using Magmasoft software. Consistent with the previous study, the HISAQ quenching medium produced the lowest residual stress values (Belte, n.d.).

CHAPTER THREE
MATERIALS AND METHODS

In the first two chapters, the application areas of aluminum casting alloys in the automotive industry, the structural characteristics of casting alloys, the effects of T6 heat treatment on mechanical properties, and the mechanisms of residual stress formation were comprehensively reviewed. The literature survey indicates that the as-cast microstructures of Al–Si–Mg alloys can be effectively modified through heat treatment. Furthermore, due to the inherently high temperature gradients present during the casting process and the subsequent exposure of Al–Si–Mg alloys to heat treatment, it is necessary to systematically investigate and clearly define their effects özaon both microstructural evolution and residual stress development.

In this chapter, the present study conducted on aluminum casting materials used in the automotive industry is presented under the headings of the “Materials” and “Methods”. Methods are detailed under “casting”, “heat treatment”, and “residual stress measurement system”.

3.1 Materials

In this study, an Al–Si–Mg–based cast aluminum alloy, widely used in automotive applications, was selected. As detailed in Chapter 2, aluminum alloys with a silicon content below 12 wt.% are classified as hypoeutectic alloys, and materials for aluminum alloy wheels are included in this group. While increasing the silicon content provides benefits such as improved casting characteristics, enhanced fluidity, and better feeding behavior, silicon-rich alloys also carry the risk of reduced ductility and machinability due to the increased hardness associated with higher silicon levels (J. R. Brown, 1999).

These hypoeutectic alloys exhibit high castability, good fluidity, and a fine-grained microstructure (Özaydın et al., 2021). The selected alloy was preferred due to its widespread use in critical industrial components and its suitability for improving mechanical properties through heat treatment.

As can be seen from the aluminum–silicon phase diagram (Figure 3.1), the eutectic reaction occurs at a silicon content of 12.6 wt.% and a temperature of 577 °C (Askeland et al., 2011). This indicates that, at the eutectic composition, the microstructure transforms directly from liquid to solid during cooling. In hypoeutectic structures, however, this liquid-to-solid transformation proceeds through the formation of the primary α-Al phase prior to the eutectic reaction.

Among the other alloying elements present in the microstructure, magnesium (Mg) enhances corrosion resistance, strontium (Sr) promotes eutectic silicon modification, and titanium–boron (Ti–B) acts as a grain refiner, collectively altering the microstructure and thereby improving the mechanical properties.

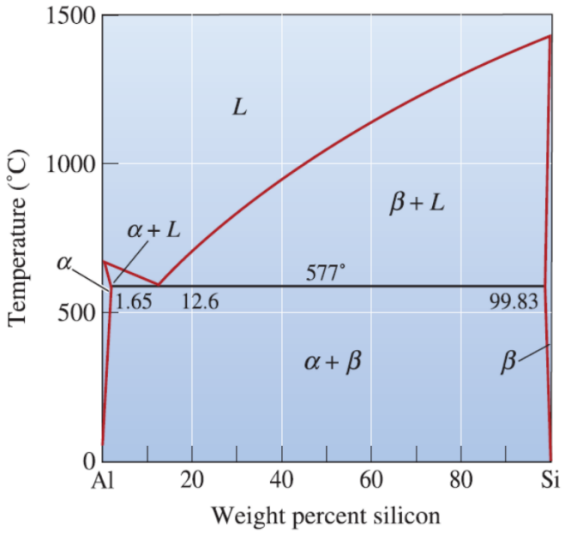

Figure 3.1 The aluminum-silicon phase diagram (Askeland et al., 2011)

When considered specifically for aluminum alloy wheel materials, it should also be noted from the phase diagram that the solidification range corresponding to silicon contents of 7 wt.% and 11 wt.% is shorter for alloys containing 11 wt.% Si. On the other hand, when the liquid-to-α-Al solid phase transformation temperatures are compared, alloys with 11 wt.% Si can be cast at lower temperatures. This characteristic may provide long-term benefits in terms of reduced energy consumption and overall cost efficiency.

With specific reference to the AlSi11 casting alloy, the microstructure of unmodified alloys is characterized by coarse, plate-like silicon phases and a brittle morphology (Figure 3.2 a–b). In the absence of modifiers such as Sr, or when the alloy is allowed to cool naturally without additional cooling arrangements, the silicon phase solidifies in a plate-like, coarse, and brittle form. This morphology contains crack initiation sites and regions of high stress concentration, thereby increasing the risk of structural damage.

In contrast, when modifiers such as Sr are introduced, the silicon morphology is altered, resulting in a modified fibrous structure (Figure 3.2 c–d). Compared to plate-like morphology, this modified structure provides significantly improved mechanical properties and enhanced castability. Owing to these pronounced differences, microstructural modification is considered essential in nearly all applications, particularly in industrial practices.

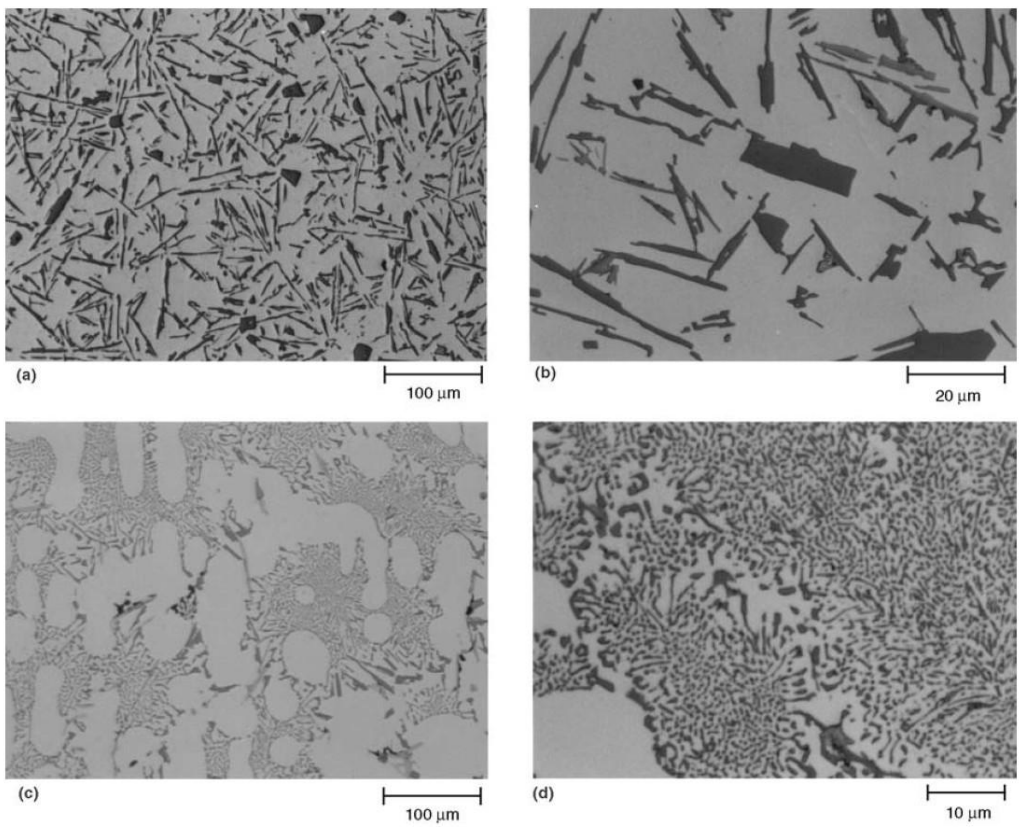

Figure 3.2 Microstructures of AlSi11 a) As-cast 150X, (b) As-cast 750X (c) As-cast modified, 150X (b) As-cast modified, 1200X (Warmuzek, 2015)

As stated in the previous section, AlSi7Mg0.3 (A356 / EN AC-42100) and AlSi11Mg (EN AC-44000) alloys are currently the standard aluminum casting alloys used for wheels (European Aluminium Association, 2011). In this study, the AlSi11Mg alloy was selected for aluminum alloy wheels, which are now offered as standard equipment in the automotive industry, primarily due to its excellent castability and superior mold-filling capability.

Although the heat-treatability of AlSi11Mg alloys is more limited compared to the alternative wheel alloy AlSi7Mg0.3, their outstanding castability significantly enhances their applicability not only for wheels with complex and complex geometries but also for non-wheel casting products such as engine components and brackets. Furthermore, the relatively limited number of industrial applications in which AlSi11Mg aluminum alloy wheels are used in the as-cast (non–heat-treated) condition, together with the corresponding gap in the literature, motivated the selection of the AlSi11Mg alloy in order to address this lack and to establish an original and novel contribution.

For this study, all specimens cast from the AlSi11Mg alloy were produced through a controlled trial casting process, prepared using process parameters similar to those utilized in standard automotive casting procedures. The chemical composition of the AlSi11Mg alloy selected for the study is presented in Table 3.1, while the mechanical properties of the alloy in the as-cast condition and after the T6 heat treatment are given in Table 3.2.

Table 3.1 Chemical Composition of AlSi11Mg Aluminum Alloy (Rheinfelden Alloys, 2016)

Chemical Composition	Si	Fe	Cu	Mn	Mg	Zn	Ti
AlSi11Mg	10.0–11.8	0.15	0.02	0.05	0.1–0.45	0.07	0.15

Table 3.2 Mechanical Properties of AlSi11Mg Aluminum Alloy (Rheinfelden Alloys, 2016)

Chemical Composition	Yield Strength [MPa]	Ultimate Tensile Strength [MPa]	Elongation [%]	Hardness Brinell [HB]
AlSi11Mg (As Cast)	80	180	3	55
AlSi11Mg (T6)	120	210	3	70

It should be noted that these values represent the minimum mechanical properties obtained from castings up to 20 mm in thickness produced using permanent molds (Rheinfelden Alloys, 2016). It should also be emphasized that the values presented in Tables 3.1 and 3.2, based on EN 1676 standards (Rheinfelden Alloys, 2016), correspond to primary aluminum casting alloys reported in the literature.

Mechanical properties may vary depending on part and mold geometry, mold material, mold cooling conditions, casting process parameters, chemical composition, and the applied heat treatment steps. All these factors will be discussed in the following "Experimental Study" section of this work, where the values obtained from specimens cast under identical conditions will be presented.

In addition to the chemical analysis values reported in the literature, major manufacturers define the allowable chemical composition limits of the materials they use in accordance with relevant standards and technical specifications and carefully monitor conformity with these limits. During production, conformity to the specified ranges should be continuously verified using chemical analysis equipment such as spectrometers, and the results should be documented and archived as traceable proof.

It has been recognized that values described in literature may differ from those defined in technical specifications or industrial standards that are employed in practical applications. In these situations, applicable standards and technical specifications—rather than values found in the literature—should serve as the controlling criteria for industrial applications.

In this study, all material supply—including aluminum alloy cast test specimens and sample wheels obtained from trial castings—was provided by "Döktaş Dökümcülük Tic. ve San. A.Ş." Therefore, it should be noted that all aluminum alloy casting materials used in this work were produced under industrial conditions in compliance with the relevant standards and technical specifications.

The industrial trial casting process begins with the melting of primary aluminum ingots and secondary aluminum, in specified proportions, in a melting furnace.

An important point that should be clarified here is the differences between the terms secondary aluminum and recycled aluminum. Secondary aluminum refers to materials generated within the same production facility, whose chemical composition complies with the relevant standards and technical specifications but cannot be used for various reasons (e.g., scrap wheels or samples rejected due to quality requirements). In contrast, recycled aluminum shows materials that may also originate from outside the production facility and may carry a risk of non-compliance with the relevant standards or technical specifications in terms of chemical composition (Karabulut et al., 2024) (Gökelma et al., 2023; Kaya et al., 2021).

As stated above, in all industrial wheel casting applications conducted in accordance with defined quality standards, compliance with the applicable standards and technical specifications is ensured through the controlled use of primary and secondary aluminum during production.

During the melting process in the furnace, specific amounts of $AlSr_{15}$ (modifier) and $AlTi_5B_1$ (grain refiner) master alloys are added to achieve the desired chemical composition and microstructure through modification and grain refinement. To remove dissolved hydrogen in the melt and potential inclusions, a degassing treatment is applied by injecting inert gas into the liquid metal. Following the degassing process, the dross and casting impurities that rise to the surface are skimmed off and removed. After these operations, the cleaned and conditioned melt is transferred via transfer ladles to the holding furnace of the low-pressure die casting machine, where it is prepared and made ready for casting.

As commonly practiced in industrial wheel casting, different materials are employed for different sections of the mold used in the low-pressure die casting machine. The wheel mold structure consists of three main components: the bottom mold, the upper mold, and the side molds. In this study, a wheel mold was used in which the bottom and upper molds were manufactured from hot-work tool steel (H13 steel), while the side molds were produced from cast iron. Although different materials may be employed for wheel molds depending on the specific design and application (Özaydın & Dikicioğlu, 2023), in general, the bottom and upper molds are exposed to higher mechanical loads and elevated temperatures compared to the side molds.

Consequently, materials with higher strength and thermal resistance are preferred for the bottom and upper molds relative to the side molds. In addition to these main components, the mold assembly also includes auxiliary elements such as the bottom plate, top plate, support columns, gating system, cooling channels, and ejector pins.

In conclusion, the AlSi11Mg alloy exhibits a lamellar microstructure due to its relatively high silicon content, and, owing to its comparatively low magnesium concentration, it demonstrates a limited potential for Mg_2Si precipitation during heat treatment. Consequently, when compared to the AlSi7Mg0.3 alloy, the achievable improvement in mechanical properties through heat treatment is relatively restricted. Nevertheless, the lamellar silicon morphology can be effectively modified through strontium (Sr) addition, leading to a more favorable microstructural configuration.

Furthermore, as indicated by the Al–Si phase diagram, AlSi11Mg undergoes a more rapid transition from the liquid to the solid phase under identical cooling conditions when compared to AlSi7Mg0.3, which provides an advantage in terms of faster solidification. Despite its hypoeutectic character, the relatively high silicon content (11 wt.% Si) places this alloy close to the eutectic composition (12.6 wt.% Si), resulting in excellent castability. These characteristics make AlSi11Mg not only suitable for aluminum alloy wheels with complex geometries, but also highly attractive for other cast components with similar geometric complexity, such as engine parts and brackets.

For these reasons, the AlSi11Mg alloy was selected for the present study. It is expected that the findings of this work will contribute to future research focusing on different geometries or alternative aluminum casting components, thereby supporting further developments in this field.

In terms of mold materials, reputable and widely used materials that are frequently utilized in the production of aluminum alloy wheels were chosen. As noted above, for the trial wheel casting, molds comparable to those employed under serial production conditions were utilized. Accordingly, the bottom and upper molds were manufactured from hot work tool steel (H13 steel), while the side molds were produced from cast iron. For the sample specimens, separate sample molds made of cast iron—similar to the side mold material—were used.

3.2 Methods

In the casting of aluminum alloy components, the selection of the casting method is determined by numerous factors, including the metallurgical and mechanical properties required from the component, its geometric characteristics, service conditions, production volume, and overall cost considerations.

In aluminum casting, permanent mold casting methods, commonly referred to as "*kokille*" casting—a term adopted from the German literature—are widely preferred. Owing to the relatively low melting and pouring temperatures of aluminum compared to cast iron and steel, mold materials such as cast iron, steel, or high-performance steels are typically selected for use as permanent molds.

With respect to the manufacturing method, gravity casting is frequently preferred, particularly for sample parts from which no functional performance is expected. Specimens produced by gravity casting are generally sufficient for chemical composition analyses and basic metallurgical analyses. However, tests aimed at determining mechanical properties—such as tensile testing and hardness measurements—as well as for localized microstructural or macrostructural analyses, the geometry of the component and its cooling characteristics have a significant influence on the results. Therefore, in such cases, it becomes essential to conduct analyses on specimens extracted directly from the wheel product itself.

Specifically for aluminum alloy wheels, although gravity casting was employed in older production technologies, this manufacturing method is considered insufficient under current technological and performance requirements.

Low Pressure Die Casting (LPDC) is still the most popular production method for aluminum alloy wheels, despite the emergence of several manufacturing techniques due to technological advancements.

In this section of the study, the wheel manufacturing process using the Low Pressure Die Casting (LPDC) method for aluminum alloy wheels is described in detail. Subsequently, the heat treatment steps and application procedures aimed at enhancing the mechanical properties are presented. Finally, the residual stresses influenced by

the thermal effects induced by the heat treatment processes, along with the corresponding measurement methods, are discussed in detail.

3.2.1 Casting

With recent advancements in manufacturing technologies, alternative production methods such as forging (Kim et al., 2002); (Yang et al., 2025) and high-pressure die casting (Işık et al., 2020) have also been applied in the production of aluminum alloy wheels. Nevertheless, particularly in cases where high production volumes and cost-effective manufacturing are critical, the Low Pressure Die Casting (LPDC) method clearly stands out among these alternatives and remains the most widely preferred production technique.

At this stage of the study, the production methods of aluminum alloy wheels relevant to this research are detailed with a specific focus on the Low Pressure Die Casting (LPDC) method. The manufacturing process of aluminum alloy wheels essentially involves melting aluminum ingots and transforming the molten metal into the final wheel product. Undoubtedly, this process includes a wide range of parameters, highlighting the inherent difficulty of achieving consistency and repeatability in casting operations.

There are five primary steps in the entire production process: Melting, low-pressure die casting, heat treatment, machining, and coating. Each of these primary stages further includes several sub-processes. For instance, the melting stage includes metallurgical inspection and degassing operations; the low-pressure die casting stage includes mold manufacturing and preparation processes; the machining stage involves sub-processes such as bolt and valve hole drilling, three-dimensional dimensional measurements, and helium leakage testing; and the coating stage includes diamond polishing as well as coating and mechanical testing operations (Figure 3.3).

Although it is not feasible to simultaneously evaluate all parameters associated with these main and sub-processes, the parameters related to the melting and low-pressure die casting stages are known to have a more pronounced influence on the final product quality compared to the others. Therefore, careful control and monitoring of the practices implemented during these stages are of critical importance.

Obtaining aluminum ingots is the first step in the production process, as shown in Figure 3.3. The ingots that pass incoming inspection tests and satisfy the quality standards are moved to the melting furnace, where the first stage of the workflow—known as the "melting" stage—begins.

3.2.1.1 Melting

As previously stated, dedicated melting furnaces are available for the two primary aluminum alloys accepted by major automotive manufacturers for aluminum alloy wheel production, namely AlSi7Mg and AlSi11Mg. At this stage, secondary aluminum material may also be charged into the melting furnace, provided that the chemical composition limits specified by the relevant standards are satisfied. The critical consideration here is the clear differences between secondary aluminum and recycled aluminum, and the necessity to avoid the use of recycled aluminum with uncertain or uncontrolled chemical composition in the melting furnace at this stage.

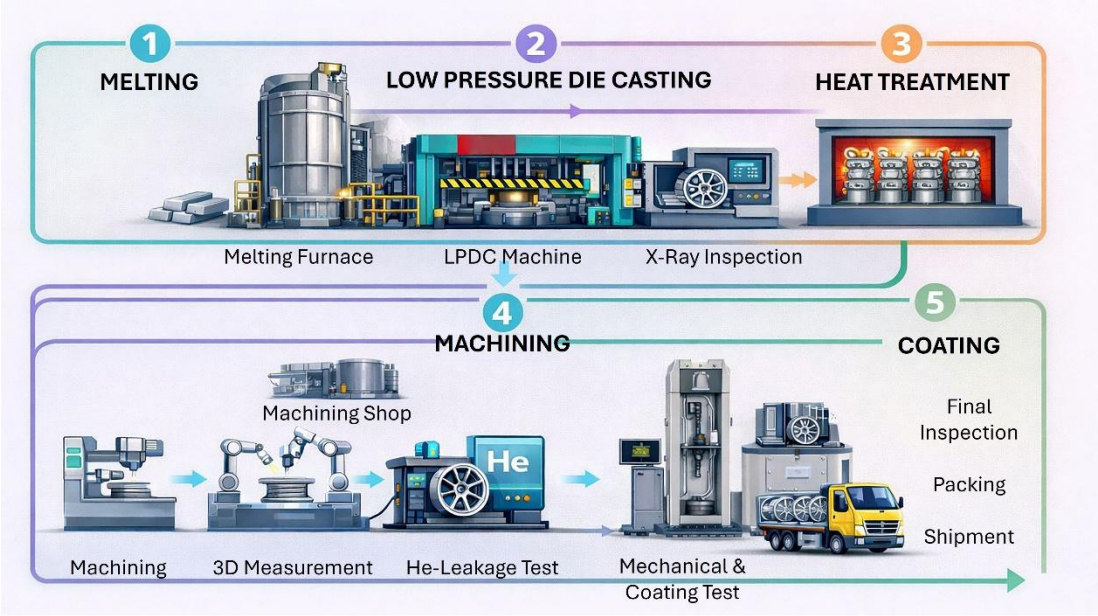

Figure 3.3 Aluminum alloy wheel production process flowchart

During the melting process, the chemical composition in the melting furnaces is periodically monitored to ensure compliance with the applicable standards and specifications and to remain within the defined compositional limits. Maintaining chemical conformity at this stage is critical for ensuring the suitability of the final

casting's chemical composition. Once the chemical composition of the molten metal has been verified, the melt is transferred from the melting furnace into a transfer ladle for delivery to the low-pressure die casting machine. At this stage, the necessary material additions are introduced to enhance the metallurgical and mechanical properties of the alloy. These additions can be categorized according to their primary functions as grain refinement, modification, and alloying.

Grain refinement is a necessary process to prevent the formation of brittle intermetallic phases and porosity, which are prone to develop within coarse and large-grained microstructures. The reduction of intermetallic phases and porosity contributes directly to improvements in mechanical properties and fatigue resistance. Grain refinement is performed by reducing grain size and increasing the number of grain boundaries, thereby delaying the propagation of dislocations and damage within the microstructure and enhancing overall mechanical strength.

The grain refinement mechanism is based on the presence of numerous titanium aluminide ($TiAl_3$) crystals within Al–Ti–B master alloys, which generate many nucleation sites when added to the molten metal. As the $TiAl_3$ crystals partially dissolve in the aluminum melt, they create a titanium-rich liquid phase. According to the Al–Ti phase diagram, the addition of titanium increases the melting temperature of aluminum, and within this temperature range, primary nucleation occurs, leading to the formation of aluminide particles. In subsequent stages, these particles act as nuclei for dendrite growth, and as solidification progresses, the dendrites grow and solidify throughout the entire structure (Sigworth & Kuhn, 2007).

Titanium and boron-based grain refiners are most used in the form of $AlTi_5B_1$ rods. It should be emphasized that, in all applications, the additional levels of these refiners must be strictly controlled and kept below specified limits in accordance with the relevant standards and technical specifications.

The modification process is based on transforming coarse, plate-like or acicular morphologies into more rounded forms. Similar to grain refinement, this approach can be explained by the principle of hindering the motion of dislocations and the progression of damage within the microstructure. Among the elements used for

modification, strontium (Sr) based modifiers—most applied in the form of $AlSr_{15}$ rods—are the most widely preferred in industrial practice. The addition of Sr not only enhances the ductility of the alloy but also leads to significant improvements in mechanical properties, which accounts for its widespread use.

Modification is typically achieved by adding Sr to the alloy in the range of 250–300 ppm; however, studies reported in the literature indicate that levels as low as 50 ppm may also be sufficient to obtain an effective modification (Duygun, 2017). In an industrial wheel application, the influence of Sr content on mechanical properties was investigated at levels of 450 ppm, 425 ppm, 400 ppm, 375 ppm, 225 ppm, and 140 ppm. At all investigated levels, effective Sr modification was achieved, and no acicular silicon morphology was observed. Instead, the modified microstructures exhibited the so-called Chinese script morphology (Özaydın et al., 2018).

In addition to the Sr content within the alloy, the holding time of the Sr-modified melts prior to casting significantly affects the effectiveness of modification. It has been demonstrated in the literature that Sr oxidizes and is gradually lost from the melt during extended holding at elevated temperatures, leading to a reduction in the modification effect. For instance, in a previous study on AlSi7Mg alloy held at 720 °C, the initial Sr content of 450 ppm decreased by approximately 50 ppm to about 400 ppm after three shifts (24 hours), and a similar decreasing trend continued with increasing holding time (Özaydın et al., 2018).

Elements such as sodium (Na), calcium (Ca), and antimony (Sb) are also known to provide modification effects like Sr. However, when all modifiers are compared, Na is known to exhibit a short-lived modification effect (Lipiński & Szabracki, 2015), while Ca and Sb have been shown to provide relatively weak modification effects compared to other alternatives (Kaufman & Rooy, 2004). Due to the transient nature of Na modification and the comparatively limited effectiveness of Ca and Sb, strontium remains the preferred modifier in serial production and industrial casting applications.

Magnesium is added to the melt to complete the alloying process. Magnesium in the alloy contributes to the formation of the Mg_2Si phase during heat treatment, which

increases hardness and promotes improvements in mechanical properties, particularly ultimate tensile strength (UTS) and yield strength (YS). In AlSi11Mg alloys, the high silicon content leads to excessive formation of eutectic silicon; this condition reduces the effectiveness of magnesium and silicon in precipitation hardening (Kaufman, 2000).

For AlSi11Mg alloys, the magnesium content is typically expected to remain within the range of 0.10–0.45 wt.% (Table 3.1). When the magnesium level exceeds this range, excessive Mg_2Si phase formation may occur, which can adversely affect mechanical properties. For this reason, the magnesium content is strictly limited within specified boundaries. An excessive amount of Mg_2Si not only deteriorates mechanical properties but may also negatively influence impact toughness.

In the final phase of the "Melting" stage, a degassing process is applied to the molten metal that has already undergone grain refinement, modification, and alloying, with the primary objective of melt cleaning. The purpose of degassing is to remove dissolved hydrogen, oxides, dross, and other non-metallic inclusions from the molten aluminum (Özaydın, Kaya, et al., 2019).

Degassing is typically performed by injecting an inert gas into the melt through a rotor, which generates fine and uniformly distributed gas bubbles within the liquid metal. These bubbles facilitate the transport of undesirable constituents—such as hydrogen, oxides, and inclusions—to the melt surface, where they can be removed. Among the inert gases commonly used, nitrogen (N_2) and argon (Ar) exhibit nearly identical metallurgical effects; however, due to its significantly lower cost, nitrogen is widely preferred in industrial applications. Consequently, nitrogen degassing is routinely employed to reduce hydrogen content in the melt and thereby minimize casting defects such as porosity and oxide-related defects.

Although industrial degassing practices often focus primarily on hydrogen removal because of its direct contribution to porosity formation, a more critical concern lies in the presence of oxide films. These oxide layers may remain floating in the melt rather than rising to the surface because their density is like that of molten aluminum. For this reason, degassing should be regarded not only as a hydrogen removal process, but

as a comprehensive molten metal cleaning operation. The generation of uniformly distributed fine gas bubbles is essential to effectively eliminate both dissolved hydrogen and suspended oxide films from the melt. If these issues are not sufficiently resolved, hydrogen-induced porosity and serious casting defects related to oxide inclusions will unavoidably occur.

In addition to degassing efficiency, melt handling practices play a crucial role in oxide control. Aluminum oxide films can reform rapidly on the melt surface, and turbulent flow during transfer operations significantly increases the risk of reintroducing these oxides into the liquid metal. Therefore, minimizing turbulence during melt transfer is of vital importance. Ideally, the transfer distance between the melting furnace and the holding furnace of the low-pressure die casting machine should be minimized, and the transfer process should be conducted under low-turbulence or turbulence-free flow conditions to preserve melt cleanliness and casting quality.

3.2.1.2 Low Pressure Die Casting

Before proceeding to the low-pressure die casting stage, the mold designed for the specific wheel model must be fully prepared and mounted onto the casting machine. The wheel mold assembly consists of three main components: the bottom die (core), the upper die (core), and the side dies (cores).

The bottom core forms the styling surface of the wheel, which corresponds to the visible area observed by the end user when the wheel is mounted on the vehicle. Consequently, it represents both the most critical mold component and the region most heavily exposed to the thermal and mechanical loads imposed by the weight and temperature of the molten metal during casting. As noted in the “Materials” section of this study, the bottom core is typically manufactured from hot-work tool steels, such as H13 steel, or from commercially available equivalents that provide comparable high-temperature strength and thermal fatigue resistance.

The upper core forms the offset region of the wheel, which interfaces directly with the vehicle assembly. Similar to the bottom core, the upper core is also commonly

produced from H13 hot-work tool steel due to its ability to withstand repeated thermal cycling and mechanical loading.

Finally, the side cores define the rim region of the wheel, which provides the seating surface for the tire. These components are generally machined from cast iron, as this material offers adequate thermal conductivity, wear resistance, and dimensional stability for the rim geometry.

In addition to these primary mold components, the mold assembly incorporates several auxiliary elements that enable secure installation and precise alignment on the low-pressure die casting machine. These include structural and positioning components such as the upper and lower plates, bridges, pillars, upper and lower pusher plates, centering shafts, centering bushings, and pins (Figure 3.4) (Aydın et al., 2021).



Figure 3.4 Mold sample for aluminum alloy wheel (Aydın et al., 2021)

After the mold preparation is completed, die coating (commonly referred to as refractory coating and marketed under various commercial names) can be applied to the surfaces that will come into direct contact with the molten metal. The primary objectives of die coating applications include ease and speed of application, extended service life of the mold, and the achievement of superior surface quality on the cast component.

In addition to these benefits, die coating treatments are known to positively influence mold filling behavior and molten metal flow characteristics by reducing

metal–die interaction and improving wettability conditions. Consequently, such coatings contribute to more stable filling conditions and improved casting quality (Kaya et al., 2019).

After the prepared mold is mounted onto the low-pressure die casting (LPDC) machine, the molten metal is transferred. Following the degassing process, the cleaned molten aluminum is transferred to the LPDC machine via a transfer ladle. The metal delivered to the holding furnace of the LPDC machine is maintained at a casting-ready temperature of 720 ± 10 °C.

To prevent any adverse effects on the grain refinement, modification, and alloying treatments—and to avoid unnecessary prolongation of the overall process time—the wheel casting operation is initiated immediately after metal transfer.

After the metal transfer, a cross-sectional view of the low-pressure die casting machine is shown schematically in Figure 3.5, illustrating the main components and process configuration.

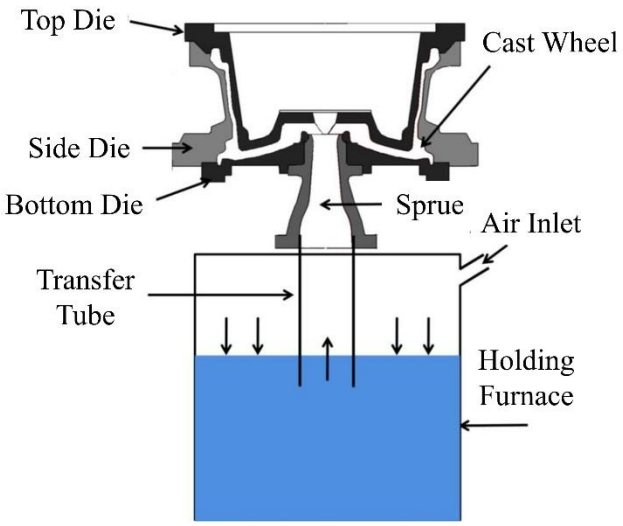

Figure 3.5 Illustration of the low pressure die casting process (Duan, 2016)

Wheel casting is performed by applying low pressure (approximately 1 bar) to the holding furnace, causing the molten metal to rise through the transfer tube, pass through the sprue, and fill the mold cavity (Figures 3.5 and 3.6). After the mold filling

is completed, the solidification process begins, resulting in the formation of the cast wheel.

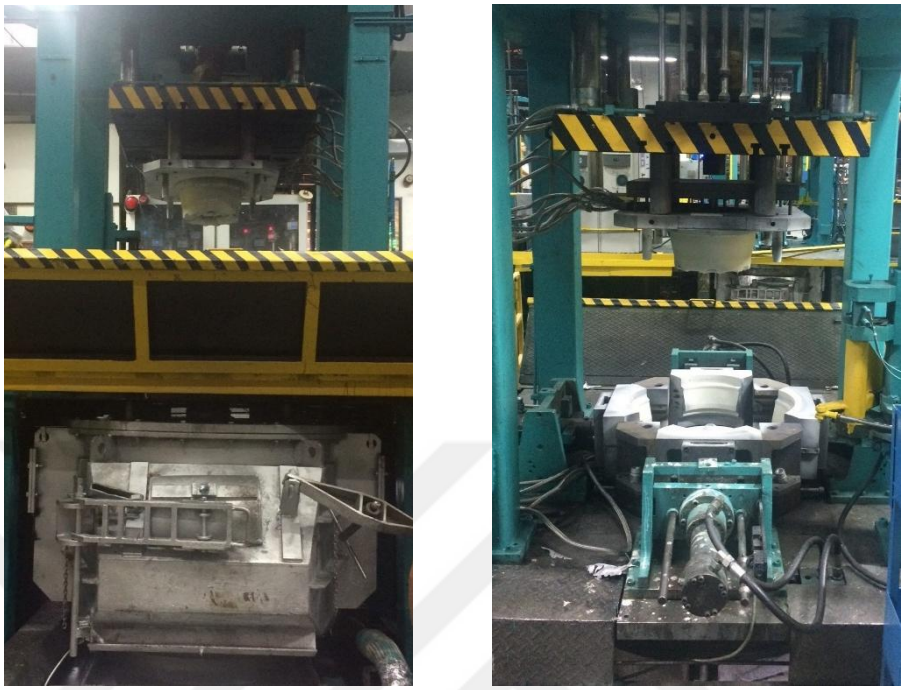

Figure 3.6 Low-pressure die casting machine (Özaydın, 2019)

During the solidification stage, achieving directional solidification is a critical requirement to minimize internal casting defects. Directional solidification should proceed from the region that solidifies first toward the region that solidifies last. In aluminum alloy cast wheels, this direction is ideally established from the inner flange region toward the hub region. Such a solidification path ensures that the semi-solid (mushy) zone within the wheel remains continuous during cooling, thereby reducing the likelihood of porosity and shrinkage-related casting defects.

To achieve this controlled solidification behavior, wheel molds are equipped with dedicated cooling channels strategically positioned within the mold structure. In conventional designs, these channels are typically implemented as cooling pipes embedded within the mold, through which air, water, or mist (air–water mixture) is circulated to control local cooling rates and promote directional solidification (Özaydın & Çatal, 2019a). The geometry and placement of these cooling channels are tailored to the specific wheel design, and the selection of cooling media—air, water,

or mist—can significantly influence both cooling efficiency and overall process stability (Özaydın et al., 2022).

Beyond conventional approaches, advanced manufacturing techniques enable the development of optimized cooling channel geometries and mold cavity designs that enhance heat transfer efficiency. Such designs allow more effective cooling with reduced coolant consumption (e.g., air-only systems), resulting in improved thermal control and increased process efficiency (Kırmızıgöl et al., 2024).

Although process parameters vary depending on the specific wheel design, the overall cycle time typically ranges between 300 and 330 seconds. Following completion of the solidification stage, the side cores and upper core are separated, allowing removal of the cast wheel from the mold.

At this stage of the operation, the cast wheel remains at a temperature too high to permit manual handling. Specifically, the wheel cannot be safely removed from the machine by the operator for gross flash removal or for the application of required brand and identification markings, which are integral to the production process. Therefore, in order to enable the subsequent operation referred to as “handling,” the cast wheel is immediately transferred into a water tank, after which the handling operation is performed.

The primary purpose of this initial cooling step is occupational health and safety, rather than metallurgical conditioning. However, this safety-driven practice introduces a critical thermal shock condition: the wheel, at an internal temperature of approximately 300–400 °C, is rapidly immersed in cooling water at 70–80 °C. Such an unexpected temperature gradient can significantly increase residual stresses within the casting.

When residual stresses develop in critical regions of the wheel, they may contribute to the initiation or propagation of micro- or macro-scale cracks, particularly in conjunction with other potential root causes inherent to the casting process. Consequently, this rapid post-casting cooling step may elevate the risk of cracking and structural damage in the final wheel product.

This situation clearly demonstrates that residual stresses, which constitute one of the primary focused points of the present study, represent a significant risk factor and may lead to various forms of structural damage, potentially extending to material damage. Accordingly, residual stresses should be regarded as a critical phenomenon that must be quantitatively measured as a first step and subsequently reduced through appropriate preventive measures.

Following the handling operation—during which marking and the removal of coarse flash are performed—the cast wheels are subjected to visual inspection and subsequently transferred to the next operation for X-ray inspection. Given that wheels are safety-critical components in the automotive industry, cast wheels are subjected to 100% X-ray inspection after casting. All potential casting defects, including porosity, oxide inclusions, and other internal discontinuities, must be thoroughly evaluated.

Since conventional X-ray inspection provides a two-dimensional image, systems equipped with movable X-ray heads or part manipulation mechanisms are commonly employed. These configurations enable more detailed examination of internal casting defects from multiple orientations. In cases where conventional X-ray inspection is insufficient, advanced non-destructive evaluation techniques, such as computed tomography (CT) scanning, may be utilized to obtain a more comprehensive three-dimensional assessment of internal defects (Zanchini et al., 2023).

Following X-ray inspection, a hub drilling operation is applied to remove the filter located in the hub region of the wheel. These filters are designed to capture oxides and inclusions that may be present in the molten metal during casting. Depending on production requirements, either metallic or ceramic filters may be used; however, in industrial practice, metal filters are generally preferred due to their cost-effectiveness.

After X-ray inspection and filter removal, wheels that meet the specified acceptance criteria proceed along the acceptance conveyor, while non-conforming wheels are collected on the reject conveyor. These rejected wheels are subsequently returned to the main melting furnace for reuse as secondary aluminum, thereby contributing to material efficiency and recycling within the production process.

In the conventional approach, wheels subjected to heat treatment are typically manufactured from AlSi7Mg0.3 alloys, whereas AlSi11Mg alloy wheels are generally not heat treated. However, in recent years, the increasing complexity of wheel and engine component geometries has led to a growing demand for alloys with high fluidity. As a result, for such complex and complex components, castability has, in some cases, become more critical than achieving the highest possible mechanical properties.

Considering the requirements and limitations enforced by original equipment manufacturers (OEMs) in the automotive industry, these castability demands are more effectively satisfied by AlSi11Mg alloys. Consequently, in contrast to traditional practices, recent industrial trends have increasingly involved the application of heat treatment to AlSi11Mg alloys, enabling their use in components where both high castability and enhanced mechanical performance are required.

3.2.1.3 Heat Treatment Process

As widely reported in the literature and commonly practiced in industrial applications, wheels produced by the Low Pressure Die Casting (LPDC) process are subjected to T6 heat treatment. This heat treatment sequence consists of solution treatment, quenching, and artificial aging, which will be discussed in technical detail in the following section.

In this section, the process steps and application methods will be detailed with a focus on industrial practice. For industrial heat treatment operations, dedicated heat treatment facilities are employed to ensure process consistency and compliance with required metallurgical standards.



Figure 3.7 Example of a heat treatment facility (Özaydın, 2019)

As shown in Figure 3.7, the process steps within the heat treatment facility begin after the hub drilling operation, which is performed to remove the filters located in the hub region of wheels produced by the low-pressure die casting method. Following the removal of remaining flash, the as-cast wheels undergo visual inspection and heat treatment marking. Subsequently, they are transferred in batches to the heat treatment facility via a conveyor system for the solution heat treatment stage. As expected, the wheels are loaded into the heat treatment facility with their styling surfaces facing upward.

During the solution heat treatment process, the wheels are exposed to a temperature of approximately 535 ± 5 °C for more than three hours. Immediately thereafter, the wheels are subjected to water quenching by immersion in a water tank maintained at 80 ± 5 °C. Following quenching, the wheels are transferred to an artificial aging furnace, where they are held at 155 ± 5 °C for approximately two hours, thereby completing the heat treatment cycle. After the completion of heat treatment, the wheels proceed to the machining stage.

3.2.1.4 Machining

After completion of the casting and heat treatment processes, the as-cast wheels still contain features such as the rim section, bolt holes, casting shrinkage allowance, and

machining allowance. In order to bring the wheels to the dimensions defined in the technical drawings, a machining process is applied. Through this process, the as-cast wheel is transformed into a finished wheel.

The machining process consists of three main stages. In the first operation, the wheel is clamped from the styling surface, allowing the rim to be machined. In the second operation, the wheel is clamped from the inner flange, and the remaining unmachined sections of the rim are shaped using machining methods. In the third and final operation, the bolt holes and valve hole, which are in a closed form in the as-cast condition, are drilled to achieve their final geometry.

Following these operations, deburring and finishing processes are performed, after which the machining process proceeds to the inspection stages. Within the scope of quality control, all wheels undergo balance inspection, and 100% leak-tightness testing is conducted using a helium leakage test, as illustrated in Figure 3.8.

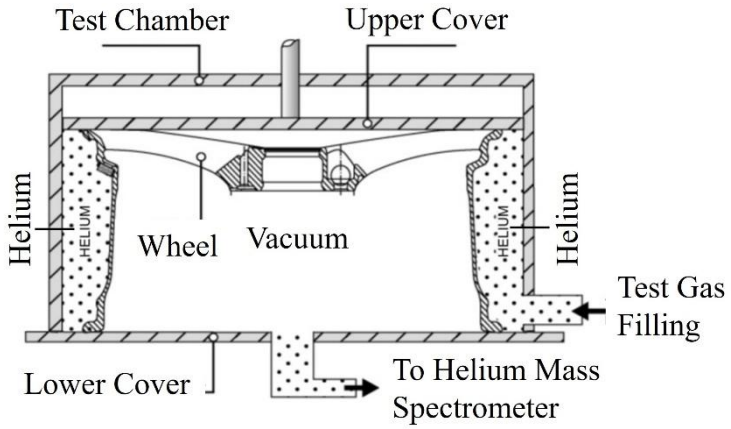

Figure 3.8 Schematic view of Helium leakage test (Grubisic, 2017)

The leak-tightness test is performed using helium, which is one of the gases with a very small molecular size. During the test, the rim surface, styling surface, and valve regions are sealed, after which helium gas is introduced into the system. Deviations observed on the measurement indicator are evaluated to determine whether any gas leakage occurs through the rim surface. Finally, dimensional accuracy inspections and

brushing operations are carried out, and upon completion of these steps, the machining process is concluded.

3.2.1.5 Coating

Following the leak-tightness (He-leakage) and dimensional accuracy inspections, the process proceeds to the coating stage, which represents the final step of the casting process. The coating operation consists of three main stages: powder coating, wet coating, and varnish application.

Prior to coating, the wheels are thoroughly cleaned using various chemical agents to remove any residual chips, coolant fluids, dirt, or oil remaining from the machining process, thereby preparing the surface for coating.

The first stage, powder coating, is applied to protect aluminum—naturally susceptible to oxidation under corrosive environmental conditions—from external degradation. At this stage, no coloration is intended; the primary objective is only to provide corrosion protection for the wheel.

The second stage, wet coating, is the coloring process performed according to customer requirements. Although various applications have emerged in recent years, wet coatings are predominantly applied in aluminum-tone colors, most commonly gray, black, or white.

Before proceeding to the third stage, an additional processing step is introduced for “diamond-cut” wheel designs, which have experienced high demand in recent years. In this case, the wheels are returned to the machining shop, where the styling surfaces are machined at the diamond-cut station to process the specified regions. Immediately following this operation, the process continues directly to the third stage, varnish application.

At this stage, mechanical tests and coating quality tests are conducted at specified intervals in accordance with relevant standards and technical instructions. While these requirements apply to wheels in series production, projects in earlier phases—such as product launching and pre-production stages—are subjected to significantly more frequent testing and inspection procedures.

In the final step, the wheels undergo visual inspection, after which they are packaged and transferred to the warehouse to be prepared for shipment. Thus, the material initially supplied in ingot form is ultimately transformed into a finished wheel product upon completion of all production stages.

3.2.2 Heat Treatment

Heat treatment is one of the fundamental methods applied to tailor the microstructure of materials to enhance their mechanical properties. Although the process steps of industrial-scale heat treatment have been presented in the previous section of this study, heat treatment is examined under the main headings of the "Methods" section for two primary reasons. First, it is an indispensable industrial practice for improving mechanical performance. Second, it involves exposure to multiple and significantly different temperature regimes, which provide a critical basis for the formation of residual stresses, one of the main focal points of this study.

Within this section, the microstructural transformations occurring during each heat treatment stage are discussed in detail, along with the specific process steps that contribute to the generation of residual stresses.

The temperature gradients that may lead to the formation of residual stresses begin, as previously noted, during the cooling stage carried out to enable "handling" of the as-cast wheel. In this step, the cast wheel, at an approximate temperature of 300–400 °C, is cooled in a water bath at around 70–80 °C. Although this operation does not constitute a heat treatment process in the conventional sense, it represents a critical stage that should not be overlooked under industrial production conditions.

Consequently, even in the absence of any subsequent heat treatment applied to the as-cast wheel, the potential risk associated with residual stresses must be recognized. The severe and rapid temperature change introduced at this stage may initiate or propagate microcracks and can contribute to structural damage within the material.

Another critical process step that can contribute to the formation of residual stresses is heat treatment. Among the heat treatment stages, those involving the largest temperature differentials present the highest risk for residual stress development.

Depending on the applied procedure, heat treatment may consist of solution treatment followed by quenching and artificial aging, or only artificial aging.

In particular, the substantial temperature difference between the solution treatment and the quenching stage constitutes the most critical phase in terms of residual stress formation. In contrast, the artificial aging step, due to its application characteristics, resembles a stress-relief heat treatment and therefore tends to reduce residual stress levels within the material.

The first stage of the T6 heat treatment is the solution treatment, which is conducted below the eutectic temperature indicated in the phase diagram (Figure 3.1, 577 °C), typically within the temperature range of 530–550 °C. Following the solution treatment, quenching is performed in water at a temperature of approximately 70–80 °C. After quenching, artificial aging is applied at temperatures between 150 °C and 170 °C to achieve the desired mechanical properties.

During the solution treatment, silicon and magnesium present in the microstructure contribute to the formation of the Mg_2Si phase, while during the aging treatment this phase precipitates between the aluminum dendrites, leading to an increase in mechanical properties and hardness values (Güven, 2005). In this context, particularly for alloys with high silicon content, higher magnesium additions may promote the formation of Mg_2Si and thereby enhance mechanical properties. However, it should be noted that excessive magnesium additions can result in an overabundance of the Mg_2Si phase, leading to excessively high hardness levels and reduced impact toughness. Therefore, the magnesium content must be carefully controlled and limited within appropriate ranges.

The primary objective of the solution heat treatment is to promote the dissolution of the silicon (β) phase present in the microstructure into the aluminum (α) matrix without reaching the melting state of the alloy. The subsequent rapid cooling is intended to preserve the homogeneity of the resulting microstructure. To prevent the transition of the alloy into the liquid phase during solution treatment, the processing temperature must be maintained below the eutectic temperature of 577 °C (Figure 3.1). In industrial practice, this temperature range is typically selected between 530 °C and

550 °C. The duration of the solution treatment varies depending on the component geometry and section thickness. For a wheel with average dimensions, the solution treatment time is generally applied within the range of 3–4 hours (Özaydın, 2019).

The quenching process is based on the rapid cooling of the aluminum (α) phase obtained during solution heat treatment, in a manner that prevents the re-nucleation of the silicon (β) phase. To effectively suppress the formation of β-Si phases, cooling is most efficiently achieved through water quenching. In contrast, when cooling is performed at a slower rate—such as air cooling—the re-precipitation of silicon (β) phases within the microstructure may occur.

Although water quenching provides the advantage of rapid cooling, it may also lead to distortion and the development of internal stresses due to the high temperature gradients involved (Özaydın & Çatal, 2019b). This condition promotes the formation of residual stresses within the material, which should be carefully considered, as such residual stresses can increase the risk of fatigue damage in components subjected to cyclic loading conditions (Özaydın, 2019). For these reasons, the appropriate selection and control of the quenching temperature are of critical importance.

The artificial aging treatment promotes the stable and controlled precipitation of Si (β) phases that remain dissolved within the Al (α) matrix after the quenching process. Under natural aging conditions at room temperature, this precipitation mechanism proceeds very slowly or may not occur at all due to insufficient time. In order to accelerate this process and ensure the controlled formation of Si (β) phases, artificial aging conditions are established by holding the material at an elevated temperature rather than at ambient conditions (J. R. Brown, 1999) .

In industrial-scale applications where heat treatment procedures similar to the T6 condition are applied, aluminum alloy wheels are subjected to heat treatment in industrial facilities. Typical processing parameters reported in the literature include a solution treatment at 535 ± 10 °C for 210 minutes, followed by water quenching at 65 ± 10 °C for 1 minute, and subsequent artificial aging at 165 ± 10 °C for 120 minutes (Kutsal et al., 2024).

Similarly, in industrial applications corresponding to the T5 heat treatment condition, there are cases where the solution treatment and water quenching steps are bypassed, and only artificial aging is applied. In an aluminum alloy wheel application, artificial aging treatments conducted at temperatures of 200 °C, 250 °C, and 300 °C for durations of 30 and 180 minutes have been investigated. According to the reported results, the highest ultimate tensile strength and yield strength values were obtained at the lowest artificial aging temperature of 200 °C combined with the longest aging duration of 180 minutes (Özaydın, 2022).

In the context of this study, the specific heat treatment conditions applied to the aluminum alloy wheel samples will be presented in detail in the "Experimental Study" section. All heat treatment processes were carried out in an industrial heat treatment facility operating in accordance with relevant standards, specifications, and technical procedures.

To ensure that the sample wheels closely represent real industrial applications, the heat treatments were performed under mass production conditions, together with serial production wheels. The sample wheels were subsequently distinguished from serial production wheels through dedicated marking and identification procedures. To obtain homogeneous and reproducible results, particular attention was paid to ensuring that all sample wheels belonged to the same production and heat treatment batch. In this manner, potential variations arising from process-related differences were minimized.

3.2.3 Residual Stress Measurement System

Residual stresses can be defined as elastic stresses that remain within a material in a non-uniform manner because of manufacturing processes and heat treatment operations. Residual stresses may arise due to mechanical actions and/or thermal effects, and their evaluation requires either direct measurement using appropriate techniques or indirect determination through analytical and numerical methods. Accordingly, residual stress assessment can be performed using destructive or non-destructive measurement techniques, while analytical approaches are employed for calculation and simulation purposes.

One of the most critical characteristics of residual stresses is that they exist within the material in the absence of any external mechanical load or thermal gradient. These internally stored stresses can become particularly critical in components operating under fatigue loading conditions, where they may promote crack initiation and propagation, thereby adversely affecting structural integrity. For this reason, the measurement and control of residual stresses are of vital importance, especially for safety-critical components in the automotive industry.

As discussed in the previous section, not only the magnitude of residual stresses but also their nature—whether tensile or compressive—constitutes a key parameter influencing component performance. From the initial design stage through manufacturing and testing, the presence and distribution of tensile or compressive residual stresses can significantly affect component behavior and service life. When considered collectively, residual stress measurement systems extend beyond providing quantitative values; they become a critical factor influencing the entire product lifecycle, from design and manufacturing processes to validation and testing conditions.

Residual stresses, which can be examined at both macro- and micro-scales, are commonly classified into three distinct stress levels. The first category, referred to as Type I residual stresses, consists of macroscopic stresses that develop during manufacturing processes over length scales larger than the grain size. The second category, known as Type II residual stresses, corresponds to microscopic stresses that form at the grain scale as a result of manufacturing processes. The third category, Type III residual stresses, represents micro-level stresses that originate from crystal defects within individual grains (Tabatabaeian et al., 2022).

In addition to arising from various manufacturing and welding processes, it has been reported that a significant portion of residual stresses in aluminum cast components develops during heat treatment operations (Tabatabaeian et al., 2022). In heat treatment sequences involving solution treatment, quenching, and artificial aging—such as the T6 heat treatment condition—residual stresses are particularly prone to form during stages characterized by rapid and substantial temperature changes over short time intervals. Among these stages, the transition between solution

treatment and quenching is especially critical. The residual stresses generated during this step may predominantly manifest as Type I residual stresses, occurring at the macroscopic scale within the component (Tabatabaeian et al., 2022).

Residual stress measurement techniques are classified in the literature under various categories such as “destructive,” “semi-destructive,” and “non-destructive” methods (Tabatabaeian et al., 2022). However, in general practice, these techniques are most commonly grouped into two main categories: destructive and non-destructive measurement methods (Rossini et al., 2012). In recent years, with the advancement of finite element methods and computational approaches, a third category—referred to as analytical methods—can also be incorporated into this classification as a complementary measurement and evaluation approach (Rossini et al., 2012).

3.2.3.1 Destructive Measurement Techniques

In destructive residual stress measurement techniques, the fundamental principle is based on releasing the stresses present in the component through various mechanical approaches and subsequently measuring the resulting response. By evaluating the deformation or displacement of the affected region, the residual stress state can be determined according to established mechanical principles (Guo et al., 2021). These mechanical techniques are also referred to as stress-relaxation methods and rely on analyzing the amount of relaxation induced by material removal from the metal component. Residual stresses are evaluated by comparing the mechanical state of the part before and after the applied mechanical intervention (Rossini et al., 2012). When destructive techniques are applied using mechanical relaxation methods, the measurements cannot be repeated on the same component, and many specimens are therefore required (Tabatabaeian et al., 2022).

Although destructive techniques may initially appear less attractive due to the damage they cause to the specimens, they stand out as a favorable option because of their versatility and reliability (Schajer, 2010). Destructive and semi-destructive techniques are generally recognized as cost-effective methods that do not require high-end technological infrastructure (Wong & Hill, 2013). In destructive residual stress measurement methods, the damage introduced into the tested component—typically

in the form of deformations resulting from incremental material removal—can be quantified using strain gauges or optical techniques such as Digital Image Correlation (DIC) (Tabatabaeian et al., 2022).

With respect to the techniques they include, the classified methods include the hole-drilling method, the ring-core method, the deep hole drilling method, the contour (section profile) method, and the sectioning method, all of which are categorized under destructive residual stress measurement techniques.

3.2.3.1.1 Hole Drilling Method

Despite the different terminologies encountered in the literature—such as "central or blind hole drilling" (Shokrieh & Ghasemi K., 2007) or "incremental or deep hole drilling" (Ghasemi et al., 2014) —the method defined as the hole drilling method in the relevant standard (ASTM, 2020) is based on bonding a strain gauge rosette to the surface of an isotropic and linearly elastic material, incrementally drilling a hole at the center of the rosette, and measuring the resulting strain relaxations. The residual stresses within the drilled volume are then calculated using equations derived from linear elasticity theory, based on the measured relaxed strains (ASTM, 2020).

Residual stresses are determined from the strain values measured around the drilled hole by applying appropriate calibration coefficients. These coefficients are selected according to the type of strain gauge rosette used and the analysis method that best represents the expected stress state (Kandil et al., 2001). Figure 3.9 schematically illustrates the strain gauge rosettes.

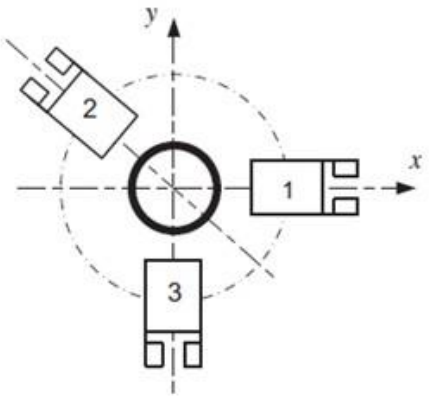

Figure 3.9 Typical geometry of a rosette (Akbari et al., 2014)

In Figure 3.9, the centrally drilled hole region is defined as such that the positive x-direction aligns with the axis of strain gauge 1, while the negative y-direction aligns with the axis of strain gauge 3. The strain relaxations released because of the drilling process are recorded simultaneously by the three strain gauges (Akbari et al., 2014). Figure 3.10 schematically presents the rosette positioning and the hole-drilling region in a three-dimensional representation.

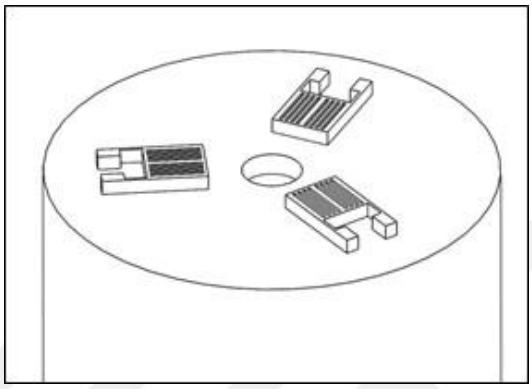

Figure 3.10 Schematic view of hole drilling method (Özaydın et al., 2025)

Rosette types may vary depending on their intended application. According to the relevant standard, three different rosette configurations are defined, as illustrated in Figure 3.11 (ASTM, 2020).

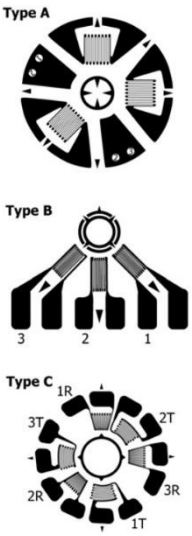

Figure 3.11 Hole drilling rosettes (ASTM, 2020)

Type A rosette strain gauges are generally preferred for flat, unobstructed surfaces, as the symmetric placement of the gauges around the drilled hole enables general-purpose measurements. In contrast, the Type B rosette features a specialized design in which all strain gauges are positioned on one side of the rosette, allowing measurements to be performed in regions close to edges, obstacles, or geometric discontinuities (ASTM, 2020).

Type B rosette is particularly suitable for measurements on contoured surfaces such as wheel rims, where edges, protrusions, and geometric discontinuities are present, due to the placement of all strain gauges on one side of the rosette. This configuration allows the rosette center to be positioned closer to obstacles, thereby increasing the applicability of the measurement and providing a significant advantage in regions where the standard Type A rosette cannot be used. For both rosette types, residual stresses are evaluated using the same linear elasticity–based calculation methods.

Type C rosette is used in applications requiring higher strain sensitivity and improved thermal stability, as pairs of oppositely positioned strain gauges are connected in a half-bridge configuration (ASTM, 2020).

For elastic properties, Equation (3.1), which is based on the stress–strain relationship, is employed. The magnitude and orientation of the principal residual stresses under plane stress conditions are determined using Equation (3.2). The strain release coefficients A and B are among the most critical factors affecting the accuracy of the method and can be calculated directly using Kirsch's theory for the full-hole drilling approach (Guo et al., 2021). The strain release coefficients A and B are given in Equation (3.3), where ν, a, and r indicate the Poisson's ratio, the radius of the drilled hole, and the distance between the strain gauge and the center of the hole, respectively (X. Li et al., 2024).

$$\varepsilon = \mathrm{A}(\sigma 1 + \sigma 2) + \mathrm{B}(\sigma 1 - \sigma 2)\cos 2\theta \tag{3.1}$$

$$\left.\begin{aligned} \sigma_{1,2} &= \frac{1}{4A}(\varepsilon_0 + \varepsilon_{90}) \pm \frac{\sqrt{2}}{4B}\sqrt{(\varepsilon_0 - \varepsilon_{135})^2 + (\varepsilon_{90} - \varepsilon_{135})^2} \\ \tan 2\theta &= \frac{(\varepsilon_0 + \varepsilon_{90} - 2\varepsilon_{135})}{(\varepsilon_0 - \varepsilon_{90})} \end{aligned}\right\} \tag{3.2}$$

$$A = -\frac{(1+\nu)}{2} \times \frac{a^2}{r^2}$$
$$B = \frac{1}{2}\ [3(1+\nu)] \times \frac{a^4}{r^4} - \frac{4a^2}{r^2} \qquad (3.3)$$

In Equations (3.1) and (3.2), ε, ε_0, ε_{90}, and ε_{135} represent the radial strains; σ_1 and σ_2 indicate the principal stresses; θ is the angle between the 0° strain gauge and the direction of the first principal stress; and E represents the elastic modulus (Young's modulus) (Guo et al., 2021; X. Li et al., 2024).

Although this approach is widely adopted in literature as a theoretical framework, it relies on analytical coefficients and is therefore more suitable for idealized and theoretical conditions. In contrast, the standardized method ASTM E837–20: Standard Test Method for Determining Residual Stresses by the Hole-Drilling Strain-Gage Method (ASTM, 2020), which has been experimentally validated, is defined using FEM-based calibration coefficients specific to the rosette type and hole geometry. Since it is incremental and experimentally verified, this standard is more commonly preferred in experimental studies. In the theoretical approach, the stress–strain relationship given in Equation (3.1) is expressed in the ASTM E837–20 standard by Equation (3.4).

$$\varepsilon = \frac{1+\nu}{E}\ \bar{a}\ \frac{\sigma_x+\sigma_y}{2} + \frac{1}{E}\bar{b}\ \frac{\sigma_x-\sigma_y}{2}\cos 2\,\Theta\ + \frac{1}{E}\bar{b}\ \tau_{xy}\sin 2\theta \qquad (3.4)$$

As can be seen from the equation, the constant coefficients A and B used in the theoretical approach are replaced by the coefficients $\bar{a}$ and $\bar{b}$ in the ASTM E837–20 standard. This is because, in ASTM E837–20, the coefficients are calculated as functions of the hole diameter, hole depth, strain-gage rosette geometry, and specimen thickness. These parameters are not considered in the theoretical formulation given in Equation (3.1). Finally, the depth effect, which cannot be considered within the scope of the theoretical approach in Equation (3.1), becomes explicit and quantifiable through the formulation defined in ASTM E837–20, as expressed in Equation (3.5).

$$\varepsilon_j = \frac{1+\nu}{E} \sum_{k=1}^{j} \bar{a}_{jk} \left(\frac{\sigma_x+\sigma_y}{2}\right)_k + \frac{1}{E} \sum_{k=1}^{j} \bar{b}_{jk} \left(\frac{\sigma_x-\sigma_y}{2}\right)_k \cos 2\,\Theta \; + \frac{1}{E} \sum_{k=1}^{j} \bar{b}_{jk} \left(\tau_{xy}\right)_k \sin 2\theta \qquad (3.5)$$

3.2.3.1.2 Ring-Core Method

The ring-core method is fundamentally derived from the hole-drilling method; however, instead of drilling a hole at the center of the strain-gage rosette as in the hole-drilling technique, material is removed in an annular (ring-shaped) region surrounding the strain gages (Figures 3.12 and 3.13). Residual stress measurement is carried out based on the principle of measuring the deformation that occurs during this material removal process.

The primary advantage of the method is its capability to detect relatively large deformations, which enables the measurement of high residual stress levels within the structure. Its main disadvantages, on the other hand, include the relatively bigger damage introduced to the component, as well as practical challenges related to application and strain-gage wiring.

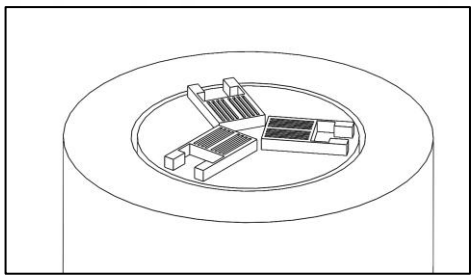

Figure 3.12 Schematic view of the ring-core method (Özaydın et al., 2025)

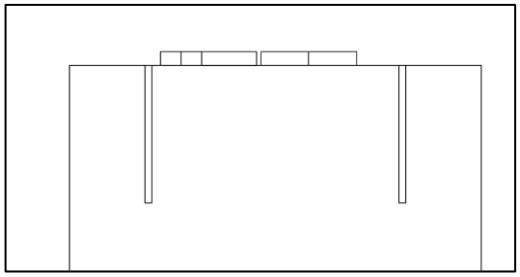

Figure 3.13 Schematic cross-section of the ring-core method (Özaydın et al., 2025)

The measurement approach used in the ring-core method, like the hole-drilling method, is based on the principle of releasing the residual stresses present in the material through controlled material removal. During the machining process, the strain variations that occur are recorded in a computer-assisted manner as a function of the drilling depth. Using these measured strain data, the residual stress distributions within the material are subsequently calculated.

3.2.3.1.3 Deep Hole Drilling Method

The deep hole drilling method is considered an intermediate technique between the conventional hole-drilling method and the ring-core method. In this approach, a hole is first drilled through the workpiece, and the initial diameter of the hole is measured with high precision. Subsequently, following a procedure like the ring-core method, the material surrounding the hole is removed in an annular manner. After the machining process is completed, the hole diameter is measured again, and the residual stress values are calculated based on the difference between the initial and final diameters.

The main advantage of this method is its capability to enable residual stress measurements in dimensionally large components. Its primary disadvantage, however, lies in the requirement for specialized cutting tools and dedicated measurement fixtures necessary for deep hole drilling.

3.2.3.1.4 Contour Method

The contour method was first proposed by Prime (Prime, 2001). The method was developed to enable the two-dimensional evaluation of residual stresses. By allowing visualization of residual stresses over the entire cut section, it provides holistic and spatially resolved results across the sectioned plane.

This technique is based on Bueckner's superposition principle, which can be fundamentally stated as follows: "The forces required to close the crack surfaces are equivalent to the stress distribution that would exist in an uncracked body subjected to the same loading conditions" (Hacini et al., 2009).

The measurement procedure consists of several sequential steps: sectioning of the specimen, acquisition of the surface profile, data collection, and determination of the residual stress distribution. To obtain an accurate and reliable surface profile, the quality of the cut surface is of critical importance. For this reason, wire electrical discharge machining (wire EDM) is preferred over conventional cutting techniques, as it minimizes additional plastic deformation and thermal effects during sectioning.

In addition to the cutting technique, several other process parameters must be carefully considered, as they can significantly influence the measurement results. These parameters include the material properties, the wire EDM process parameters, and the geometric complexity of the component (Hacini et al., 2009; Schajer, 2010).

3.2.3.1.5 Sectioning Method

This method is classified under different names in the literature, such as sectioning, slitting, or slicing, depending on the source (Ekmekçi, 2004; Rossini et al., 2012; Tabatabaeian et al., 2022). The sectioning technique is a destructive residual stress measurement method based on measuring the deformation that occurs because of the release of residual stresses during the removal of a defined mass or volume of material from the component under investigation (Figures 3.14 and 3.15).

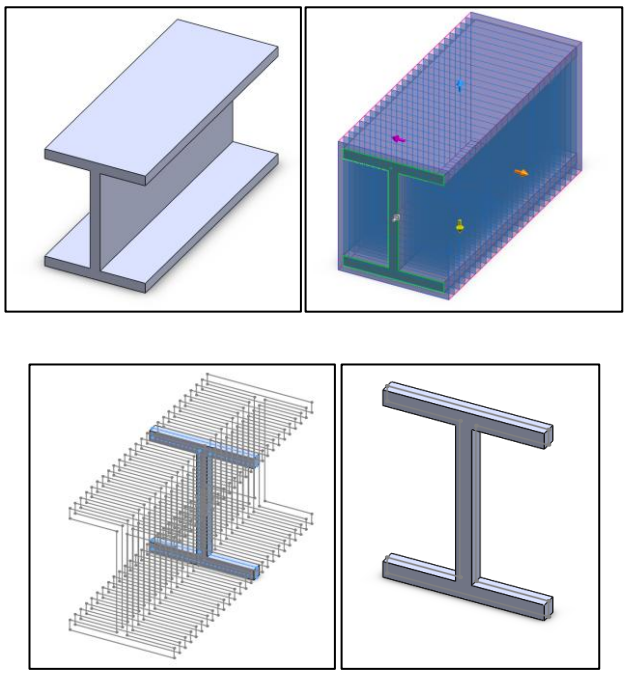

Figure 3.14 Schematic view of an I-Profile in the sectioning method (Özaydın et al., 2025)

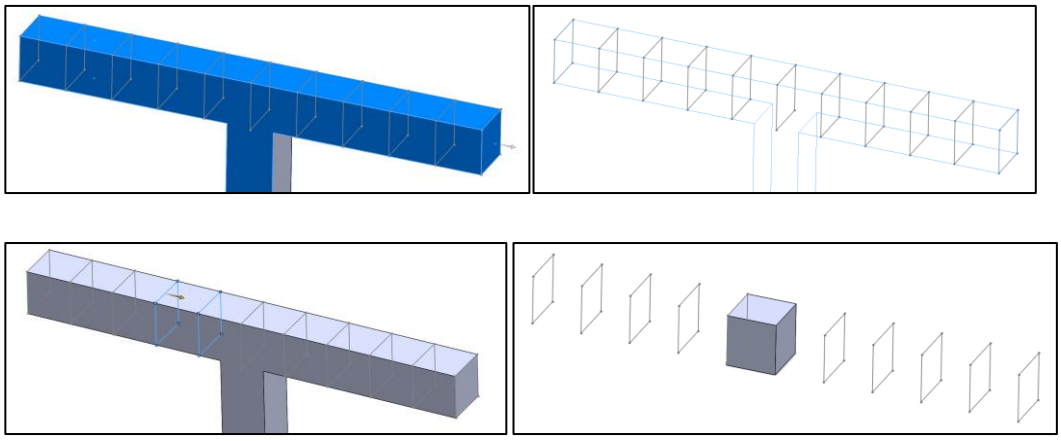

Figure 3.15 Detailed schematic view of an I-Profile in the sectioning method (Özaydın et al., 2025)

3.2.3.2 Non-Destructive Measurement Techniques

Non-destructive methods are based on the measurement of elastic deformations. The defining characteristic of these techniques is that the measurement process is carried out without causing any damage to the material.

Although non-destructive methods generally provide more accurate results compared to destructive techniques, they are associated with significantly higher costs (Tabatabaeian et al., 2022). Consequently, their applicability in industrial studies—where cost effectiveness is a critical requirement—can be limited.

Among non-destructive residual stress measurement techniques, X-ray diffraction (XRD), ultrasonic methods, and neutron diffraction are the most used approaches.

3.2.3.2.1 XRD: X-Ray Diffraction Method

One of the most widely used methods for the determination of residual stresses is the X-ray diffraction (XRD) technique. X-ray diffraction is a non-destructive measurement method that is primarily employed for the evaluation of residual stresses at or near the surface of materials.

This method is based on the changes in the interplanar spacing of atomic planes caused by elastic deformations arising from applied stresses or existing residual stresses in the material. Using the X-ray diffraction technique, the spacing between

atomic planes is measured, and residual stresses are subsequently determined by calculating the elastic strain values derived from these variations in interplanar spacing (Akdeniz, 2012).

The X-ray spectrometer is schematically illustrated in Figure 3.16. X-rays emitted from the tube (T) are directed toward the crystal (C), which can be rotated about an axis passing through point O, the center of the spectrometer circle, allowing adjustment to any desired angle with respect to the incident beam. The intensity of the diffracted X-rays is measured by the detector (D), which can likewise be rotated about point O and precisely positioned at the required angular location. During the measurement, the crystal is oriented such that the diffraction planes form a specific angle with the incident X-ray beam, and the angular position of the detector is adjusted accordingly. Following this alignment, the intensity of the diffracted beam is recorded, and the corresponding wavelength is calculated using Bragg's law (Equation 3.6) (Cullity & Stock, 2014), (Dieter, 1961).

$$\lambda = 2d \sin\theta \tag{3.6}$$

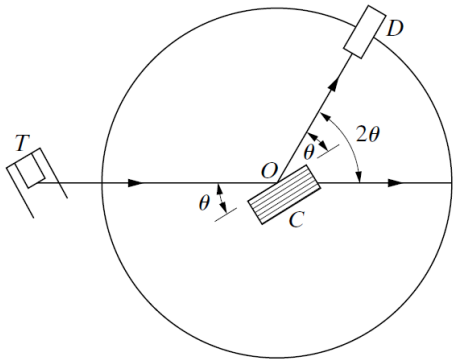

Figure 3.16 The x-ray spectrometer (Cullity & Stock, 2014)

The principal advantage of this method is its ability to measure all types of residual stresses. In contrast, the high cost of the equipment and the limitations on the size of specimens that can be measured are considered their main disadvantages.

3.2.3.2.2 Ultrasonic Method

In ultrasonic methods, variations in ultrasonic wave velocities caused by the stress state within a solid material are measured, and these measurements are used to calculate residual stress values.

A material exhibits different ultrasonic wave velocities in the presence of residual stresses compared to a stress-free state. If the material maintains elastic behavior, the ultrasonic wave velocity varies as a function of the residual stress state within the material (Dege, 2013).

Residual stresses present within a material hinder the propagation of acoustic waves, leading to a reduction in wave velocities. Accordingly, the round-trip travel times of ultrasonic waves that propagate through the material and are reflected from the back surface differ from those observed in a stress-free material. Since these differences are in the order of nanoseconds, the detection of such variations requires measurement systems with extremely high sensitivity (Akdeniz, 2012). According to the literature, ultrasonic methods are predominantly applied to welded components and are widely used for the evaluation of residual stresses generated as a result of welding processes.

3.2.3.2.3 Neutron Diffraction Method

The neutron diffraction method operates on a principle similar to that of X-ray diffraction, enabling the determination of residual stresses by measuring changes in the interatomic lattice spacing within the crystalline structure of a material. The primary advantage of this technique lies in the use of neutrons, which possess significantly greater penetration depth compared to X-rays, thereby allowing residual stress measurements to be performed deep within the material (Akdeniz, 2012). As with other non-destructive techniques, the major limitations of neutron diffraction are its high cost and the requirement for specialized, large-scale experimental facilities.

3.2.3.3 Analytical Techniques

In residual stress analysis, destructive and non-destructive experimental techniques have been defined as the primary approaches. However, in industrial applications, the

increasing costs associated with measurement equipment, setup requirements, and testing time have led to a growing reliance on analytical methods and finite element (FE) modeling. The main advantages of these approaches are their relatively short implementation time and the elimination of the need for specialized measurement equipment and installation costs. Nevertheless, their most significant limitation lies in the difficulty of accurately modeling all aspects of real operating and processing conditions. Methods that involve residual stress evaluation through analytical formulations and finite element models are therefore classified under analytical techniques.

As in many manufacturing processes, casting simulations are also performed in the low-pressure die casting (LPDC) process prior to experimental trials in order to identify potential casting defects and to evaluate characteristics such as castability and mold filling behavior. This step, which can be considered part of product validation activities, involves analyzing the real experimental process environment within a simulation framework using various commercial software packages. Examples of such software include those based on the Finite Difference Method (e.g., Magmasoft, FLOW-3D Cast, SolidCast), the Finite Volume Method (e.g., CastCAE, Noca-Solid&Flow), the Finite Element Method (e.g., CapCast, ProCAST), and the Vector Element Method (e.g., AutoCAST) (Khan & Sheikh, 2018).

Although not available in all commercial software packages, some casting simulation tools offer additional modules capable of calculating residual stresses. Among these, Magmasoft not only enables casting simulations for product validation but also provides the Magmastress module, which allows thermal effects applied to the component to be defined and the resulting residual stresses to be calculated.

In this study, heat treatment simulations were carried out using the Magmasoft software in conjunction with the Magmastress module. During the heat treatment simulation stages, furnace temperatures, holding times, process temperatures, as well as quenching media and their temperatures were defined within the software to replicate the heat treatment conditions. Through these simulations, it was aimed to evaluate the effects of variations in heat treatment parameters on material properties and to analyze the resulting residual stress distributions.

As part of their benchmark analysis, Johnson et al. carried out a simulation investigation in Magmastress using a thermo-elasto-plastic formulation (Johnson et al., 2012).

The mechanical and thermal stresses, ε_{Mech} and ε_{Th}, respectively, add up to the total strain, ε_{Tot}, which is determined by (Equation 3.7):

$$\varepsilon_{\{Tot\}} = \varepsilon_{\{Mech\}} + \varepsilon_{\{Th\}} = \varepsilon_{\{El\}} + \varepsilon_{\{Pl\}} + \varepsilon_{\{Th\}} \tag{3.7}$$

The temperature history is used to calculate thermal strain increments, which are then integrated over time during cooling. The thermal strain (Equation 3.8), which is determined by (Johnson et al., 2012), also considers volumetric expansion and contraction from the phase changes:

$$\varepsilon_{\{Th\}} = \int_{T_1}^{T_2} \alpha(T)dt \tag{3.8}$$

where T and α stand for temperature and thermal expansion coefficient, respectively.

Magmastress uses a well-known elasto-plastic formula that combines‘ law with (Equation 3.9):

$$\sigma_{ij} = \frac{E}{1+\nu}\left\{\varepsilon_{ij} + \frac{\nu}{1-2\nu}\delta_{ij}\varepsilon_{kk}\right\} - \delta_{ij}\frac{E\alpha\Delta T}{1-2\nu} \tag{3.9}$$

where v is the Poisson’s ratio, E is the Young’s modulus, and δ_{ij} is the Kronecker delta (Johnson et al., 2012) provides a conventional formulation with a temperature-dependent yield condition that includes isotropic hardening (Equation 3.10).

$$\varepsilon_{Mech} = \begin{cases} \frac{\sigma}{E} & for\ \sigma < \sigma_y \\ \frac{\sigma_y}{E}\left[\frac{1}{n}\left(\frac{\sigma}{\sigma_y}\right)^n - \frac{1}{n} + 1\right] & for\ \sigma \geq \sigma_y \end{cases} \tag{3.10}$$

where σ_y is the yield stress and n is the hardening parameter (Johnson et al., 2012).

When all these methods are evaluated specifically for the aluminum alloy casting samples and wheels considered in this study, the hole-drilling method was identified as the most appropriate technique. This conclusion is based on its suitability for the material in question, its applicability under industrial conditions, its widespread acceptance and preference in industrial practice, and the availability of well-established, standardized application and calculation procedures. Accordingly, the hole-drilling method was selected for experimental investigations.

Although this technique introduces a limited level of damage to the component (approximately 1.5 mm in hole diameter and up to about 2.0 mm in depth), its high accuracy, reliability, standardized testing procedures, and relative ease of implementation played a decisive role in its selection for this study.

In addition, it was considered that performing an analytical evaluation of residual stresses for the aluminum alloy wheel would provide complementary insight by enabling the identification of critical residual stress regions and a clearer understanding of their location distribution within the component. Accordingly, analytical analyses were carried out using the Magmastress module of the Magmasoft software. On this basis, experimental procedures were designed and planned to ensure a holistic and integrated approach to the study.

Due to both the very high investment costs and the practical difficulties associated with their implementation in industrial environments, non-destructive methods were not preferred in this study.

Instead, the hole-drilling method selected for experimental application, together with the analytical techniques employed, is described in detail in the following “Experimental Study” section.

CHAPTER FOUR
EXPERIMENTAL STUDY

In this section of the study, the experimental investigations corresponding to the material and methodological approaches presented in the previous chapter are addressed. The Experimental Study section comprises the experimental applications carried out under the headings of material and casting, heat treatment, and residual stress, respectively.

Under the “Material and Casting” heading, the chemical composition of the AlSi11Mg alloy used in this study is first determined, and the suitability of this composition is evaluated. Subsequently, experimental steps related to the production of cast specimens and sample wheels manufactured using this aluminum alloy are described. Following this stage, the microstructural and macrostructural analysis procedures applied to the aluminum alloy wheels are presented, and finally, standard tensile and hardness tests are discussed in detail.

Under the “Heat Treatment Applications” heading, the different heat treatment trials applied to the cast aluminum alloy wheels are presented in tabulated form. The experimental procedures associated with these trials are described, and the expected microstructural and mechanical changes resulting from each treatment condition are explained in detail.

Under the “Residual Stress Measurement” heading, the experimental studies for the analytically-based method and the destructive hole drilling technique—selected according to the justifications provided in the previous section—are presented. Within this scope, the preparation steps and software details used for the analytical approach are described, while for the hole drilling method, the procedures for sample preparation, strain gauge application, drilling operation, and data acquisition are systematically explained.

4.1 Material and Casting

As detailed and justified under “3.1 Materials” in Chapter 3, the AlSi11Mg alloy was selected for this study. The alloy used in the experimental work, including all aluminum cast sample parts and the trial cast sample wheels, was supplied by “Döktaş Dökümcülük Tic. ve San. A.Ş.” Although this same alloy is used in serial production, it was also employed for the trial casting in this study, with repeated quality and measurement tests applied to ensure consistency.

For metal preparation, molten metal taken from the main furnace in the foundry was first transferred to a holding furnace. Grain refinement (using $AlTi_5B$ at 100 ppm) and modification (using $AlSr_{15}$ at 250 ppm) were applied, after which the melt was directly subjected to degassing without additional alloying. During the degassing step, a program identical to the serial production process was followed. To remove hydrogen and oxides efficiently, nitrogen gas was injected through a rotor into the molten metal, providing a cost-effective solution. Following degassing, the dross was removed, and the “cleaned” melt was sampled for chemical analysis.

Chemical composition was determined using Optical Emission Spectroscopy (OES), which generates a localized arc on the sample surface to induce rapid and precise combustion. To ensure reliability, at least three arc burnings were performed for each sample. In this study, chemical analyses were conducted in accordance with ASTM standards E415, E1086, E1251, and E2994 using an ARL 8820 spectrometer at the laboratories of “Döktaş Dökümcülük Tic. ve San. A.Ş.” The resulting data will be presented and discussed in the “Results and Discussion” section of this work.

Prior to the wheel casting process, gravity casting was carried out using sample molds to produce trial specimens. These samples were cast in aluminum alloy to serve as preliminary test pieces before the actual production of the wheels (Figure 4.1).



Figure 4.1 Gravity-cast preliminary specimens (Personal archive, 2026)

The “cleaned” and chemically analyzed molten metal was rapidly transferred to the low-pressure die casting (LPDC) machine to minimize potential oxidation risks. Prior to this transfer, the mold specifically designed for the corresponding wheel model was mounted on the LPDC machine and held ready for casting. The mold preparation, including assembly of its various components and attachment to the machine, was carried out following the same procedures used in series production, ensuring that all production parameters outside the scope of the study remained consistent.

The molten metal brought to the holding furnace of the LPDC machine was transferred with minimal flow turbulence to avoid bifilm formation or oxidation issues. The transferred metal was held at 720 ± 20 °C before proceeding to the casting step. Casting began when pressure applied to the holding furnace caused the molten metal to rise through the riser tube. The process then involved filling the mold cavity, initiating solidification, completing solidification, and executing the drop step. In general, the process includes pressurization, holding under pressure, and depressurization stages, which may vary depending on the wheel model, size, and cooling channel design in different manufacturing setups.

For example, in the LPDC machine, metal is pressurized between 0.8 and 1 bar and the total casting process can last 300–350 seconds. The initial castings in a mold are deliberately performed as trial wheels to bring the mold up to the desired casting temperature (~400 °C) and allow it to reach thermal steady state. Once the mold is properly conditioned, the actual casting is carried out (Figure 4.2).



Figure 4.2 Low-pressure as-cast wheel specimen - Option #1 (Personal archive, 2026)

The properly cast as-cast wheels were removed from the machine after the casting process and proceeded to the marking, coding, and burr-removal stage. At this point, the freshly cast wheels were still at a high temperature (~300–400 °C), making direct handling unsafe. To enable the operators to perform the necessary operations, the wheels were first dipped into a water bath to reduce their temperature. Once cooled, the required marking, coding, and burr-removal steps were carried out.

Following this stage, the wheels underwent 100% X-ray inspection, and those meeting quality requirements had the hub filters removed via hub drilling before proceeding to the heat treatment process.

At this stage, microstructural analyses can be performed on the wheels in their as-cast condition. Essentially, the same experimental procedure applies to the wheels that will undergo micro- and macrostructural analyses after the subsequent heat treatment, ensuring consistency across all samples in the study.

Samples for microstructural analysis were prepared following standard metallographic procedures. Specifically, the samples were ground using SiC abrasive papers of progressively finer grit sizes, then polished with felt cloth and polishing paste. After polishing, the surfaces were cleaned with alcohol and deionized water and subsequently etched using a 0.5% hydrofluoric acid (HF) solution. Following etching, microstructural examinations were performed using an optical microscope.

Macrostructural analyses were conducted on the wheel cross-sections after etching. The resulting microstructures were observed using the optical microscopes available at the “Döktaş Dökümcülük Tic. ve San. A.Ş.” laboratories, while the macrostructures were classified by comparison with structures defined in the American Foundrymen’s Society (AFS) ASTM E112 procedure.

Similar to the preparation and examination procedures for chemical analysis, microstructure, and macrostructure, the tensile and hardness tests were also conducted at the “Döktaş Dökümcülük Tic. ve San. A.Ş.” laboratories.

Tensile tests were performed on specimens prepared in accordance with the DIN 50125 standard, using a Shimadzu AG-I 100 kN tensile testing machine, following the EN ISO 6892-1:2016 standard. The tests provided measurements of yield strength [MPa], ultimate tensile strength [MPa], and elongation [%].

Hardness measurements were carried out as Brinell hardness values using a QNESS CS EVO 250 Brinell hardness tester, in accordance with ASTM E10. Hardness values were measured at the defined inner flange, outer flange, and spoke regions of the specimens (Figure 4.3) and are summarized in tables presented in the “Results and Discussion” section.

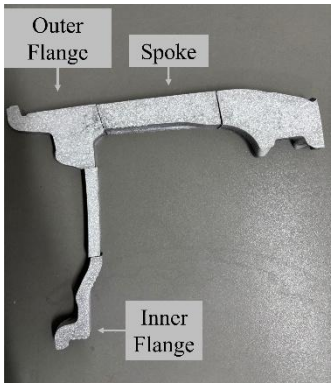

Figure 4.3 Inner flange, outer flange and spoke on cross-section of wheel

4.2 Heat Treatment Applications

Heat treatment applications initially began with cooling experiments performed on samples obtained via gravity casting prior to wheel production. The same alloyed metal was used for all the sample castings, while some samples were allowed to cool naturally in air and others were quenched in water (Figure 4.4).

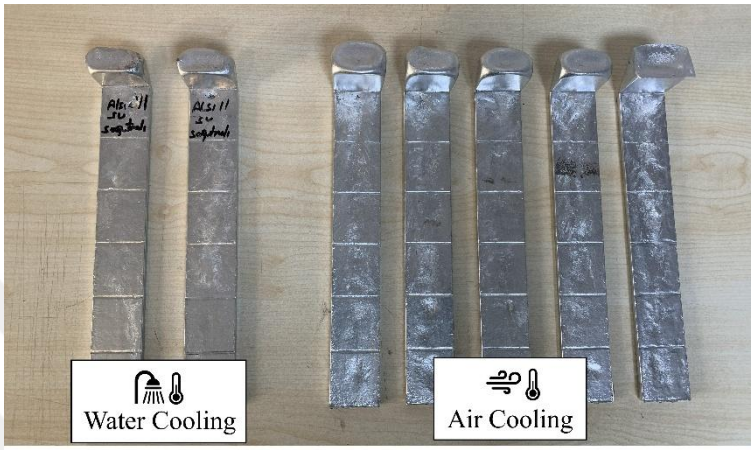

Figure 4.4 Gravity-cast preliminary specimens with different cooling conditions (Personal archive, 2026)

The experimental procedures of the study continued with the wheels that passed 100% X-ray inspection being transferred to the heat treatment facility. Upon arrival at the facility, the wheel batch was divided into three main groups to evaluate the effects of different heat treatment conditions.

The first group consisted of wheels labeled as as-cast (Figure 4.2, Option #1), which were not subjected to any heat treatment at the facility. These wheels were only exposed to the mandatory handling step, which involved immersion in a water bath for safe manipulation after casting.

The second main group consisted of wheels that underwent the full T6 heat treatment (solution treatment, water quenching, and artificial aging) under series production conditions (Figure 4.5). Within this group, wheels were subjected to different aging durations—Option #2: 150 min, Option #3: 120 min, and Option #4: 90 min—to investigate the effect of aging time on mechanical properties. In this group,

the high temperature difference between the solution treatment and water quenching step is also expected to increase the risk of residual stress formation.



Figure 4.5 Low-pressure T6 heat treated wheel specimens - Option #2, #3, #4 (Personal archive, 2026)

The third main group consisted of wheels subjected only to artificial aging (Figure 4.6, Option #5). Since this process is similar to a stress-relief annealing, this group was examined to evaluate whether artificial aging alone has a significant effect on the reduction of residual stresses.



Figure 4.6 Low-pressure artificial aged wheel - Option #5 (Personal archive, 2026)

Table 4.1 presents the detailed heat treatment procedures applied to the wheels. For the trial-cast wheels, a solution treatment was performed at 535 ± 5 °C for 200 minutes.

The subsequent quenching step was carried out in moderately stirred water at 80 ± 5 °C for 70 seconds. Finally, an artificial aging treatment was applied at 155 ± 5 °C for 150 minutes. In addition to this standard heat treatment sequence, alternative heat treatment routes specific to this study were also implemented to evaluate their effects on mechanical properties and hardness values.

Table 4.1 Heat treatment application

	Solution Treatment		Quenching		Artificial Aging	
	Temperature (°C)	Duration (min)	Temperature (°C)	Duration (s)	Temperature (°C)	Duration (min)
Option #1	N/A	N/A	N/A	N/A	N/A	N/A
Option #2	535±5	200	80±5	70	155±5	150
Option #3	535±5	200	80±5	70	155±5	120
Option #4	535±5	200	80±5	70	155±5	90
Option #5	N/A	N/A	N/A	N/A	155±5	150

4.3 Residual Stress Calculation and Measurement

At the end of the previous chapter, the residual stress measurement methods selected for this study were explained in detail. For the specific case of aluminum alloy cast specimens and wheels considered in this work, the hole-drilling method was identified as the most suitable destructive technique, particularly in view of its applicability to industrial practice. Owing to its reliance on standardized testing and calculation procedures, the hole-drilling method was therefore considered appropriate and was selected as the experimental residual stress measurement technique in this study.

Before the experimental procedures were carried out, it was considered necessary to perform residual stress calculations and analyses using analytical methods, which have become increasingly popular in industrial applications due to their cost-effectiveness, as they do not require any additional equipment or experimental setup.

The analytical calculations and analyses conducted in this study were intended to both predict regions with a high risk of residual stress formation in aluminum alloy wheels and estimate the potential magnitudes of residual stresses that may develop in these components.

Once again, due to the very high investment costs and the practical difficulties associated with their implementation under industrial conditions, non-destructive methods were not preferred in the experimental phase of this study.

4.3.1 Residual Stress Calculation: Analytical Technique and Simulations

Initially, the Low Pressure Die Casting (LPDC) process was defined within the simulation software (Magmasoft) utilized in this study. The following modules consist of the sequential structure of Magmasoft's workflow: Project, Geometry, Mesh, Definition, Optimization, Simulation, Assessment, and Result (Magmasoft, 2015).

After creating the "Project" in the software, the "Geometry" stage starts, the mold and wheel configurations utilized in the study are defined based on the corresponding CAD models. Subsequently, material definitions for both the wheel and the individual mold components are specified using the software's internal material library. In addition, movable elements of the mold, including the upper die and side cores, are identified and configured within this step. Following this step, a suitable computational mesh is created, accompanied by a systematic evaluation of mesh quality. To obtain accurate simulation results, particular focus is given to regulating element size, distribution, and local refinement inside thin-walled regions. After the meshing procedure is completed, the workflow advances to the "Definition" stage. In this phase, the casting alloy, bottom die, upper die, and side core elements, as well as the runner system, cooling channels, and air gaps, are specified based on information obtained from the software's material database. Initial temperature conditions are then assigned to each component.

To enable an accurate representation of thermal interactions, appropriate heat transfer coefficients (HTC) are introduced at this stage. These coefficients are defined for all interfaces where thermal contact occurs between mold components. Finally, the process conditions are established, and the mold filling, pressure holding,

solidification, and cooling stages are comprehensively defined and implemented within the simulation environment (Figure 4.7) (Özaydın, 2019).

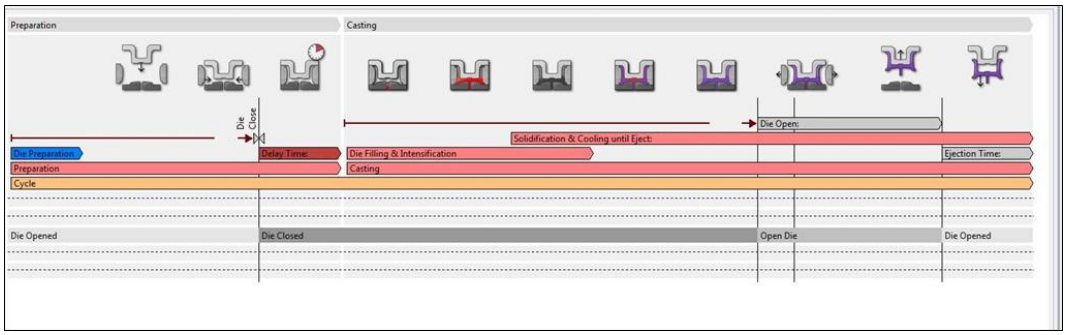

Figure 4.7 Casting simulation process steps (Özaydın, 2019)

After all necessary definitions have been completed, the workflow proceeds to the simulation stage, during which the analysis is performed to obtain results for subsequent evaluation. In this manner, the entire casting process of the wheel is comprehensively modeled using the Magmasoft Wheel module.

After the casting simulation is finished, the heat treatment process is subsequently modeled to evaluate the resulting residual stress state. At this stage, the Magmastress module, which operates as a dedicated extension within the same simulation environment, is run. The primary function of this module is to calculate stress evolution following casting and to predict the distribution of residual stresses with high accuracy.

In parallel with the numerical approach, the experimental production sequence involves several post-casting “handling” operations. After completion of the wheel casting cycle, the component is removed from the die casting machine and transferred to a conveyor system for X-ray inspection. During the handling phase, identification markings are applied and burrs / leftovers originating from mold parting lines are manually removed by the operator. To ensure safe handling conditions, the wheel is first subjected to partial cooling. This is accomplished by quickly lowering the wheels’ temperature after casting by putting it in cooling bath that is between 70 and 80 °C for 20 seconds. Following removal from the cooling bath, preliminary marking and rough flash removal are completed, after which the wheel is placed on the conveyor belt for

transport to X-ray inspection. This handling sequence is applied to all produced wheels, irrespective of whether a subsequent heat treatment is performed. Consequently, the described handling and cooling steps are incorporated into the simulation framework prior to the heat treatment analysis to achieve a realistic representation of the industrial process and to enhance the accuracy of the predicted stress results.

After completion of the handling-related procedures, the heat treatment stages applied to the wheel component were also defined within the same simulation module. Within the Magmastress module, the analysis workflow follows a structured sequence consisting of geometry definition, material assignment, mesh generation, solidification modeling, boundary condition specification, stress analysis, results evaluation, and optimization, in accordance with the methodology described previously.

In the present study, once the geometric model was established, material properties for the casting alloy, runner system, riser, filter, and permanent mold components—including the upper, side, and bottom dies—were selected from the software's integrated material database. The computational mesh was generated to ensure a minimum of three elements across the narrowest sections, and the corresponding boundary conditions were defined accordingly.

Unlike the other simulation modules, the stress analysis stage (Figure 4.8) incorporates an expanded "Result Definitions" section that enables the calculation of stress-related outputs. As a result, simulation results corresponding to the "Preparation", "Die Filling", "Solidification", and "Heat Treatment" stages were obtained and evaluated.

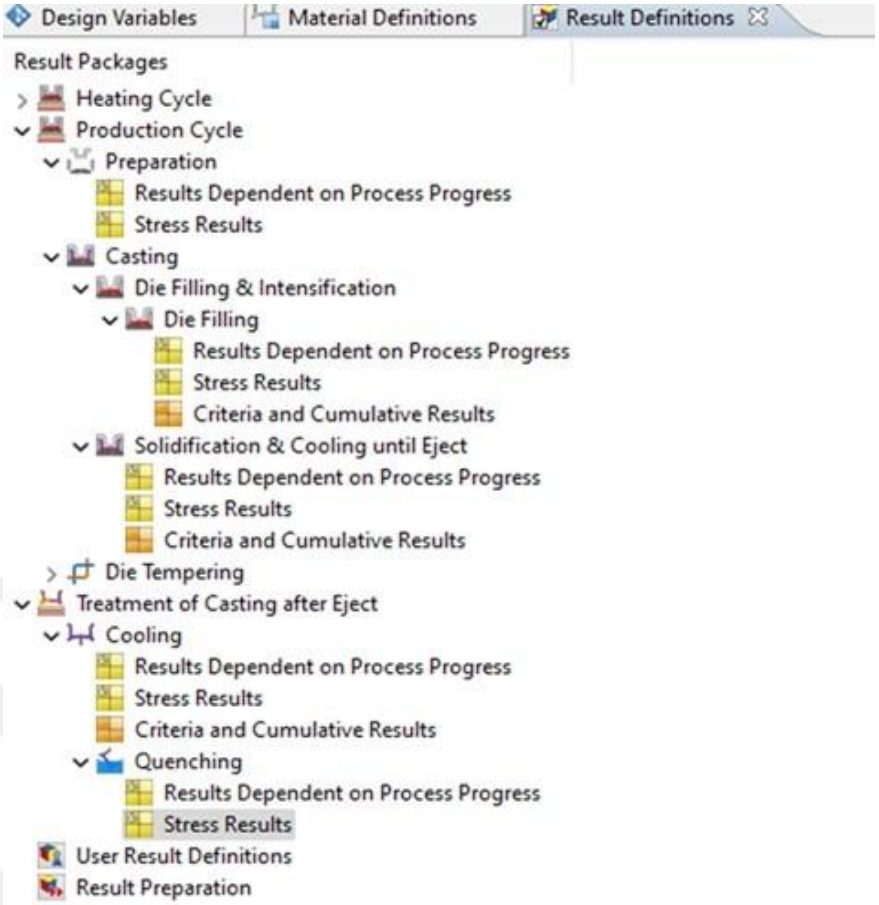

Figure 4.8 Results definition in Magmasoft software - Magmastress module (Özaydın, 2019)

During the definition phase, several alternative simulation configurations were established to address specific objectives. The corresponding results obtained from these configurations are presented and discussed in the “Results and Discussion” section. In total, five unique heat treatment scenarios (Option #1 - #5) were defined and implemented prior to the heat treatment simulations.

The first option (Option #1) represents the conventional as-cast condition commonly applied to AlSi11Mg alloy wheels in industrial practice. In this scenario, only the handling-related process definitions were considered, and no heat treatment stages were introduced. Consequently, comparatively lower mechanical performance is expected when compared with the remaining configurations.

In the second (Option #2), third (Option #3), and fourth (Option #4) options, a T6 heat treatment was applied to the AlSi11Mg alloy, in accordance with procedures typically employed for aluminum alloy components. The simulation steps were defined to closely replicate the process parameters used by the industrial partner, consisting of solution treatment at 535 ± 5 °C for 200 minutes, water quenching at 80 ± 5 °C for 70 seconds, and artificial aging at 155 ± 5 °C for 150 minutes. Although higher levels of residual stress are expected under these conditions, the resulting mechanical properties are also anticipated to be significantly enhanced. The primary difference among these three options lies in the artificial aging durations. While all other processing conditions were kept the same for Options #2, #3, and #4, the artificial aging times were set to 150 minutes, 120 minutes, and 90 minutes, respectively, as summarized in Table 4.1.

The fifth option (Option #5) was developed to address the generation of residual stresses associated with the large temperature gradients induced during water quenching in the T6 process, as frequently reported in the literature. To reduce this effect, a treatment similar stress-relief annealing was implemented. This approach is expected to result in lower residual stress levels, although the corresponding mechanical properties are not expected to reach those achieved under the T6 heat treatment condition.

4.3.2 Residual Stress Measurement: Hole Drilling Method on Aluminum Cast Parts

For the measurement of residual stresses in aluminum alloy cast components, the hole-drilling method was selected as the destructive experimental technique. In this method, a blind or through-hole is drilled at the region of interest on the component, and the changes in strain measured by strain gauges before and after drilling are recorded. The measured strain variations are then converted into stress values using established analytical relationships. The fundamental principle of the method is based on quantifying the difference between the state of stress before and after material removal, from which the residual stress values are calculated.

These experimental studies were carried out on aluminum alloy components cast specifically for this work. The experimental plan comprised aluminum cast parts that

can be fundamentally classified into two groups: gravity-cast preliminary specimens and Low-pressure cast wheel specimens.

The first group consisted of gravity-cast preliminary specimens with a relatively simple geometry in the form of a rectangular prism, designed for preliminary experimental investigations (Figures 4.1 and 4.4). The second group included low-pressure cast wheel specimens, representing product-level components manufactured under industrial conditions for the main automotive and aftermarket wheel industry (Figures 4.2, 4.5, and 4.6).

For cast wheel specimens, the hole-drilling equipment used for residual stress measurements, as well as the data acquisition system responsible for collecting, processing, and monitoring the measurement data, are described in detail in the following section.

4.3.2.1 Gravity-Cast Preliminary Specimens

The gravity-cast preliminary specimens shown in Figures 4.1 and 4.4 were produced from the AlSi11Mg alloy—selected for this study—using the gravity casting method. These specimens were manufactured to evaluate the applicability of the hole-drilling method, to determine appropriate hole-drilling parameters, and to verify the reliability and quality of the data obtained from the laboratory-scale measurement setup.

Mantle and Aspinwall conducted a comprehensive investigation into the influence of various machining parameters on residual stress formation during machining. Their study demonstrated that cutting speed, feed rate, depth of cut, workpiece orientation, and milling direction have a significant influence on the resulting residual stress profiles (Mantle & Aspinwall, 2001).

Based on these findings, an experimental set-up was designed for the gravity-cast preliminary specimens to determine the most suitable hole-drilling parameters, with a specific focus on cutting speed and feed rate. All other parameters—such as hole diameter, depth of cut, workpiece orientation, and milling direction—were kept

constant to understand the effects of cutting speed and feed rate on the drilling process and the resulting strain measurements.

In this experimental set, a uniaxial single-direction strain gauge was employed to observe the strain relaxation on the specimens resulting from variations in machining parameters (Table 4.2, Figure 4.9). Through this approach, the influence of the selected processing parameters on the measured strain response was evaluated, with the aim of identifying the most suitable machining conditions for the hole-drilling procedure. As mentioned before 1.5 mm in hole diameter and up to 2.0 mm in depth is applied.

Furthermore, using the machining parameters identified as suitable, three holes were drilled at different distances from the uniaxial strain gauge, and a comparative set of measurements was obtained on the same specimen.

Table 4.2 Machining parameters and experimental set ups for gravity-cast preliminary specimens

Gravity Specimens No	Machining Plan No	Cutting Speed [rpm]	Feed Rate [mm/min]	Cooling Condition	Strain Gauge Type
Primary experimental set-up					
#1	#1	18000	0.2	Air	Uniaxial
#2	#2	18000	0.3	Air	Uniaxial
#3	#3	12000	0.2	Air	Uniaxial
#4	#4	12000	0.3	Air	Uniaxial
Secondary experimental set-up					
#5	#1	18000	0.2	Water	Uniaxial
#6				Air	Rosette
#7				Water	Rosette

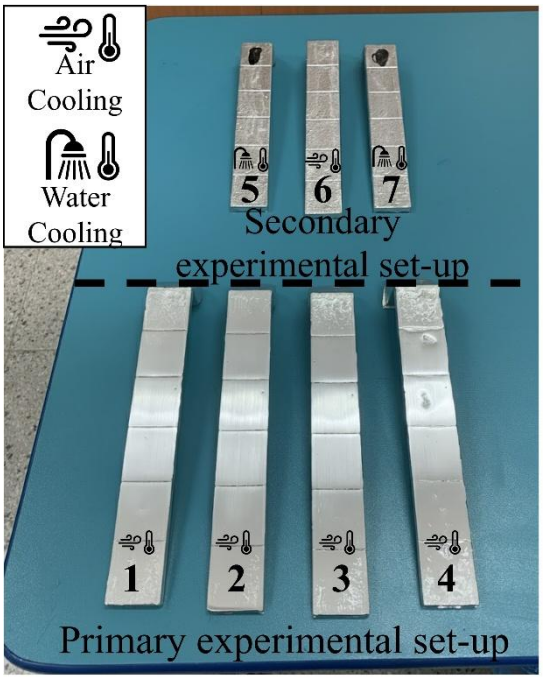

Figure 4.9 Gravity-cast preliminary specimens (Personal archive, 2026)

Prior to the experimental investigation of the appropriate machining parameters, the regions intended for strain gauge application were prepared accordingly. This surface preparation process typically began with achieving suitable surface roughness. The surface roughness was adjusted through successive grinding using 80, 120, 240, and finally 400 grit abrasive papers (Figures 4.10 and 4.11). According to the application note titled “Surface Preparation for Strain Gage Bonding” published by Vishay, one of the leading companies in the field, a final surface finish corresponding to 400 grit is considered appropriate for reliable strain gauge bonding (Vishay, 2005).

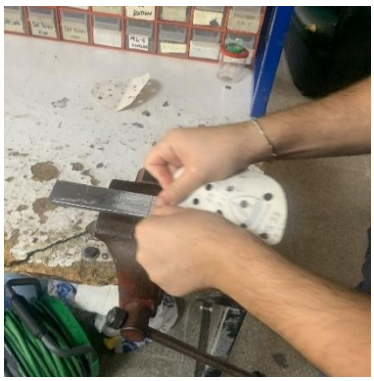

Figure 4.10 Surface preparation (Personal archive, 2026)



Figure 4.11 Surface-prepared (top left) and non–surface-prepared (bottom right) specimen (Personal archive, 2026)

The critical aspect at this stage is to achieve a surface condition that is sufficiently smooth so as not to introduce errors into the strain gauge measurements, while at the same time being adequately rough to ensure proper adhesion of the strain gauge to the surface. Although all preparation steps in this study were carried out under laboratory conditions, it should be noted that the surface was thoroughly cleaned and free from contaminants such as dirt, oil, and grease. This level of surface cleanliness is equally essential and should be controllable and reproducible under industrial application conditions.

Uniaxial strain gauges were applied to the surface-prepared gravity-cast preliminary specimens in accordance with the machining parameters listed in Table 4.2. The application procedure comprised cleaning the specimen surfaces—previously prepared to the appropriate surface roughness—using a solvent-based surface cleaner (Loctite SF 7063), followed by strain gauge bonding after the surface had completely dried, and subsequent wiring of the gauges. The strain gauges used in this study were uniaxial Kyowa KFGS-5-350-C1-11 L2M3R models with a nominal resistance of 350 Ω (Figure 4.12).



Figure 4.12 Uniaxial strain gauges (Personal archive, 2026)

At this stage of the experimental study, the objective was to observe the differences in strain relaxation caused by the material removal performed near uniaxial strain gauges, and thereby to identify the most suitable machining process parameters. In the primary experimental set-up, uniaxial strain gauges were applied to four gravity-cast preliminary specimens (Gravity Specimen #1, #2, #3, and #4). These specimens were then mounted on a laboratory-scale CNC machine (Figure 4.13) located at the ACRL Laboratory of Dokuz Eylül University (Figure 4.14).

The machining system used in this study was a Snapmaker Artisan 3-in-1 device, which integrates multiple functions including 3D printing, laser engraving and cutting, and CNC carving and cutting within a single platform (Figure 4.15). In the present work, the CNC module of the Snapmaker Artisan 3-in-1 system was utilized to perform hole drilling operations, enabling the execution of destructive residual stress measurement experiments on aluminum cast specimens.

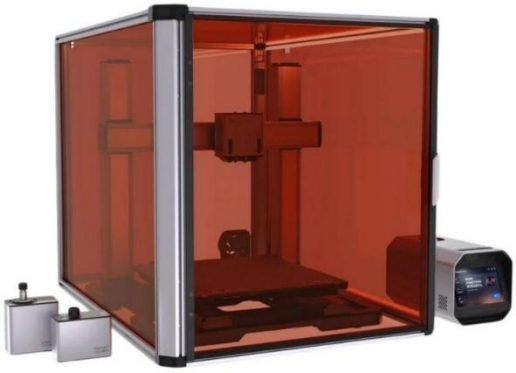

Figure 4.13 Snapmaker Artisan 3-in-1 device (Snapmaker, n.d.)



Figure 4.14 Primary experimental set-up for machining parameters (4 Samples + 1 Dummy) (Personal archive, 2026)



Figure 4.15 Snapmaker Artisan 3-in-1 machine with CNC Module (Personal archive, 2026)

During the experiments, a dummy specimen made of the same material and with identical dimensions was applied to the four-sample experimental group under identical conditions to provide temperature compensation (Figure 4.14). Temperature compensation becomes particularly critical in processes where significant temperature variations may occur. In the present study, although the induced damage was limited and no substantial temperature increase was observed in the specimens (maximum recorded temperature of 28.1 °C, Figure 4.16), temperature compensation was nevertheless implemented as a precaution to ensure that thermal effects did not influence the measurement results.

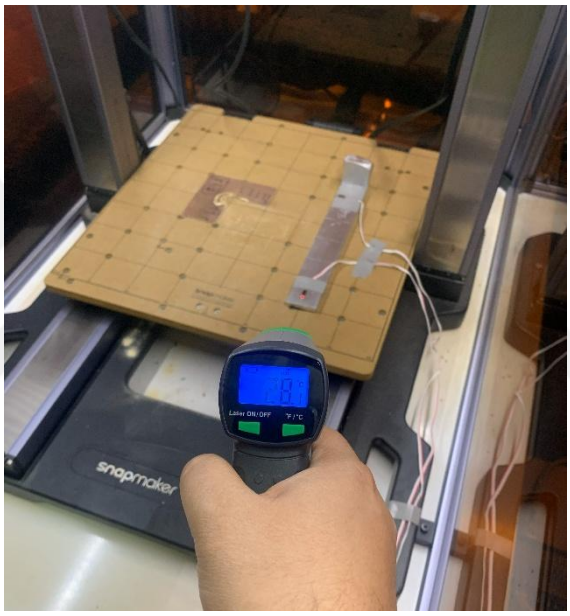

Figure 4.16 Temperature measurement after trial machining (Personal archive, 2026)

Following the application of the machining process parameters listed in Table 4.2 to the experimental setup shown in Figures 4.14 and 4.15, the obtained results are discussed in detail in the “Results and Discussion” section. However, based on the observations made at this stage, the machining parameters defined as Machining Plan #1—corresponding to a cutting speed of 18000 rpm and a feed rate of 0.2 mm/min—were identified as the most suitable conditions (Figure 4.17).

In addition, as will be detailed under the “Data Acquisition System” section, a 350 Ω quarter-bridge configuration was employed during these measurements.

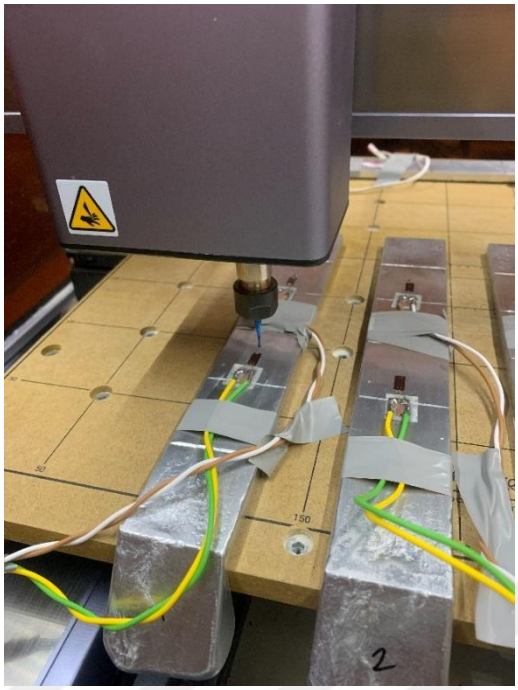

Figure 4.17 Machining Plan #1: Cutting speed 18000 rpm and feed rate 0.2 mm/min (Personal archive, 2026)

After the appropriate machining parameters had been established, a second experimental set was designed (Figure 4.19). This set aimed to compare the gravity-cast preliminary specimens cooled in air with respect to the differences between air cooling and water quenching and evaluate and compare the uniaxial strain gauge approach with the three-element rosette strain gauge configuration within the same experimental framework.

In the second experimental set, three gravity-cast preliminary specimens were involved. The first specimen in this group (Gravity Specimen #5, Figure 4.18) was water-quenched and machined using the same machining parameters as those applied to Gravity Specimen #1 in the primary experimental study. Accordingly, the only distinguishing parameter between Gravity Specimen #1 and #5 is the cooling condition, namely air cooling versus water quenching, enabling a direct comparison of the effect of cooling medium on the measured strain relaxation and residual stress response.



Figure 4.18 Gravity Specimen #5 is added to measure (Personal archive, 2026)

At this stage, it should be noted that a uniaxial strain gauge was used on Gravity Specimen #5 in the second experimental set-up. Since the strain gauge applied was the same Kyowa KFGS-5-350-C1-11 L2M3R (350 Ω) model as in the first set-up, the measurements were carried out using a 350 Ω dummy gauge, identical to that employed in the primary experimental configuration, to ensure proper temperature compensation and measurement consistency.

In the second experimental setup, Gravity Specimen #6 and Gravity Specimen #7 were processed using the previously determined optimal machining parameters. Unlike the uniaxial strain gauges employed in the earlier experiments, three-element rosette strain gauges capable of measuring strain in three directions (Vishay, model CEA-06-120CZA-120) were applied to these specimens. The distinguishing parameter between these two specimens was the cooling condition, with Gravity Specimen #6 being air-cooled and Gravity Specimen #7 water quenched.

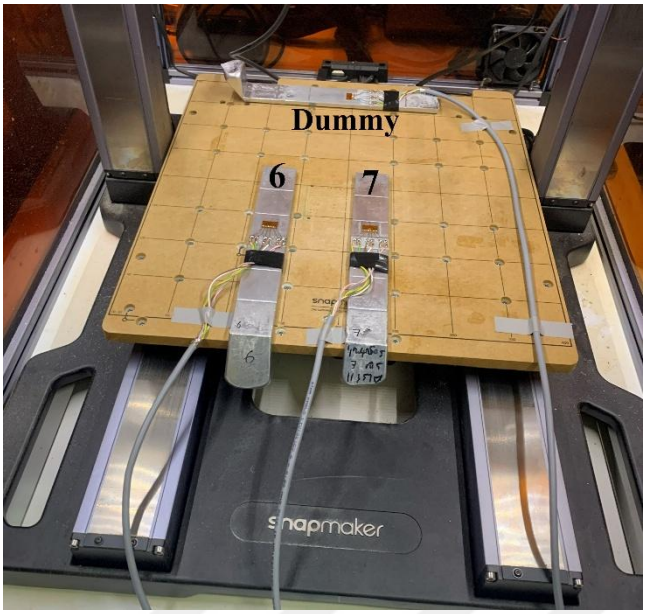

Figure 4.19 Gravity Specimen #6 and #7 (Personal archive, 2026)

It should be noted that, since the Vishay CEA-06-120CZA-120 strain gauges applied to Gravity Specimen #6 and Gravity Specimen #7 have a nominal resistance of 120 Ω, a dummy specimen equipped with a 120 Ω strain gauge was used in the second experimental setup. Accordingly, a 120 Ω quarter-bridge configuration was employed during these measurements to ensure proper signal conditioning and temperature compensation.

Thus, following the primary experimental setup in which the appropriate machining parameters were identified, the second experimental setup was designed to systematically reveal both the differences between uniaxial and rosette strain gauge measurements and the differences between air-cooled and water-cooled specimens within each measurement approach.

4.3.2.2 Low-Pressure Cast Wheel Specimens

In this section, the experimental procedures applied to the low-pressure cast wheel specimens, which were produced under industrial conditions and represent a commercial product supplied to the automotive wheel industry, are described in detail. The strain gauges applied to the wheel specimens for residual stress measurements

were Vishay CEA-06-062UM-120 rosette strain gauges (Figure 4.20). According to the relevant standard, these gauges correspond to the Type B rosette configuration (Figure 3.11).

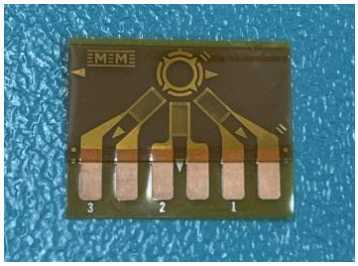

Figure 4.20 Rosette strain gauge -Vishay, CEA-06-062UM-120 (Personal archive, 2026)

The application procedure for the rosette strain gauges followed the same steps described in the previous section, including surface roughness preparation, surface cleaning, and gauge bonding. In contrast to the preliminary specimens, the positioning of the rosette strain gauges on the wheel specimens required careful consideration of both the geometric suitability of the cast wheel for strain gauge application and the probability of residual stress concentration. Taking these factors into account, the most suitable application area for the selected wheel model was identified as the region between the hub and the spoke. Accordingly, surface preparation was completed in this region prior to strain gauge installation (Figure 4.21).



Figure 4.21 Prepared surface area for rosette strain gauges (Personal archive, 2026)

The rosette strain gauge was then applied to the prepared surface. During this step, particular attention was paid to the proper placement of the strain gauge without inducing damage or fracture, as well as to the correct adhesive application and curing procedures, all of which are critical factors that can directly influence measurement accuracy (Figure 4.22).



Figure 4.22 Rosette strain gauge on the wheel (Personal archive, 2026)

To prevent potential issues that may arise during wiring and measurement, and to improve the reliability of the connections between the rosette strain gauge leads and the wiring points, a strain gauge terminal was positioned between the rosette strain gauge and the data acquisition system. This terminal was placed near the rosette strain gauge in order to minimize possible lead-wire resistance effects (Figure 4.23).



Figure 4.23 Strain gauge terminal near the rosette strain gauges (Personal archive, 2026)

Essentially, the same approach is also applicable to the gravity-cast preliminary specimens, and terminal blocks were similarly implemented for those samples. However, considering that the strain gauges used for residual stress measurements are both relatively costly and associated with long purchase lead times, the implementation of this precaution becomes particularly meaningful.

Finally, the wiring connections between the terminal block and the data acquisition system were completed using shielded cables, and the wheel specimens were thereby prepared and made ready for measurement (Figure 4.24).



Figure 4.24 Wiring of rosette strain gauge on the wheel (Personal archive, 2026)

The wheel specimen prepared for measurement was positioned on the Snapmaker Artisan 3-in-1 laboratory-scale CNC machine (Figure 4.25).



Figure 4.25 Mounting the wheel on the lab scale CNC machine (Personal archive, 2026)

The cutting tool was positioned, via the CNC spindle, over the location defined by the Vishay CEA-06-062UM-120 rosette strain gauge and prepared for the hole-drilling operation (Figure 4.26).

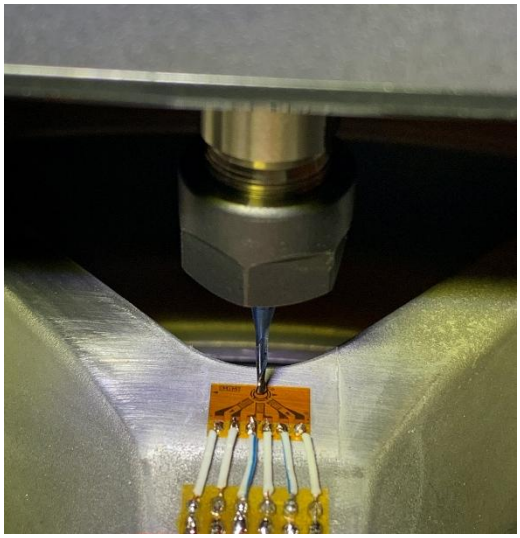

Figure 4.26 Positioning the drilling head onto the rosette strain gauge (Personal archive, 2026)

Finally, the hole was incrementally drilled at the designated location in accordance with the selected machining parameters (Figure 4.27), and the resulting data were acquired via the data acquisition system described in the following section and prepared for subsequent processing and analysis.

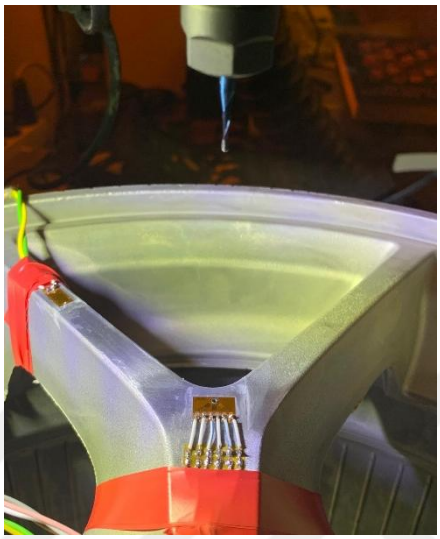

Figure 4.27 After hole drilling process (Personal archive, 2026)

4.3.2.3 Data Acquisition System

In the data acquisition system stage of this study, the measurement equipment available at the ACRL Laboratory of Dokuz Eylül University was utilized. The data acquisition setup in the ACRL Laboratory consists of strain gauges, a Wheatstone bridge, an analog-to-digital converter (ADC) module (HX711), and an Arduino Mega 2560 microcontroller.

One of the most popular techniques for measuring mechanical strain is the use of strain gauges, which employ a Wheatstone bridge to detect minute alterations in resistance to electricity when deformed.

A strain gauge calculates strain using two principles. First, a wire's resistance is determined by its length and cross-sectional area. When a load is applied, the wire's resistance will change in response to changes in the length or area of cross-section. (Equation 4.1) can be used to express a piece of wire's resistance (Kip et al., 2025).

$$R = \frac{\rho L}{A} \tag{4.1}$$

The wire's electrical resistance is represented by R (Ω), its length is indicated by L (m), and its resistivity is shown by ρ. One basic structural material attribute that varies with temperature is resistivity. A stands for the wire's cross-sectional area.

In addition, there is a correlation between the strain and this change in the wire's resistance. Equation 4.2 provides the way for controlling this, which is determined by a parameter called the "Gauge Factor" (Kip et al., 2025).

$$GF = \frac{\Delta R/R}{\varepsilon} \tag{4.2}$$

GF is the strain gauge's Gauge Factor. ΔR/R is calculated by dividing the change in resistance by its nominal resistance. The measured strain is denoted by ε.

Within the scope of this study, both 350 Ω uniaxial strain gauges and 120 Ω rosette strain gauges were used. Accordingly, Wheatstone bridge configurations incorporating 350 Ω and 120 Ω resistors were used (Figure 4.28). To ensure adequate measurement accuracy and sensitivity, precision resistors with a tolerance of ±1% were selected.

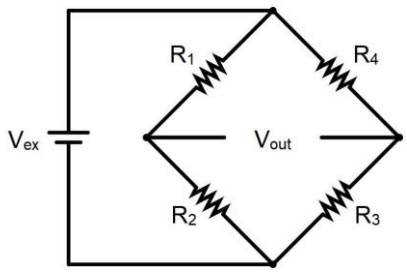

Figure 4.28 Wheatstone bridge (Kip et al., 2025)

In the configured quarter-bridge circuit, one strain gauge was incorporated as a dummy gauge for temperature compensation purposes, while the other strain gauge was used in an active configuration to sense strain.

Based on Kirchhoff's current law applied to this bridge configuration, the relationship between the excitation voltage V_{ex} and the output voltage V_{out} is obtained

as given in Equation 4.3. For accurate strain measurements, the Wheatstone bridge must be balanced, meaning that the resistances R_1 and R_2, as well as R_3 and R_4, are required to be equal. (Kip et al., 2025).

$$V_{out} = \left(\frac{R_3}{R_3 + R_4} - \frac{R_2}{R_1 + R_2}\right) V_{ex} \tag{4.3}$$

The strain gauge takes the position of resistors R3 and R4. The resistance R4 is positioned so that it is not subjected to elongation and is referred to as a dummy gauge for temperature compensation, whereas the resistance R3 is the active gauge. As seen in Figure 4.29, resistances R2 and R1 can be chosen to be set resistance (Kip et al., 2025).

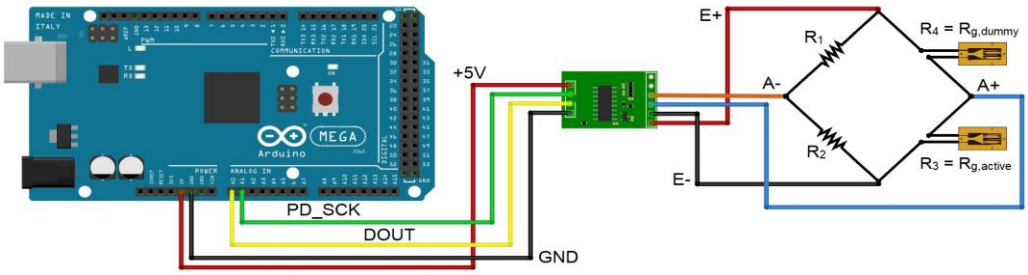

Figure 4.29 The wiring diagram of the measuring system (Kip et al., 2025)

The Analog-to-Digital Converter HX711 amplifier for bridge excitation and conditioning the output signal is used once the bridge configuration is finished. It makes it possible to convert the analog signal into a digital signal and amplify the output voltage in millivolts, which is produced by slight changes in resistance. The ADC HX711 library makes it simple to link Arduino Mega 2560 to control and read the measurement.

CHAPTER FIVE
RESULTS AND DISCUSSION

In this section of the study, the results obtained from the experimental investigations carried out in the “Experimental Study” chapter are presented. The findings are discussed in detail and evaluated considering the literature and industrial knowledge and experience reviewed in the “State of the Art and Literature Review” section.

Considering the three main subsections of the “Experimental Study” chapter—namely “Material and Casting,” “Heat Treatment Applications,” and “Residual Stress Calculation and Measurement”—the results and discussions in the “Results and Discussion” chapter are structured in a manner consistent with these sections.

However, to facilitate clearer comparison and understanding of the results, the findings related to specimens in the as-cast condition and those subjected to heat treatment are presented under a single, consolidated subsection entitled “Material and Heat Treatment Results.” This approach was adopted because discussing the results from the “Material and Casting” and “Heat Treatment Applications” sections together enable a more direct and comprehensible comparison between untreated and heat-treated specimens.

Within the “Material and Heat Treatment Results” section, the chemical composition analysis results of the investigated aluminum alloy are first presented and their compliance with the specified alloy requirements is discussed.

Subsequently, macrostructural analyses conducted on the aluminum alloy wheel product are reported, and the suitability of the observed macrostructures is evaluated with reference to the relevant standards. After the macrostructural analysis, microstructural analyses are performed. These analyses are carried out on both as-cast wheels and heat-treated wheels, enabling a direct comparison of the microstructural differences induced by the applied heat treatment conditions.

In the subsequent step, Brinell hardness (HB) test results obtained from three critical regions commonly defined in the literature—namely the spoke, inner flange, and outer flange—are presented for both as-cast and heat-treated aluminum alloy

wheels. Finally, tensile test results, obtained in accordance with the relevant standards from tensile specimens extracted from the same three regions of the aluminum alloy wheel, are reported and comparatively evaluated.

Under the “Residual Stress Results” heading, residual stress evaluations are first presented for the investigated wheel model using the Magmastress module of the Magmasoft software, and these results are discussed under the subheading “Analytical Method Results.” In line with the approach adopted in the previous subsection, residual stress calculations are performed separately for as cast and heat-treated wheels, allowing for a direct comparison of the effects of heat treatment on residual stress formation.

In addition, for a subset of the heat-treated wheels, residual stress calculations are carried out at different stages of the heat treatment process—namely after solution treatment, after quenching, and after aging—using the Magmasoft software and its Magmastress module, to assess the evolution of residual stresses throughout the heat treatment sequence.

Finally, experimental results obtained using the hole drilling method on wheel specimens in the as-cast condition as well as under different heat treatment states are presented. All analytical and experimental findings are then evaluated collectively within a comprehensive framework to provide a comprehensive assessment of residual stress behavior in the studied aluminum alloy cast components.

5.1 Material and Heat Treatment Results

5.1.1 Chemical Analysis Results

The chemical composition of the AlSi11Mg alloy used both for the test specimens and for the aluminum alloy wheel material in this study was determined in accordance with the standards detailed in the “Experimental Study” chapter. The analysis was carried out using a calibrated and accredited ARL 8820 Optical Emission Spectrometer (OES), and the resulting chemical composition is presented in Table 5.1.

Table 5.1 Chemical Analysis of Cast AlSi11Mg Aluminum Alloy

Chemical Composition	Si	Fe	Cu	Mn	Mg	Zn	Ti	Sr	Al
AlSi11Mg	10.81	0.12	0.01	0.00	0.15	0.03	0.11	0.03	88.74

When the experimentally obtained chemical composition is compared with the reference values given in Table 3.1, it is observed that all elements fall within the specified composition ranges or remain below the reported maximum limits. Accordingly, the alloy used in this study is confirmed to comply with the compositional limits defined in literature. In addition, since the alloy was cast within "Döktaş Dökümcülük Tic. ve San. A.Ş." it can be noted that it also satisfies the proprietary specifications defined by the relevant automotive suppliers.

5.1.2 Microstructure and Macrostructure

The specimens prepared in accordance with standard metallographic preparation procedures were examined using a calibrated and accredited optical microscope available at the laboratories of "Döktaş Dökümcülük Tic. ve San. A.Ş."

Macrostructural examinations were carried out by etching the cross-sections taken from different regions of the aluminum alloy wheel (Figure 5.1).

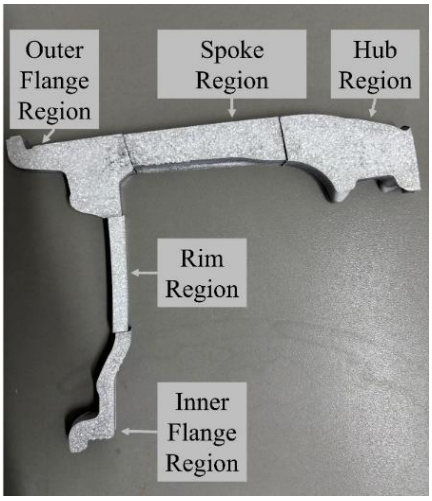

Figure 5.1 Macrostructure of wheel cross-section and regions (Personal archive, 2026)

The macrostructures were classified by comparison with the reference structures defined by the American Foundrymen's Society (AFS) in accordance with ASTM Procedure E112, as commonly practiced in many industrial organizations.

Table 5.2 Microstructures of All Options

	X50 (Scale: 500μm)	X100 (Scale: 200μm)	X200 (Scale: 100μm)
Option #1	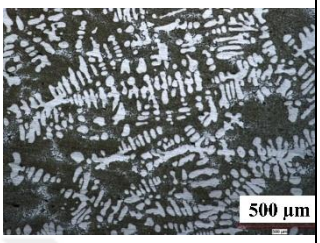	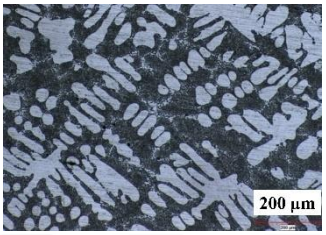	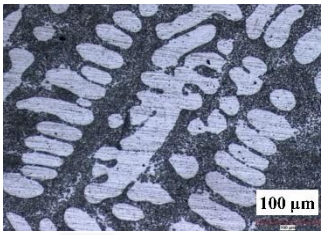
Option #2		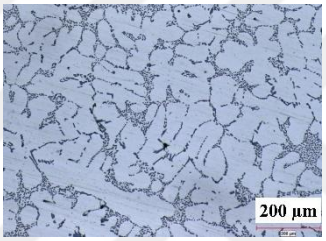	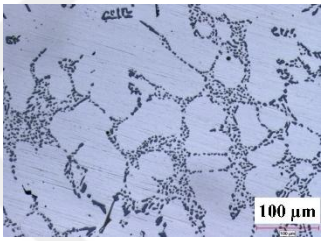
Option #3	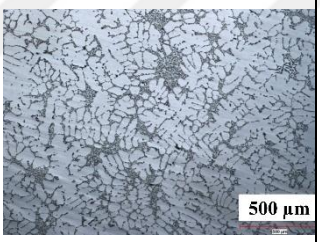	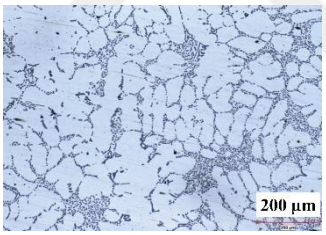	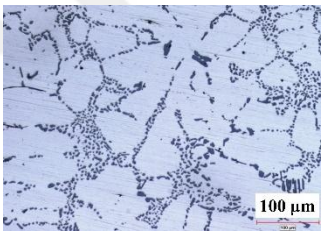
Option #4	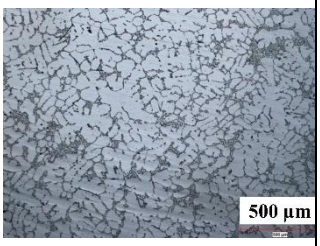	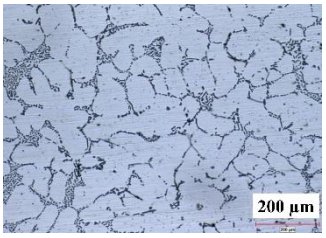	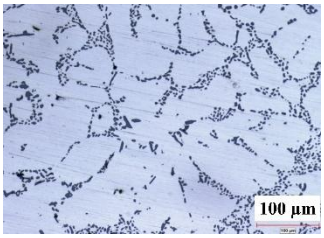
Option #5	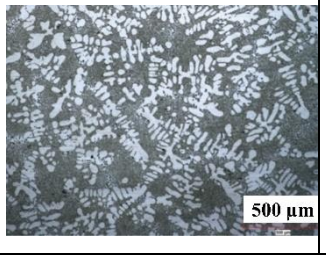	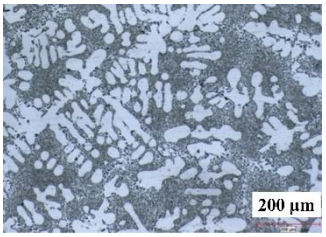	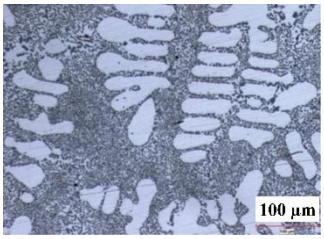

Based on this comparative evaluation, the macrostructures described above were assessed to have a grain size value of 4. This corresponds to an ASTM macro grain size number of 10.5, which is equivalent to approximately 125 grains per cm^2.

Table 5.2 shows microstructural images taken from the samples cut from the spoke region (Figure 5.1) for each option that is fixed in experimental study (Table 4.1) phases.

The sample shown in the above table under Option #1 (as-cast condition) exhibits a clearly dendritic solidification structure with coarse, clearly defined dendritic arms. High porosity risks, segregation, and structural heterogeneity are usually linked to this morphology. As a result, comparatively poor mechanical performance is anticipated, especially regarding tensile strength. Furthermore, it should be mentioned that this kind of dendritic structure adds to brittle fracture behavior and raises the possibility of crack initiation.

In Options #2, #3, and #4, the dendritic structure was significantly modified, resulting in a more spheroidized microstructure. The heat treatment refined the Si particles and gave them a comparatively spheroidized shape. These Si structures are clearer to see at higher magnifications. This microstructure was formed in part by the partial dissolution of Si during the solution treatment step and the fine and distributed precipitation during the aging process. Higher tensile strength and hardness values are therefore expected when compared to the as-cast condition. Hardness and tensile strength in Al-Si-Mg alloys under T6 heat treatment are expected to be much greater than those under as-cast and brief heat treatment (stress relief annealing) conditions. The microstructural investigations showed notable parallels between Options #2, #3, and #4, where variations are restricted to the artificial aging step of the T6 process. As a result, no significant differences in hardness or tensile strength are anticipated between these choices.

With coarse and sharp dendritic arms and a comparatively coarse eutectic Si morphology, Option #5's dendritic morphology is very similar to the as-cast condition. In contrast to Option #1, there might have been some precipitation hardening; Microstructural variability is still evident, though. As a result, the mechanical

performance is expected to be higher than that of the as-cast samples but worse in terms of hardness and tensile strength when compared to the homogenous structures formed following T6 heat treatment.

5.1.3 Hardness and Tensile Test Results

Similar to the procedures applied for chemical analysis and microstructural and macrostructural preparation and examination, the experimental protocols for tensile and hardness testing were also carried out in the laboratories of "Döktaş Dökümcülük Tic. ve San. A.Ş."

Tensile tests were performed using a Shimadzu AG-I 100 kN universal testing machine in accordance with EN ISO 6892-1:2016, employing test specimens prepared in compliance with the DIN 50125 standard.

Brinell hardness tests were performed in accordance with the ASTM E10 standard using a QNESS CS EVO 250 hardness testing system. As seen in Figure 5.1, measurements were taken from the specimens designated inner flange, outer flange, and spoke regions.

The findings of the tensile and hardness tests conducted on the specimens prepared in compliance with the previously mentioned specifications are reported in the present section of the study. Table 5.3 and Figure 5.2 describe the tensile test results and hardness values for the inner flange, outer flange, and spoke—the three key parts of the wheel product.

The dendritic and heterogeneous microstructure seen in the non-heat-treated Option #1 specimens produced the lowest tensile test results when compared to the other alternatives, which is in line with the predictions stated in the subheading "Microstructure and Macrostructure".

Higher ultimate tensile strength (UTS) and yield strength (YS) were not achievable due to this structure's brittleness. The inner and outer flanges showed comparable values across nearly all possibilities when the wheel's regional results are considered, with the inner flange typically exhibiting slightly higher UTS and YS. The inner flange

solidifies first during the low-pressure casting process, which explains this phenomenon.

Table 5.3 Mechanical Properties of AlSi11Mg Aluminum Alloy on Different Areas

		Yield Strength [MPa]	Ultimate Tensile Strength [MPa]	Elongation [%]	Hardness Brinell [HB]
Option #1	Inner Flange	114.80 ± 0.1	199.80 ± 2.66	7.92 ± 0.35	56.45 ± 0.8
	Outer Flange	115.27 ± 0.33	202.38 ± 4.66	9.50 ± 0.97	55.95 ± 0.25
	Spoke	115.02 ± 2.11	170.01 ±1.39	3.24 ± 0.35	55.8 ± 0.55
Option #2	Inner Flange	192.57 ± 7.03	275.34 ± 11.79	13.95 ± 3.88	81.4 ± 0.8
	Outer Flange	191.15 ± 4.05	267.41 ± 23.43	11.78 ± 6.16	81.4 ± 0.1
	Spoke	170.86 ± 27.32	216.0 ± 27.85	3.67 ± 2.22	73.35 ± 0.05
Option #3	Inner Flange	190.70 ± 5.71	274.08 ± 8.78	14.56 ± 2.29	85.95 ± 0.75
	Outer Flange	188.58 ± 4.83	267.34 ± 8.97	13.33 ± 4.48	83.65 ± 1.85
	Spoke	166.96 ± 5.78	211.09 ± 17.19	3.49 ± 1.84	82 ± 0.1
Option #4	Inner Flange	174.43 ± 11.19	258.85 ± 13.65	15.82 ± 1.22	83.15 ± 0.15
	Outer Flange	173.86 ± 10.56	255.42 ± 13.71	14.79 ± 4.59	81 ± 0.1
	Spoke	155.98 ± 11.65	204.49 ± 15.54	4.24 ± 1.26	73.85 ± 0.75
Option #5	Inner Flange	117.96 ± 1.53	202.12 ± 18.17	9.02 ± 4.35	59.2 ± 2.2
	Outer Flange	117.16 ± 0.94	210.36 ± 2.5	10.69 ± 1.04	58.55 ± 1.55
	Spoke	117.57 ± 1.33	188.26 ± 12.16	4.18 ± 1.36	61.3 ± 0.7

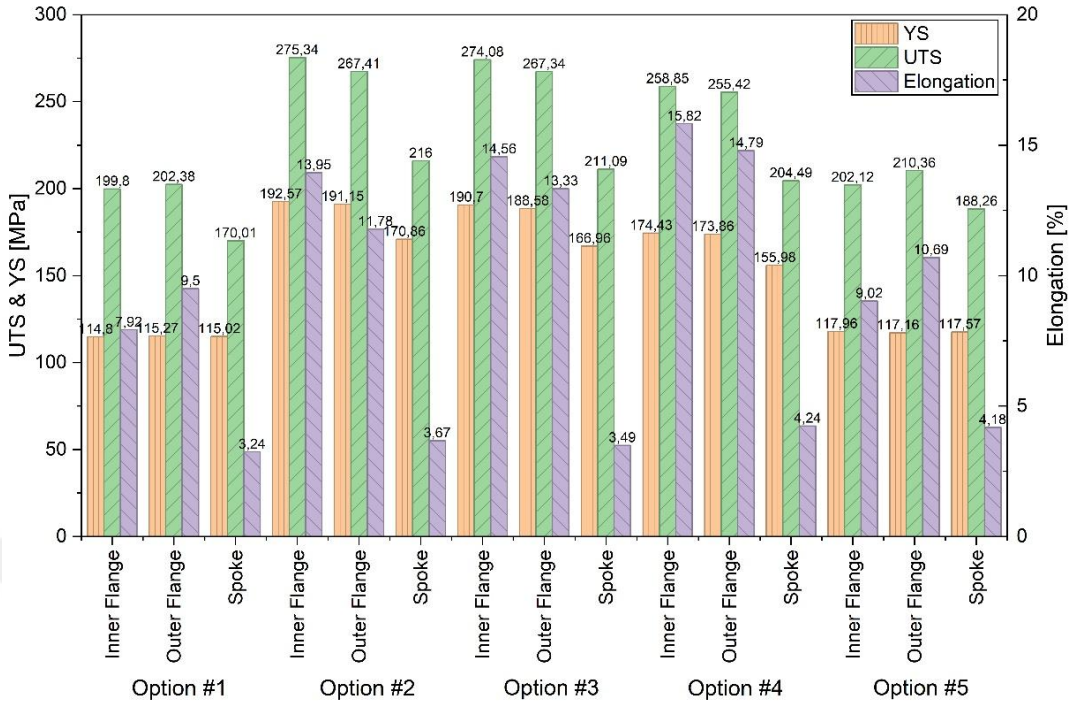

Figure 5.2 Results of UTS [MPa], YS [MPa] and Elongation [%]

The spoke region consistently had the lowest UTS and YS values because solidification moves through the inner flange, outer flange, and spoke in that order. Elongation showed the same trend, with the spoke region showing far lower values than the other regions because it solidified last. The T6-treated Options #2, #3, and #4 had the highest hardness values, whereas Option #1, which did not apply any heat treatment, had the lowest hardness.

Figure 5.3 provides a detailed presentation of the hardness values. Option #1 showed the lowest hardness values among the samples in all three regions (spoke, outer flange, and inner flange), while there were no noticeable differences across the regions. Similarly, partial precipitation hardening produced a limited increase in hardness in Option #5, which had a limited heat treatment (artificial aging only). Similar to Option #1, there was no noticeable variance in change between the various wheel sections. Although it would normally assume that the spoke, as the final solidifying location, would have the lowest hardness, the differences across the regions were negligible, most likely because the hardness levels were typically low. Comparing Options #1 and

#5, Option #5 showed a comparatively slight improvement in the average hardness values of the designated wheel regions—roughly 6%.

On the other hand, when compared to Options #1 and #5, the T6 heat-treated Options #2, #3, and #4 showed a clear improvement in hardness. This result agrees with the homogeneous and dissolved dendritic microstructures found, which provide predictable outcomes. Option #2 showed a significant rise, especially in the flange regions, with hardness values as high as 81.4 HB; however, the spoke showed a lower value (73.35 HB), potentially because of its later solidification. A similar trend was clearly obvious in Option #4, whereas in Option #3, although a comparable trend was expected, the improvement was more uniform. The hardness values of Option #3 (inner flange: 85.95 HB, outer flange: 83.65 HB, spoke: 82 HB) were the highest of all conditions, suggesting a more uniform distribution across regions. Due to less precipitation hardening, Option #5 performed better than Option #1, but it was still far below the results for Options #2, #3, and #4. Options #2 and #4 showed excellent performance in certain areas, but their overall structural consistency suffered by the spoke's lower hardness values. Option #3, on the other hand, proved to be the most beneficial condition, providing continuously high and balanced hardness throughout all locations. Nevertheless, when Options #2, #3, and #4 are compared with one another, the differences in average hardness across the defined wheel regions were relatively minor, on the order of 5–6%.

Lastly, Option #1's hardness values were found to be comparable to the literature values (Table 3.2), but Options #2, #3, and #4's hardness values exceeded the reported ranges. The ultimate tensile strength (UTS), yield strength (YS), and elongation (%) obtained from tensile testing are compared in the following figures (Figures 5.4–5.6). The distinctive heat treatment used in Options #1 through #5 has a noticeable effect on the properties of the material.

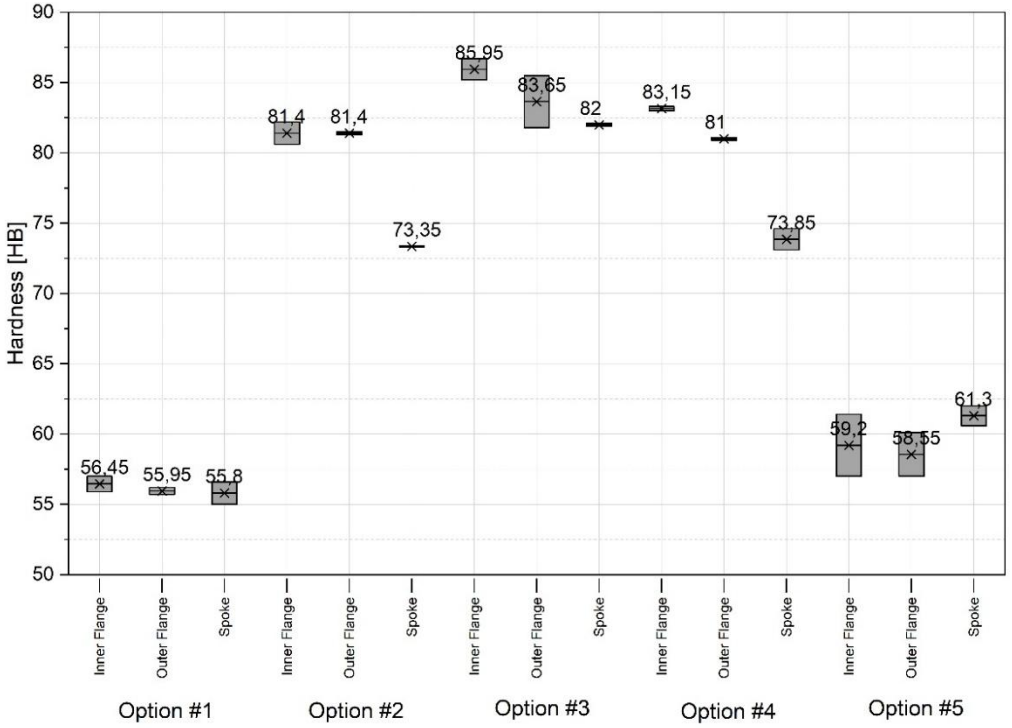

Figure 5.3 Results of Hardness Brinell [HB]

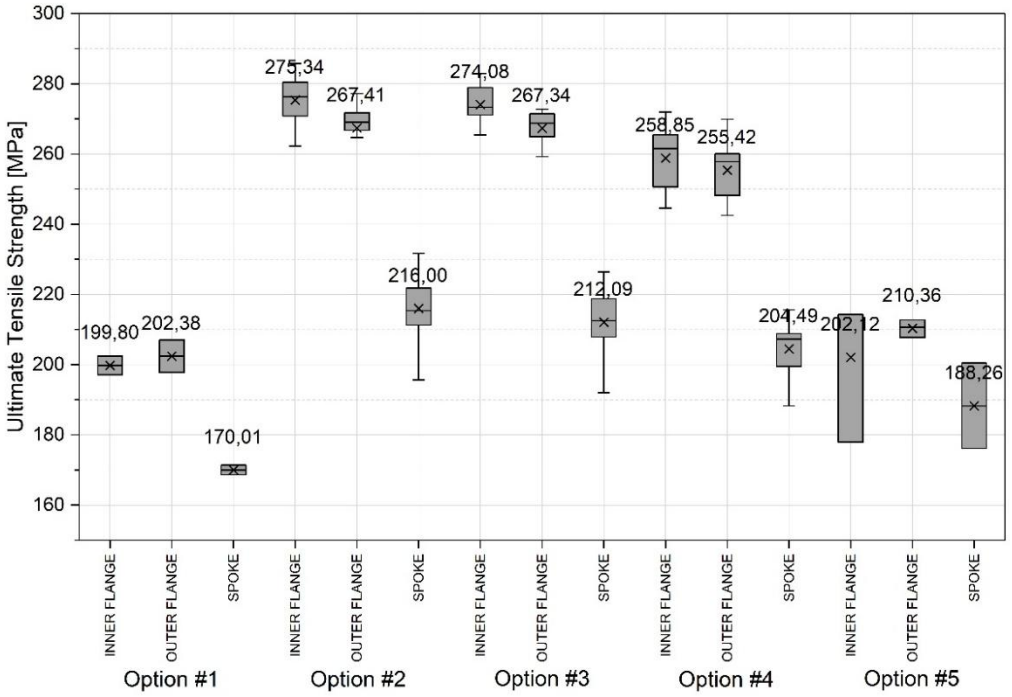

Figure 5.4 Results of Ultimate Tensile Strength (UTS) [MPa]

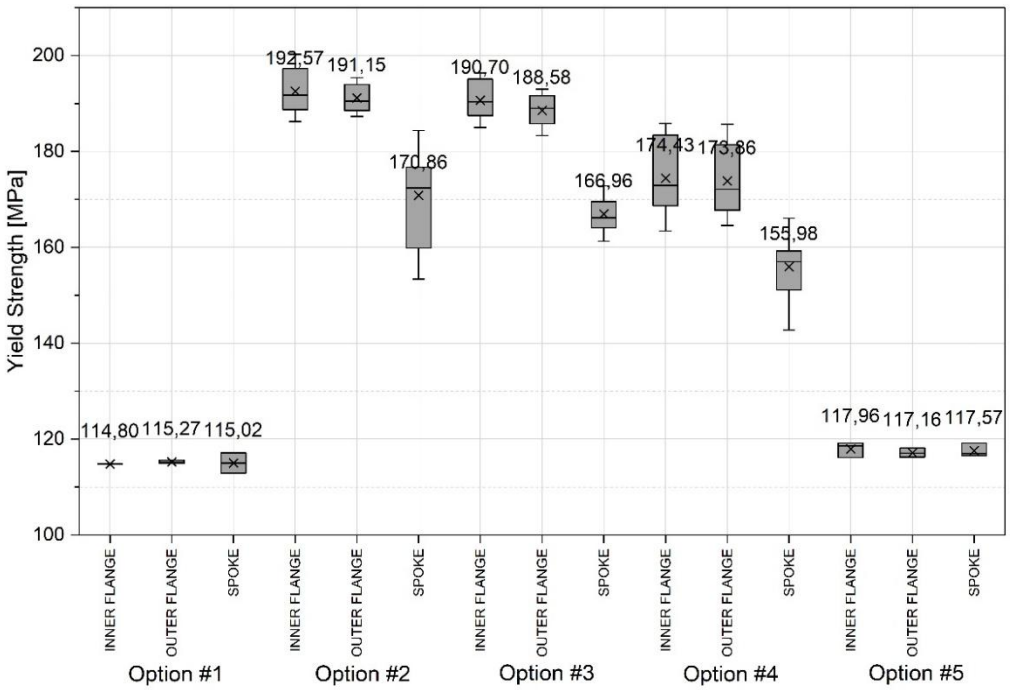

Figure 5.5 Results of Yield Strength (YS) [MPa]

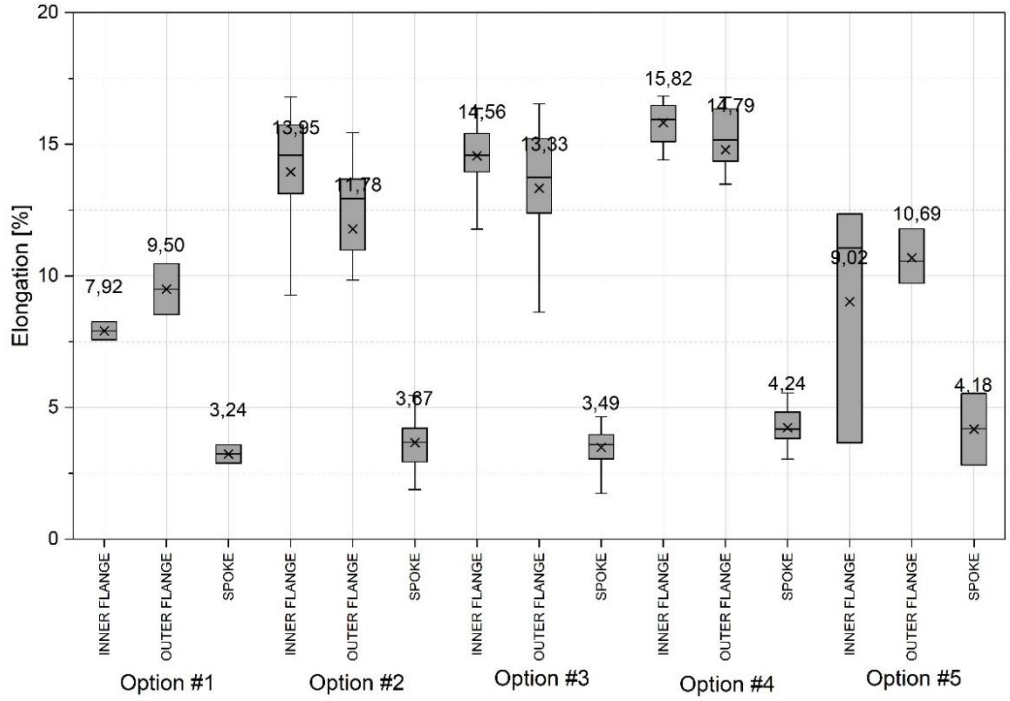

Figure 5.6 Results of Elongation [%]

The T6-treated groups (Options #2, #3, and #4) provide the highest UTS, YS, and elongation values in comparison to the other conditions, according to a thorough analysis of Figures 5.4–5.6, which report UTS, YS, and elongation, respectively. Option #2 (longer artificial-aging time: 150 min) and Option #3 (middle artificial-aging time: 120 min) provide results that are nearly the same regarding UTS and YS.

At this point, Option #3 seems to be the best option when the previous hardness data is considered. Option #4 exhibits the lowest tensile results (UTS and YS) among the T6-treated groups. These results suggest that to produce the best combinations of mechanical characteristics and hardness, a minimum artificial-aging time of 120 minutes (as in Option #3) is advised. Across different wheel locations, UTS drops of 5–6% and YS decreases of 7–9% were noted with a shorter artificial-aging time of 90 minutes (as in Option #4). On the other hand, increasing the artificial-aging time to 150 minutes (Option #2) only produces small improvements and offers no noticeable advantage.

As expected, the T6-treated specimens exhibit lower UTS and YS in the spoke—a location that cools slower during the solidification sequence—than in the inner and outer flanges when the options are compared throughout the various wheel areas (inner flange, outer flange, and spoke). The artificially aged-only Option #5 and the non-heat-treated Option #1 show a similar trend in UTS; however, the regional differences for YS under these two conditions are still quite slight.

In conclusion, it is necessary to clearly state acceptable boundaries and performance requirements at the product level before identifying a single alternative as "optimal." The current analysis shows that these expectations may differ regionally throughout the wheel's various sections as well as at the material properties.

The results show that Option #2 or Option #3 are the best options when high UTS and YS are needed, regardless of the sampling region. However, among the T6-treated conditions (Options #2, #3, and #4), Option #2's longer artificial-aging period has almost no influence on UTS and YS in the inner and outer flanges (highest differences of 1.34% for YS and 0.45% for UTS). Even if the spoke shows noticeable differences (1.8% for UTS and 2.28% for YS), these improvements are not operationally

conceivable when manufacturing restrictions are considered. Considering these facts, Option #3 is the best option for applications that mostly require strong UTS and YS.

On the other hand, Option #4 is best when relatively high elongation is prioritized. Option #4 offers elongation values that are 13–25% higher in the inner and outer flanges and 16% higher in the spoke than Option #2 (the lower-ductility condition) in the T6-treated set (Options #2, #3, and #4).

Option #5 (artificial aging only) performs better than Option #1 (as-cast, non-heat-treated) in every comparison. However, Option #5 is obviously poor when compared to the T6-treated choices, especially in terms of UTS and YS.

The spoke of a particular option has the lowest UTS, YS, and elongation values for almost all alternatives; in a few cases, any differences are insignificant. This finding emphasizes the importance of closely inspecting the spoke/hub region, where residual stress can develop. In comparison to the flanges, the continuously lower tensile values in this region suggest that residual stress may compromise structural integrity and increase risk. As a result, the necessity of residual-stress estimates and studies that are verified on representative specimens is underlined once more.

5.2 Residual Stress Results

5.2.1 Analytical Method Results

This section presents the residual stress results predicted using the Magmasoft Magmastress module for the different simulation configurations incorporating various heat treatment strategies.

As mentioned previously, the analytical investigation started with the numerical simulation of the wheel casting process based on the Low Pressure Die Casting (LPDC) technique to assess the castability of the component. Upon verification of the wheel model's castability, the study was subsequently extended using the Magmasoft - Magmastress module to evaluate residual stress distributions, which constitutes the primary focus of the present work.

It is essential to incorporate the wheel data obtained from the baseline casting simulation, which accounts for the effects of mold filling and solidification, to accurately capture their influence on the final results. Dependence only on the heat treatment stage within the Magmastress module would fail to represent the actual experimental casting process and would overlook the contribution of the filling and solidification phases to the final residual stress distribution. Consequently, the validity and consistency of the input data supplied to the Magmastress module are of fundamental importance to ensure the reliability of the residual stress predictions.

A distinguishing feature of the present study, which contributes to its originality compared to existing literature that primarily focuses on the filling and solidification stages of casting simulations, is the emphasis placed on residual stress analysis. Accordingly, this section is dedicated to presenting and discussing the results obtained from the Magmasoft - Magmastress module. Furthermore, no external mechanical loads were applied to the wheel model in the analytical investigations, enabling the residual stress state within the structure to be directly evaluated through simulation software.

The heat treatment procedures summarized in Table 4.1 were implemented within the Magmasoft - Magmastress module and applied to the wheel model obtained from the casting simulation. Accordingly, individual simulation cases were generated for each treatment option, and the resulting outputs were systematically evaluated and reported.

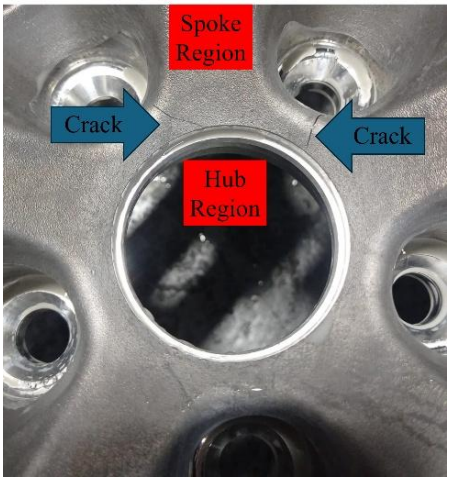

Figure 5.7 Suspected hub & hub/spoke area for cracks (Personal archive, 2026)

In all analyses, particular attention was focused on the hub and hub–spoke regions (Figure 5.7), where crack formation was also observed during the experimental trials, to maintain consistency between the numerical predictions and the actual production behavior.

For Option #1, which corresponds to the as-cast condition without the application of any heat treatment, the handling procedure—consisting of immersion in water at 70-80 °C for 20 seconds followed by air cooling—was incorporated into the simulation framework to examine its potential influence, as described in Section “Experimental Study”. Although this step is generally regarded in industrial practice as having a negligible impact on residual stress development, due to the expectation that such effects are removed during the subsequent solution treatment stage, its contribution was nonetheless quantified and reported in the present study using simulation software (Figure 5.8).

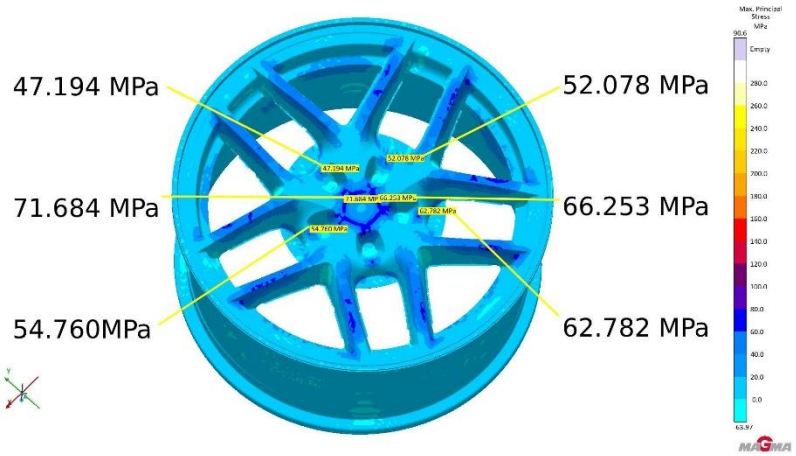

Figure 5.8 The effect of handling process on residual stress (Option #1)

The present analysis is equally applicable to the remaining heat-treated configurations, as all options originate from the same initial condition prior to the application of any heat treatment and immediately following the handling process. The residual stresses generated within the structure after handling were found to range between 66–71 MPa in the hub region and 47–62 MPa along the transition from the

hub toward the spoke. Although these stress levels are subsequently shown to vary under different heat treatment regimes, such as the T6 process, they provide a valuable reference for characterizing the residual stress state of the as-cast specimens (Option #1) before any thermal treatment is applied.

In the second phase of the investigation, numerical simulations were conducted for wheel components subjected to T6 heat treatment under Options #2, #3, and #4, which differ with respect to artificial aging duration (150 min, 120 min, and 90 min, respectively). The hub and hub–spoke regions, previously identified as critical zones with a high susceptibility to cracking in the manufactured product (Figure 5.7), were examined in detail. Within this group of T6-treated configurations, the cases representing the longest and shortest aging durations—namely Option #2 and Option #4—were evaluated first. For these conditions, residual stress assessments were performed not only upon completion of the full treatment cycle, but also at each principal stage of the T6 process (after solution treatment, after quenching, and after artificial aging), thereby enabling a comprehensive evaluation of stress evolution throughout the treatment sequence.

Figure 5.9 shows the residual stress distributions predicted by the simulation for Option #2, which corresponds to the longest artificial aging duration.

The results shown in Figure 5.9 demonstrate that, following the solution treatment stage, the structure exhibited nearly zero residual stress levels, with locally compressive stresses observed in certain regions as a result of the elevated processing temperature (Figure 5.9(a)). As expected, the maximum tensile residual stresses occurred after the quenching stage, during which the thermal gradient reached its highest magnitude. At this stage, residual stress values were found to range between 107–119 MPa in the hub region and 85–91 MPa in the region extending from the hub toward the spoke (Figure 5.9(b)). Subsequent artificial aging led to a partial relaxation of residual stresses due to the combined influence of temperature and exposure time, as confirmed by the simulation results. In this stage, residual stress levels were reduced to 101–113 MPa in the hub region and 80–86 MPa in the hub–spoke transition zone (Figure 5.9(c)). A comparison of these values with the corresponding post-quenching

stresses indicates an average stress relaxation of approximately 5.53% in the hub region and 5.69% in the hub–spoke region.

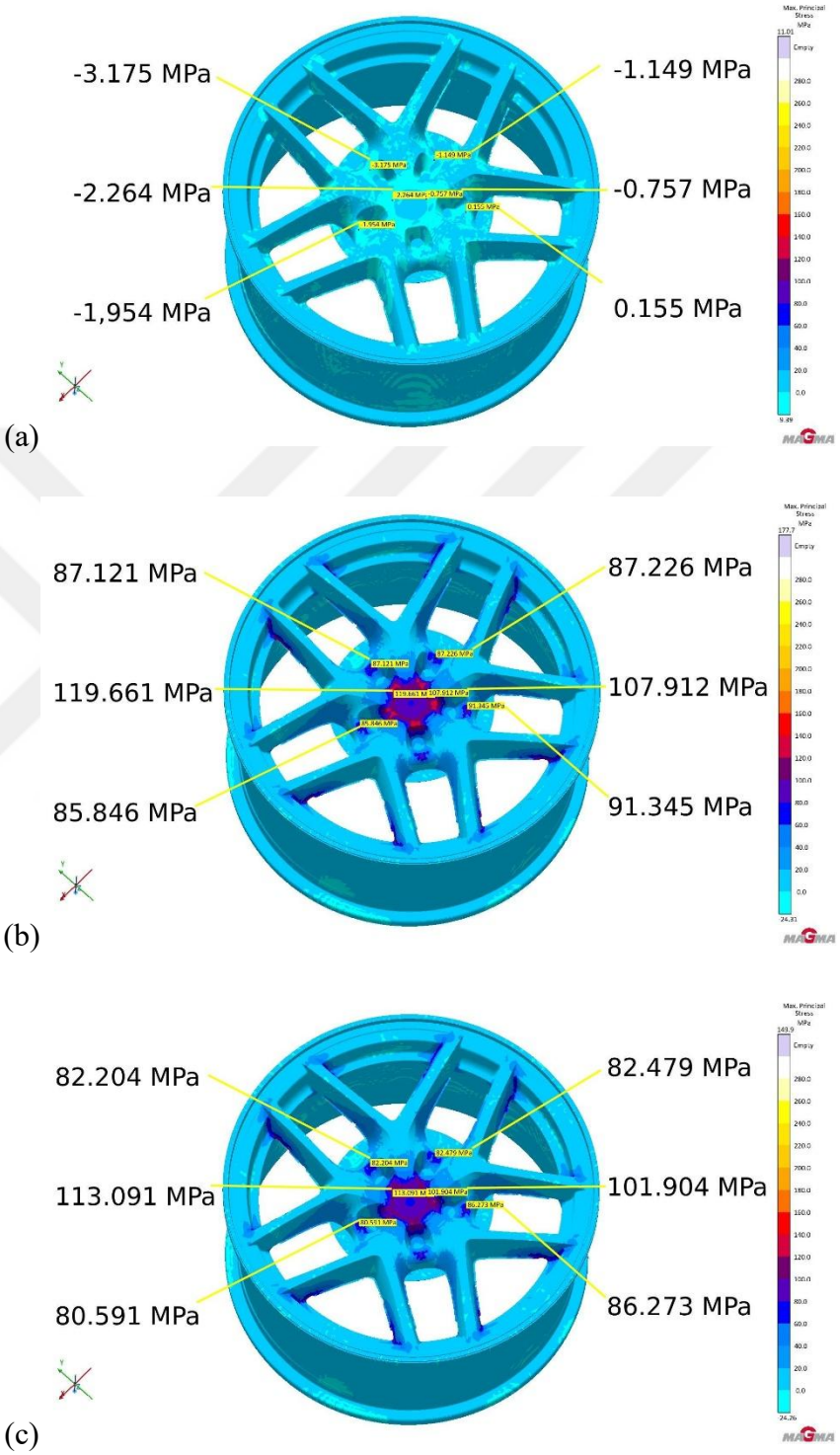

Figure 5.9 The results of Option #2 on various steps (a)After solution treatment, (b)After quenching, (c)After aging.

Using the same simulation methodology, the results corresponding to Option #4 are presented in Figure 5.10.

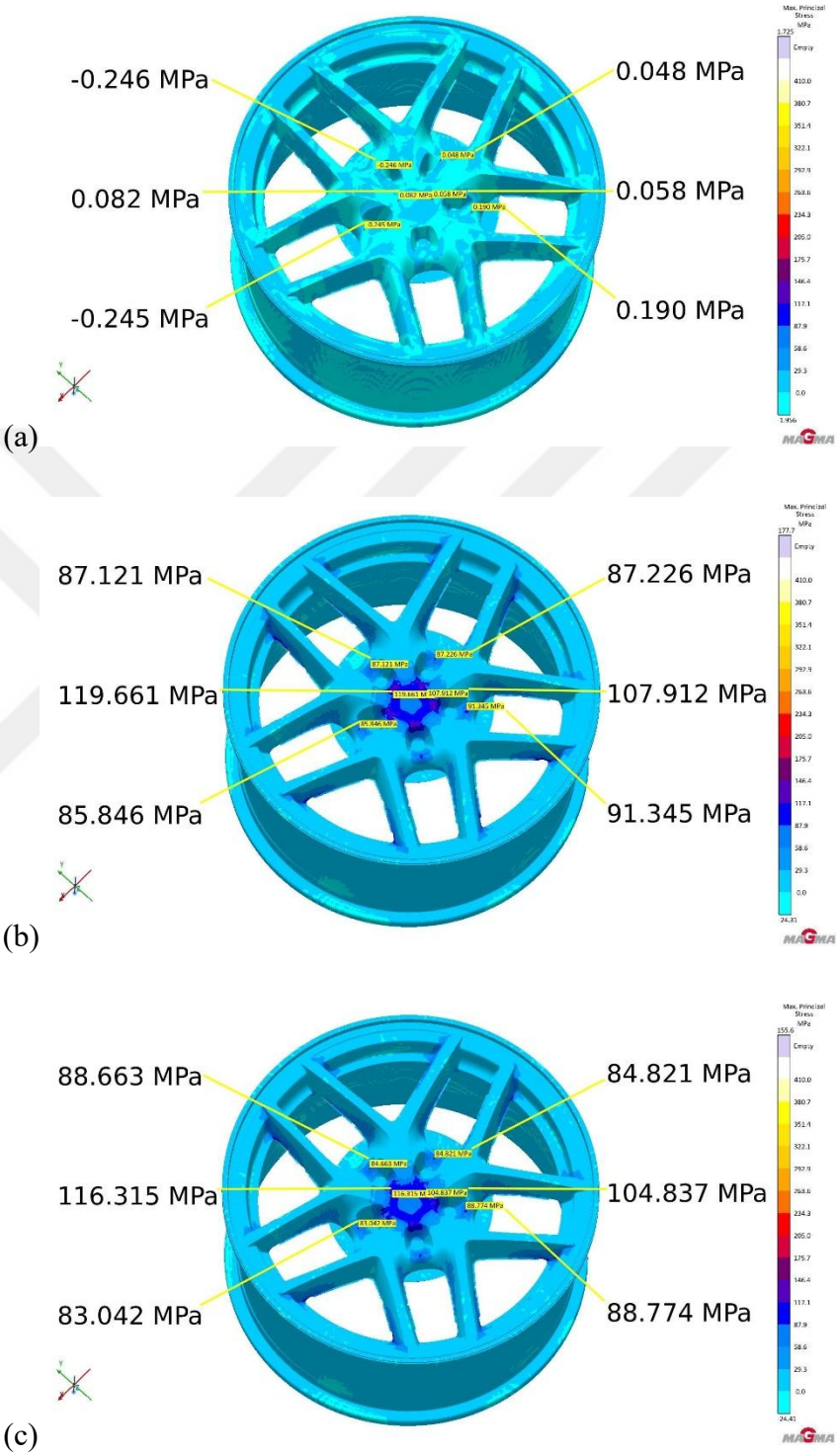

Figure 5.10 The results of Option #4 on various steps (a) After solution treatment, (b)After quenching, (c)After aging.

For Option #4, which corresponds to the shortest artificial aging duration, the results obtained using the same simulation methodology are presented in Figure 5.10 and exhibit a strong similarity to those of Option #2. During the solution treatment stage, the structure displayed nearly negligible tensile residual stresses, with locally compressive stresses observed in certain regions (Figure 5.10(a)). However, these stress levels are sufficiently small that a meaningful quantitative comparison is not feasible, and it can therefore be concluded that the residual stresses in both Option #2 and Option #4 are effectively neutralized at this stage.

Following the quenching step, at which the maximum thermal gradient is enforced, identical residual stress distributions were obtained (Figure 5.10(b)). This outcome is expected, as no modifications were introduced to the simulation parameters up to this point, despite the execution of separate simulation cases for this option. In the subsequent artificial aging stage, a partial relaxation of residual stresses was observed, with values ranging from 104–116 MPa in the hub region and 83–88 MPa in the hub–spoke region (Figure 5.10(c)). A point-by-point comparison of these results indicates an average stress reduction of approximately 2.82% in the hub region and 2.91% in the hub–spoke region.

A direct comparison between Options #2 and #4 indicates that the extended artificial aging duration applied in Option #2 (150 min) leads to lower residual stress levels than those obtained with the shorter aging time of Option #4 (90 min). Since the only difference between these two configurations is the duration of the artificial aging stage, the observed differences in residual stress can be attributed exclusively to this parameter. Specifically, Option #2 exhibits an average reduction in residual stress of approximately 2.78% in the hub region and 2.86% in the hub–spoke region relative to Option #4.

An overall evaluation of the results indicates that Options #2 and #4, both processed under T6 heat treatment conditions, yield nearly identical residual stress levels up to the post-quenching stage. However, when a longer artificial aging duration is applied (Option #2, 150 min), stress relaxation in the critical hub region exceeds 5.5%, whereas for the shorter aging duration (Option #4, 90 min), the corresponding relaxation is limited to approximately 2.8%.

Given the minimal differences observed between Options #2 and #4, considering that all simulation parameters—other than the artificial aging duration—were kept constant, Option #3 was expected to intermediate results with only minor deviation from the other two configurations. Consequently, a separate detailed analysis for Option #3 was considered unnecessary.

Based on the comprehensive evaluation of the analyses and observations, it can be concluded that among the T6 heat-treated configurations, Option #2—characterized by the longest artificial aging duration—resulted in the lowest residual stress levels. From the perspective of residual stress reduction, Option #2 can therefore be regarded as the most favorable condition. The underlying mechanism responsible for the reduction of residual stresses with increasing aging time is attributed to dislocation mobility, commonly described as dislocation relaxation, creep, or climb.

In the third and final phase of the investigation, numerical simulations were carried out for Option #5, which was subjected to a heat treatment method excluding the solution treatment and quenching steps—commonly referred to in the literature as stress-relief annealing (Wyatt et al., 2007)—and evaluated in comparison with the conventional T6 heat treatment process. By omitting the quenching stage, the procedure avoids the severe thermal gradients that are typically responsible for the generation of high residual stress levels.

Nevertheless, consistent with all other configurations, Option #5 was also subjected to the handling process inherent to the production sequence. As a result, the residual stresses originating from the handling stage, as illustrated in Figure 5.8, were transferred into the subsequent heat treatment step (155 ± 5 °C for 150 min). The evolution of residual stresses during this stress-relief annealing process is presented in Figure 5.11.

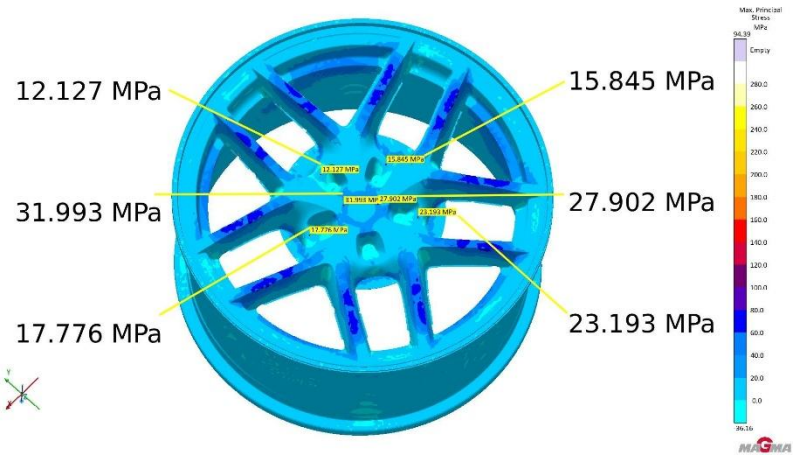

Figure 5.11 The results of Option #5 after stress relief annealing

Following the stress-relief annealing treatment, as illustrated in Figure 5.11, a detailed examination was conducted on the hub and hub–spoke regions, which have been identified as critical zones with a high susceptibility to cracking in the actual component (Figure 5.7). A pronounced reduction in residual stress was observed after the annealing process, with stress levels decreasing to 27–31 MPa in the hub region and 12–23 MPa in the hub–spoke transition region.

A comparison between the residual stress levels measured after the handling stage (Figure 5.8) and those remaining in the structure following stress-relief annealing (Figure 5.11) reveals an average reduction of 56.63% in the hub region and 68.62% in the hub–spoke region. These results clearly demonstrate the effectiveness of the stress-relief annealing treatment applied in Option #5, in agreement with the earlier comparisons between Options #5 and #1 in terms of both microstructural characterization and mechanical performance, thereby confirming its significant role in reducing residual stress.

5.2.2 Hole Drilling Method Results

Prior to presenting the residual stress measurement results obtained by the hole drilling method, a preliminary evaluation was conducted to determine the appropriate drilling parameters for the material under investigation (AlSi11Mg). For this purpose,

the local projection of the residual stress released by drilling a hole along a single direction was calculated based on uniaxial strain measurements.

Through this preliminary assessment, the local variation of residual stress was demonstrated using a uniaxial strain gauge, thereby providing a one-directional preliminary interpretation of the values to be obtained from the rosette strain gauge measurements on the wheel rim.

Before all these calculations, the output data obtained from the data acquisition system are electrical signals in the microvolt (μV) range and do not have physical meaning on their own; therefore, they must be converted into strain (ε) and consequently into stress (σ). For these conversion procedures, the formulas detailed under the section titled "Data Acquisition System", which describe the relationship between the Gauge Factor (GF) and the excitation voltage V_{ex} and output voltage V_{out} of the Wheatstone bridge (Equations 4.2 and 4.3), must be used.

When the voltages across the arms of the Wheatstone bridge (Arm A: Equation 5.1 and Arm B: Equation 5.2) are calculated accordingly;

$$V_A = V_{ex} \frac{R}{(R+\Delta R)+R} = V_{ex} \frac{R}{(2R+\Delta R)} \tag{5.1}$$

$$V_B = V_{ex} \frac{R}{R+R} = \frac{V_{ex}}{2} \tag{5.2}$$

The output voltage (Equation 5.3) is then given by,

$$V_{out} = V_A - V_B \tag{5.3}$$

$$V_{out} = V_{ex} \left(\frac{R}{(2R + \Delta R)} \right) - \frac{1}{2}$$

After performing the mathematical operations,

$$V_{out} = V_{ex} \left(\frac{\Delta R}{(4R+2\Delta R)} \right) \tag{5.4}$$

Equation (5.4) is obtained.

Thus, the resistance change $\Delta R$is calculated from the V_{out}value. Substituting this into the gauge factor equation (Equation 4.2) then enables the conversion to strain.

Following the conversion to strain, the stress value is obtained from the strain value by applying Hooke's law (Equation 5.4). Since no external load is applied to the measured component, the measured strain corresponds to the elastic strain relaxation caused by residual stresses.

$$\sigma = E \,.\, \varepsilon \tag{5.4}$$

However, it must be noted that this value represents the residual stress relaxation strain only along the axis of the uniaxial strain gauge; it does not contain information about other directions and constitutes merely an initial analysis and preliminary assessment prior to the residual stress measurement.

In the primary experimental setup (Figure 4.9), different machining parameters (Table 4.2) were applied to specimens that were identical in all other respects (material, casting and cooling conditions, hole diameter, and the relative position of the hole center and the uniaxial strain gauge) in order to investigate which machining parameters produced data within the most suitable and readable range.

At this stage, considering the required conversion formulas, the output data exhibiting the highest millivolt value in terms of the absolute difference between the maximum and minimum points were evaluated as the most appropriate. In the following figures (Figures 5.12–5.15), the data acquisition system outputs obtained from the gravity-cast preliminary specimens in the primary experimental setup (Figure 4.14), to which the machining parameters detailed in the *Experimental Study* section were applied, are presented. Since all other parameters were kept constant at this stage, no additional cycling was performed.

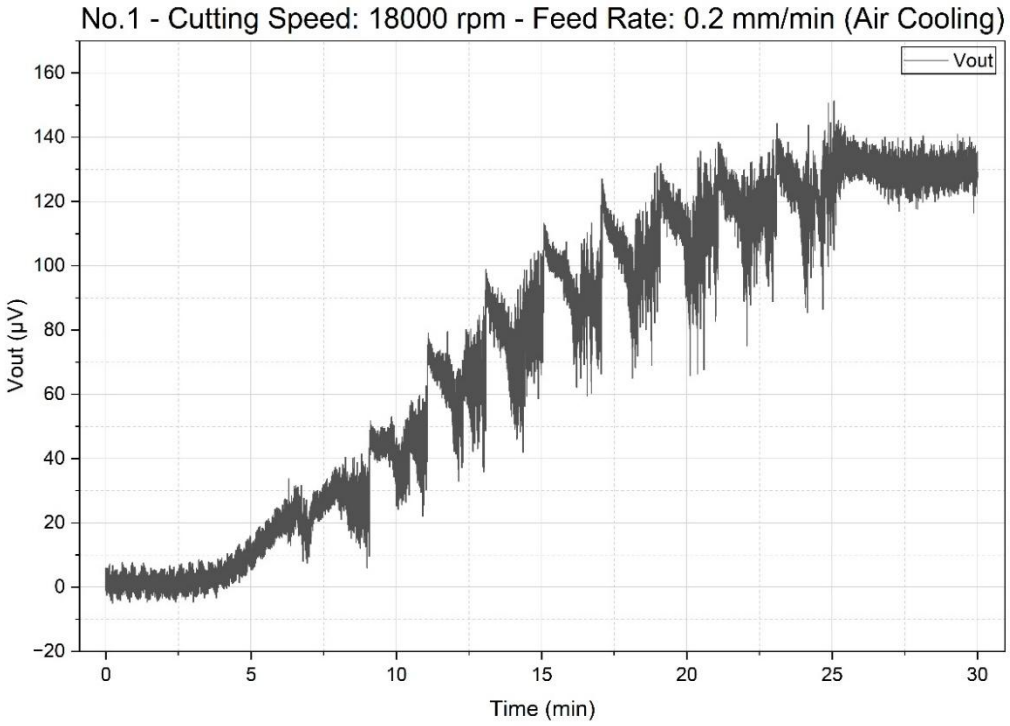

Figure 5.12 Gravity Specimen No.1 - Cutting Speed: 18000 rpm - Feed Rate: 0.2 mm/min

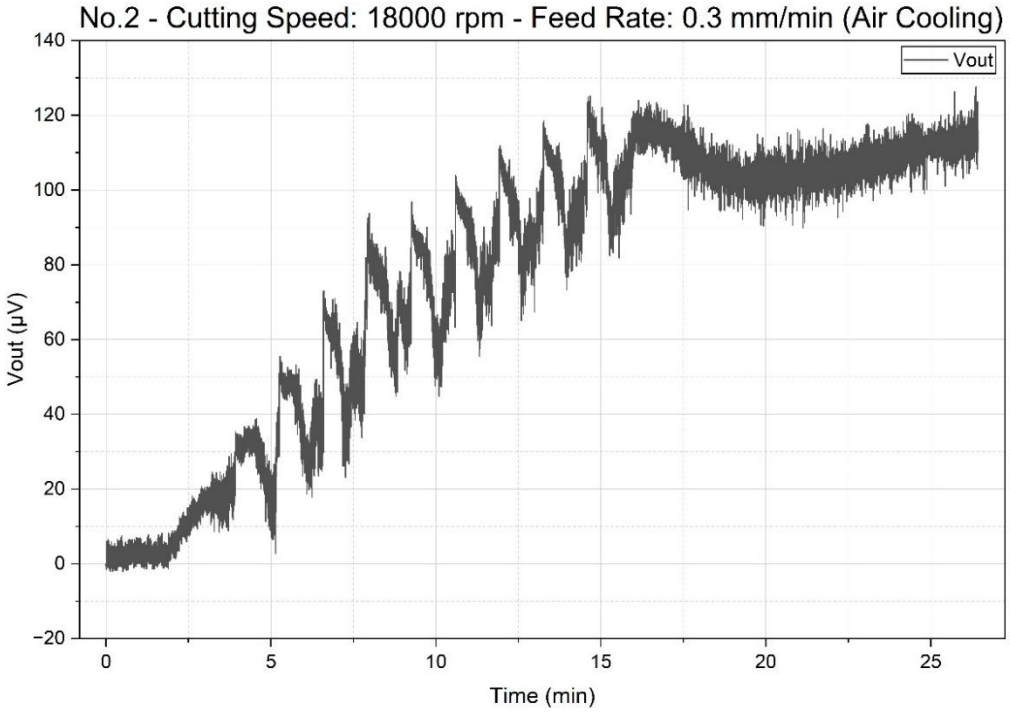

Figure 5.13 Gravity Specimen No.2 - Cutting Speed: 18000 rpm - Feed Rate: 0.3 mm/min

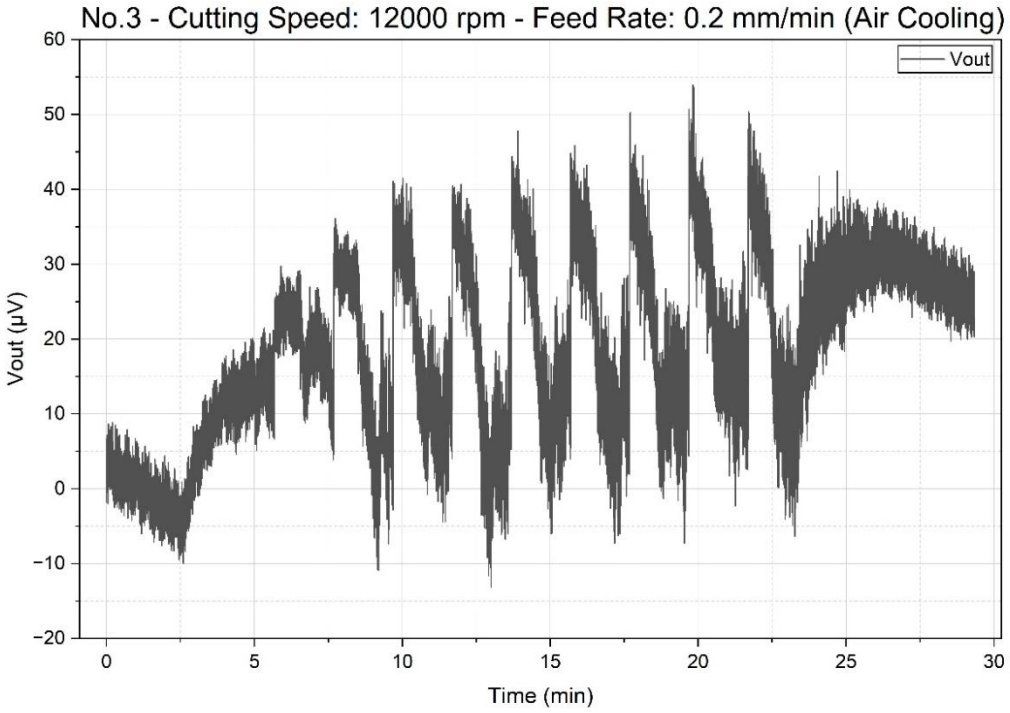

Figure 5.14 Gravity Specimen No.3 - Cutting Speed: 12000 rpm - Feed Rate: 0.2 mm/min

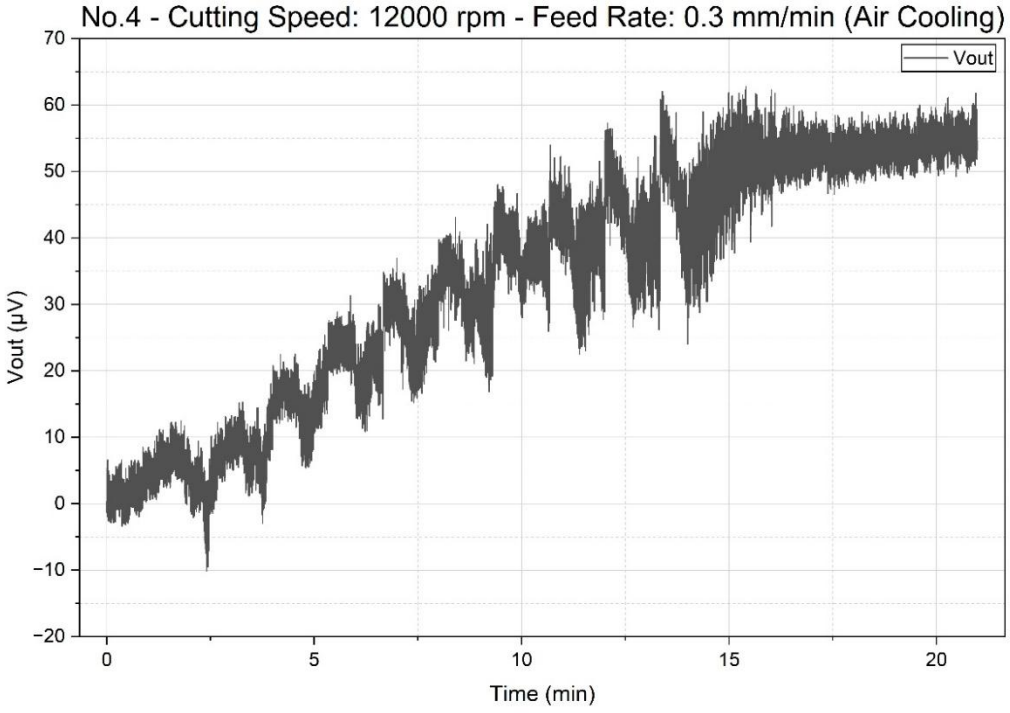

Figure 5.15 Gravity Specimen No.4 - Cutting Speed: 12000 rpm - Feed Rate: 0.3 mm/min

As previously stated, the most suitable parameters were identified as those specified in Machining Plan #1, namely a cutting speed of 18,000 rpm and a feed rate of 0.2 mm/min.

Subsequently, in the secondary experimental setup (Figure 4.9), Machining Plan #1 parameters continued to be applied to the gravity-cast specimens. At this stage, a comparison was conducted between Gravity Specimen No. 1, which was cooled in air and instrumented with a uniaxial strain gauge (Figure 5.12), and Gravity Specimen No. 5, which was cooled in water (Figure 5.16), in order to evaluate the effect of water cooling on the strain response along the strain gauge axis (Figure 5.17). During this comparison, as described above, the output voltage was converted into stress values. It should be noted that the stress obtained here corresponds to the stress relaxation caused by residual stresses only along the axis of the uniaxial strain gauge and does not provide information in other directions.

As observed in Figure 5.17, the relaxation induced by drilling did not result in a significant stress difference along the direction of the uniaxial strain gauge.

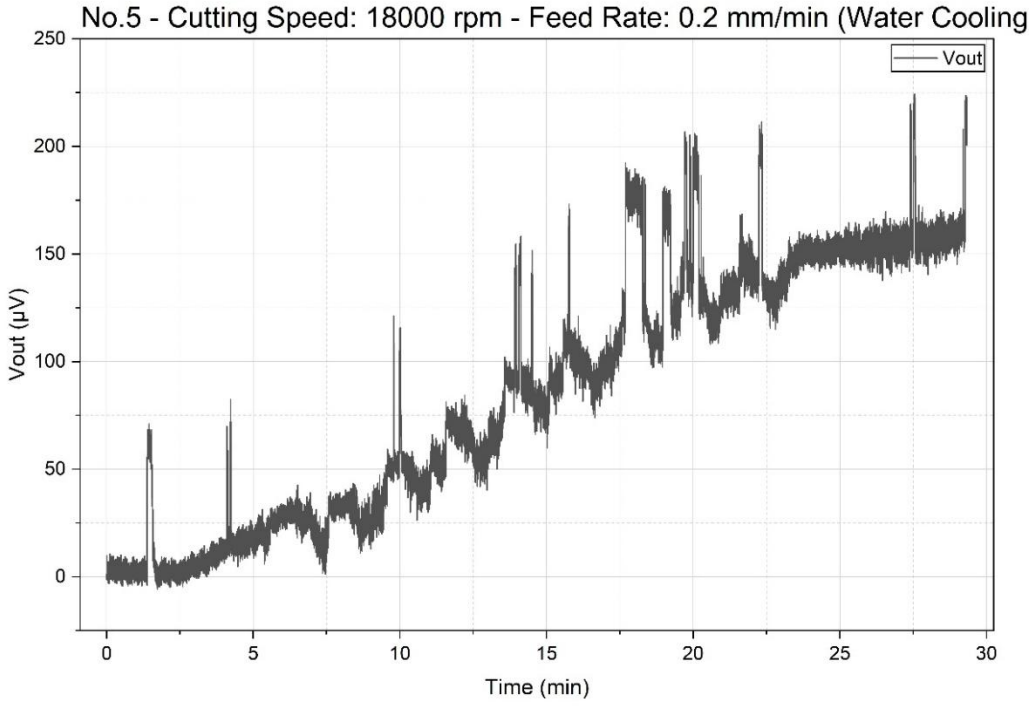

Figure 5.16 Gravity Specimen No.5 - Cutting Speed: 18000 rpm - Feed Rate: 0.2 mm/min

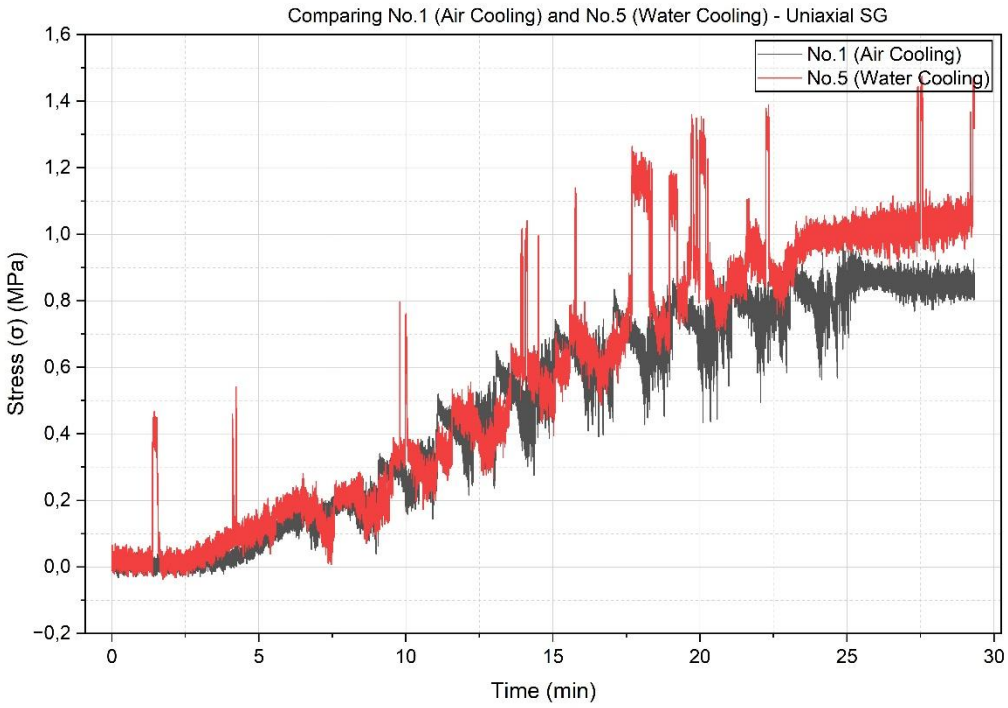

Figure 5.17 Comparing Gravity Specimen No.1 (Air Cooling)–No.5 (Water Cooling)–Uniaxial SG

In the subsequent step, in order to investigate whether any variations occurred in other directions, a Vishay CEA-06-120CZA-120 rosette strain gauge capable of measuring in three directions was applied to Gravity Specimens No. 6 and No. 7. Machining was then performed in a manner similar to the primary experimental setup, and the stress relaxation resulting from drilling was measured in three different channels corresponding to 0° (reference), 45°, and 90°, respectively. According to this configuration, measurements were taken from Channel 1 in the 0° direction, from Channel 2 in the 45° direction, and from Channel 3 in the 90° direction.

Based on these secondary experimental results, it can be concluded that, similar to the primary experimental setup, no significant stress differences were observed. This indicates that the rapid cooling process applied after casting (water cooling), without any subsequent heat treatment, does not produce a noticeable difference compared to air cooling. Moreover, this observation is valid not only along the direction of the uniaxial strain gauge but also for the rosette strain gauge measurements conducted at different orientations, which likewise exhibited low variations.

The important outcome here is that, using the data acquisition system employed in this study, strain differences can be successfully detected, and the stress relaxation induced by machining due to internal stresses within the structure can be measured through the resulting voltage variations.

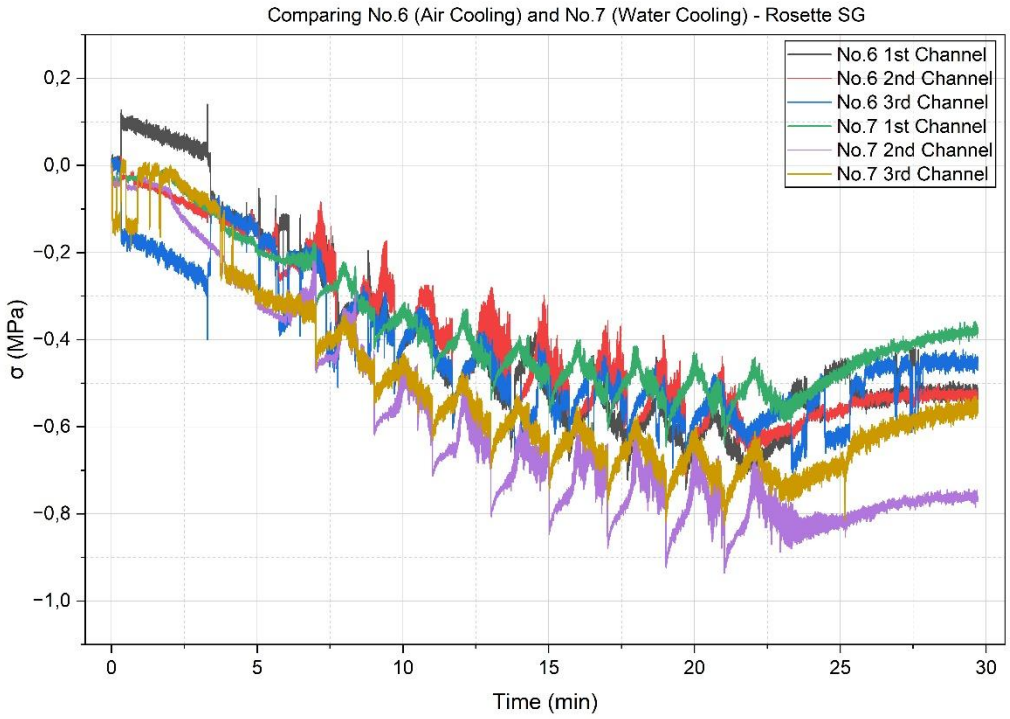

Figure 5.18 Comparing Gravity Specimen No.6 (Air Cooling)–No.7 (Water Cooling)–Rosette SG

The primary reasons for the low stress ranges obtained may be attributed to the geometrically simple shape of the specimen, which is a rectangular prism (37 mm × 140 mm × 7 mm), and its relatively small size, which does not allow for the development of significant temperature gradients during cooling. In addition, the absence of any heat treatment at the specimen scale (e.g., T6) and the lack of any cooling channel system in the casting mold, which would otherwise promote directional solidification during cooling and solidification, suggest that the resulting residual stress levels remain very low.

In the subsequent stage, since these factors differ for the low-pressure cast wheel specimens produced directly in an industrial environment, residual stress formation at different and higher levels is expected.

During the wheel measurements, Vishay CEA-06-062UM-120 rosette strain gauges, as defined in the relevant standard, were used. For measurements on the wheel specimens, the CEA-06-062UM-120 is classified as an ASTM Type B – 1/16 in rosette. According to ASTM E837-08 Table 1 (Rosette Dimensions) (ASTM, 2008), the gage circle diameter is D = 0.202 in = 5.13 mm. Considering the geometrical parameters of the drilled hole (hole diameter: D_0 = 1.5 mm, hole depth: h = 2 mm, gage circle diameter: D = 5.13 mm), the ratios h/D = 0.40 and D_0/D = 0.40 correspond to $\bar{a}$ = 0.203 and $\bar{b}$ = 0.541, as read from ASTM E837-08 Table 3 (ASTM, 2008). By incorporating the material properties (E = 70 GPa, ν = 0.33), the conversion from measured microvolts to strain, and from strain to stress, can be performed. In this step of the study, incremental hole drilling is carried out and the formulas provided in the standard (Equations 3.4 and 3.5) are applied.

The drilling process was carried out using the previously determined optimal feed rate of 0.2 mm/min, drilling the 2 mm deep hole in 10 incremental steps. Since the time corresponding to each step is known from the prepared CNC program, the step (hole depth) corresponding to each point in the graph can be determined. In summary, the V_{out} versus time graph can be converted into a residual stress versus depth profile for the specified increments. The experimental setup for the wheel specimens was applied to three wheels conditions: as-cast (Figure 4.2), T6 heat-treated (Figure 4.5), and artificially aged (Figure 4.6).

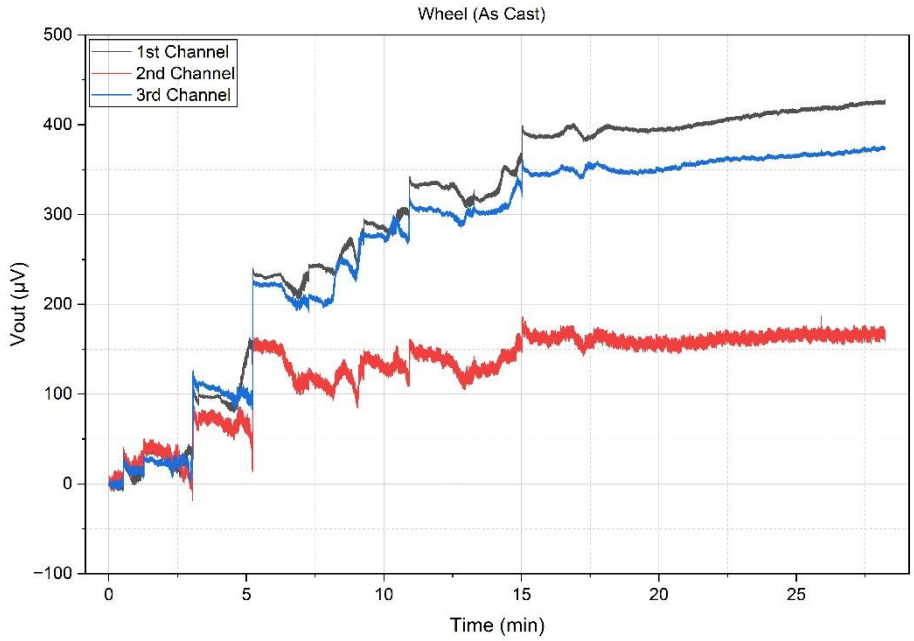

Figure 5.19 Vout / time for as cast wheel

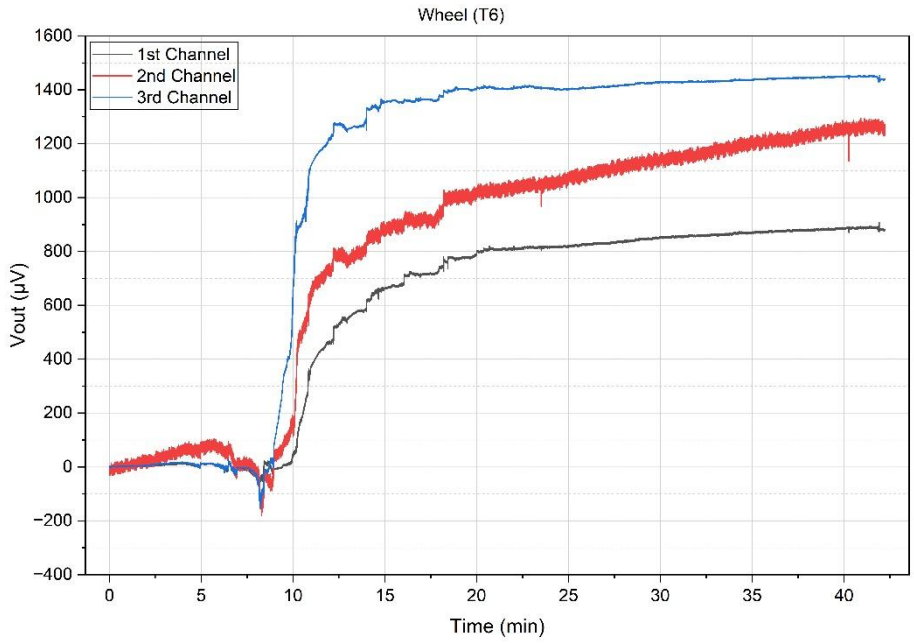

Figure 5.20 Vout / time for T6 wheel

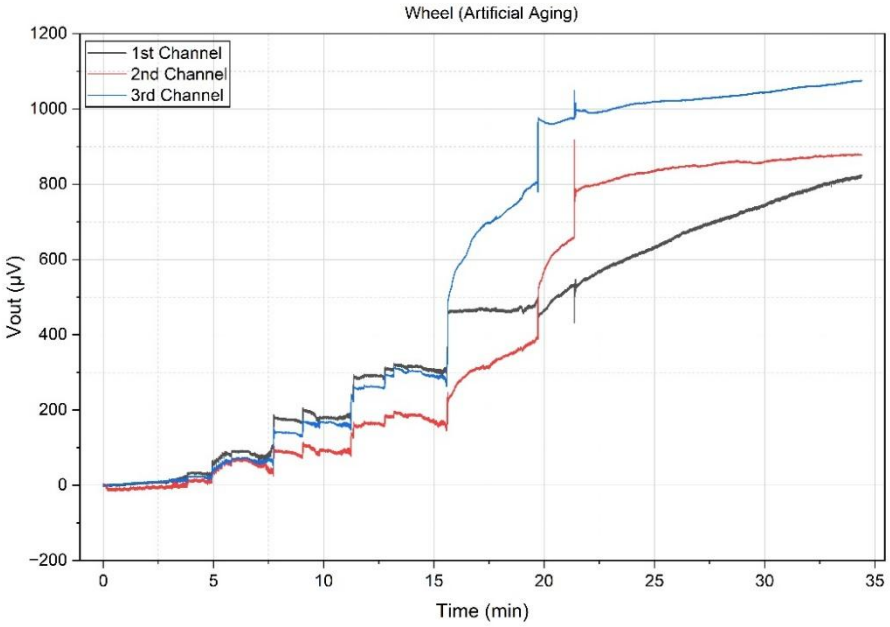

Figure 5.21 Vout / time for artificial aged wheel

At this stage of the study, the V_{out} versus time graphs (Figures 5.19–5.21) are presented first, followed by the residual stress versus depth graphs obtained after the previously mentioned calculations (Figures 5.22–5.24).

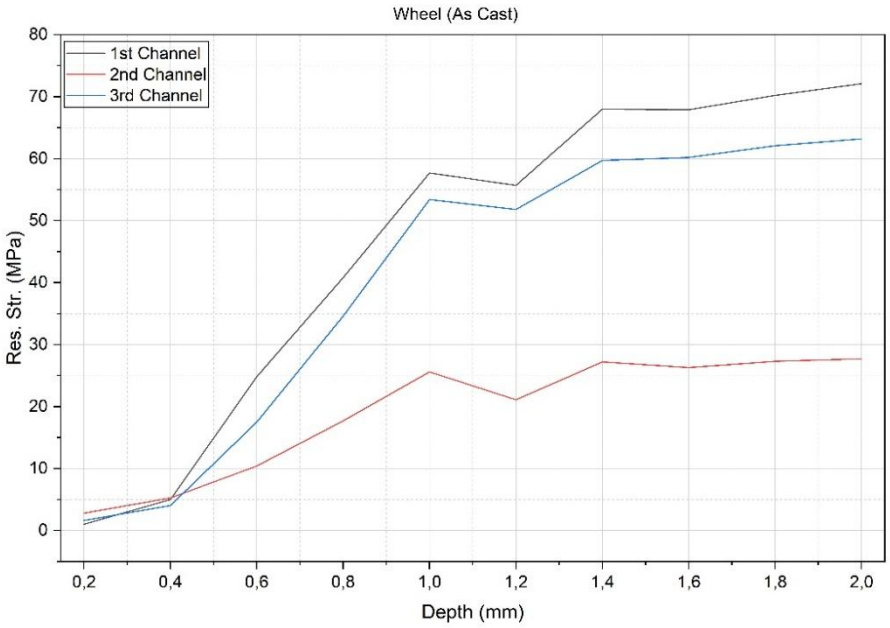

Figure 5.22 Residual Stress / depth for as cast wheel

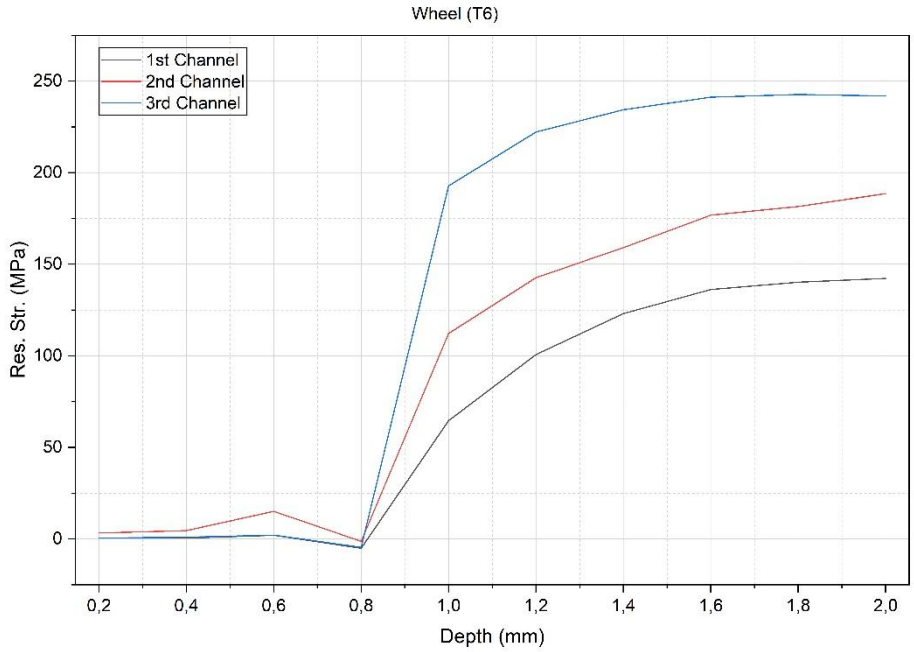

Figure 5.23 Residual Stress / depth for T6 wheel

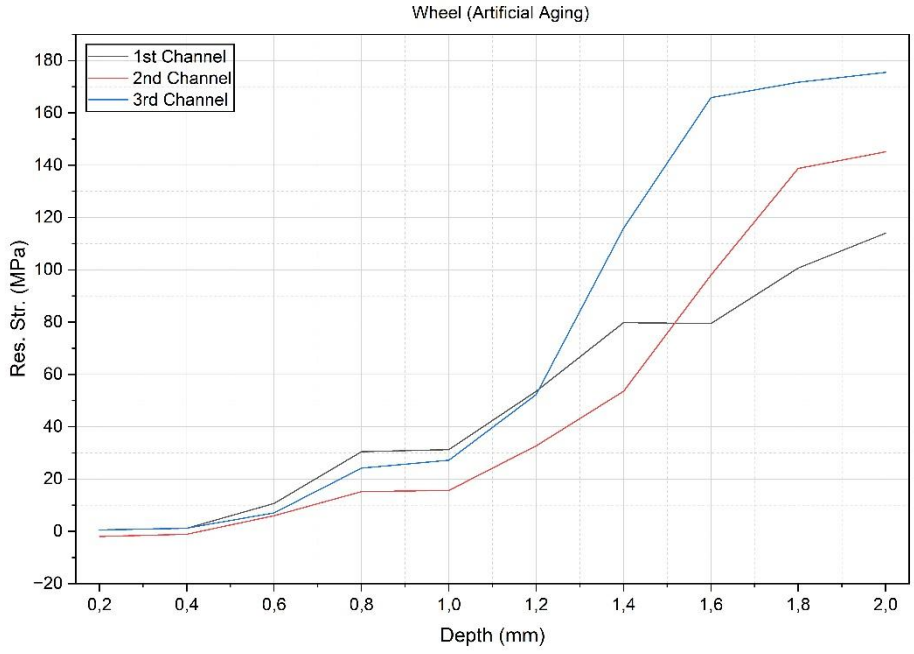

Figure 5.24 Residual Stress / depth for artificial aged wheel

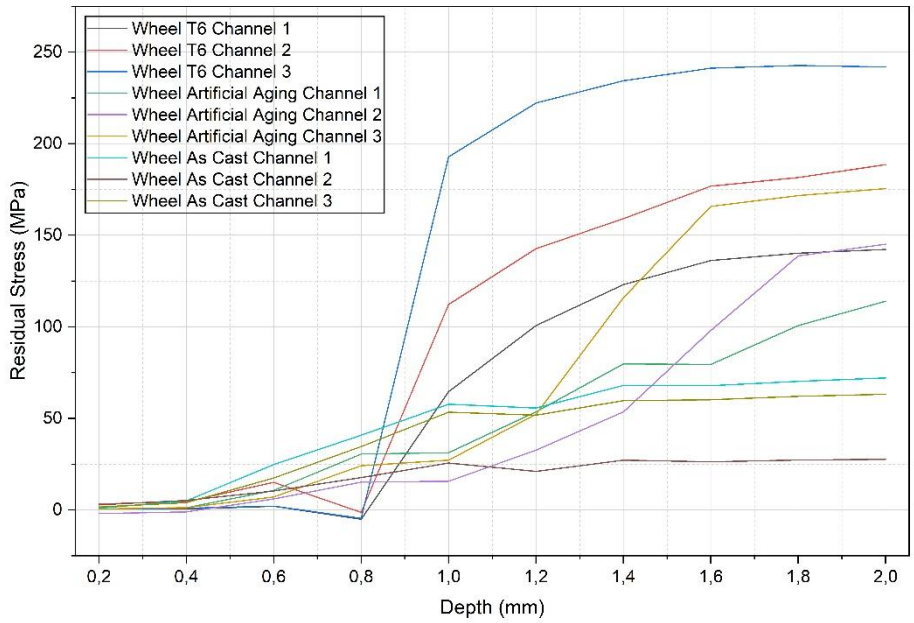

Figure 5.25 Comparing all wheels

In the last figure (Figure 5.25), the residual stress values for all wheel samples are compared. As can be observed from these comparisons, the highest residual stress values were measured in the T6 heat-treated wheel specimens. This outcome aligns well with the results and expectations presented in the "Analytical Method Results" section. Following the T6 heat-treated wheels, the next highest residual stress levels were observed in the wheels subjected to artificial aging. The residual stress measured after artificial aging was approximately 20–25% lower than that of the T6 heat-treated specimens. Finally, the as-cast wheel specimens, which were not subjected to any heat treatment, exhibited the lowest residual stress values. These values are more than 50% lower compared to the T6 heat-treated wheels.

In summary, the experimentally measured residual stress levels from highest to lowest were as follows: T6 heat-treated wheel specimens, artificially aged wheel specimens, and as-cast (non-heat-treated) wheel specimens. Prior to the measurements on the wheels, the gravity-cast preliminary specimens—also not subjected to heat treatment—exhibited almost negligible residual stresses. This confirms that the

primary factor contributing to residual stress development is the heat treatment process.

In contrast to the experimental results, the analytical study indicated the highest to lowest residual stress levels as follows: T6 heat-treated wheel specimens, as-cast wheel specimens, and artificially aged wheel specimens. While both approaches agree that T6 treatment generates the highest residual stresses in the material, the presence of moderate residual stresses in as-cast wheels in the analytical results—unlike in the experimental measurements—may be attributed to industrial process parameters introduced in the simulation, such as handling conditions, water temperature during quenching, and flow disturbances, which are difficult to precisely replicate in industrial settings.

CHAPTER SIX
CONCLUSIONS

This study systematically investigated the influence of casting and heat treatment processes on the microstructure, mechanical performance, and residual stress development in AlSi11Mg aluminum alloy wheels produced via low-pressure die casting (LPDC). The motivation for this work originated from the need to optimize wheel production processes to ensure mechanical reliability, minimize residual stress-induced failures, and achieve material properties suitable for automotive applications.

The objectives of this study:

- Characterize the chemical composition, macrostructure, and microstructure of AlSi11Mg alloy wheels.
- Investigate the effects of various heat treatment processes, including T6 treatment and artificial aging, on mechanical properties.
- Quantify and analyze residual stress development under different processing conditions using both numerical simulations and experimental techniques.

Chapter 3 (Materials and Methods) detailed the material selection, casting procedures, and experimental protocols, including chemical analysis, macro- and microstructural evaluations, mechanical testing, and residual stress measurement methods.

Chapter 4 (Experimental Study) provided the experimental design, outlining the material characterization, heat treatment schedules, and residual stress calculation and measurement approaches. Both analytical (Magmastress module of Magmasoft) and experimental (hole drilling method with uniaxial and rosette strain gauges) techniques were employed to ensure accurate and comprehensive evaluation of residual stress evolution.

The chemical analysis confirmed that the AlSi11Mg alloy composition met standard and industrial specifications, providing a reliable foundation for mechanical performance. Macrostructural evaluation indicated uniform grain distribution, while

microstructural observations revealed a transition from coarse dendritic structures in as-cast wheels to refined and spheroidized silicon particles in T6-treated specimens. Options #2, #3, and #4, representing different artificial aging durations, exhibited improved microstructural homogeneity and reduced structural heterogeneity, directly impacting mechanical performance.

Mechanical testing demonstrated that as-cast wheels (Option #1) had the lowest ultimate tensile strength (UTS), yield strength (YS), and Brinell hardness, correlating with their coarse dendritic microstructure. Wheels subjected to partial artificial aging (Option #5) showed moderate improvement, while T6-treated wheels (Options #2–#4) displayed significant enhancements in strength and hardness. Among these, Option #3 (120 min artificial aging) provided the most balanced combination of UTS, YS, elongation, and hardness across the inner flange, outer flange, and spoke regions, highlighting the critical role of aging time in optimizing mechanical properties.

Residual stress assessment revealed that as-cast wheels exhibited low-to-moderate stress levels, largely influenced by handling during production. T6-treated wheels experienced higher residual stresses following quenching due to steep thermal gradients, which were partially relieved during artificial aging. Option #2, with the longest aging duration (150 min), achieved the lowest residual stresses in the hub and hub–spoke regions, with an average reduction of approximately 5–6% relative to post-quenching values.

Experimental hole drilling results corroborated these trends, confirming that residual stresses were highest in T6-treated wheels, followed by artificially aged and as-cast wheels. The spoke region consistently showed lower tensile strength and higher vulnerability to residual stress effects, emphasizing its critical role in wheel integrity.

Comparison of analytical and experimental results demonstrated strong agreement regarding the ranking of residual stress levels and the influence of heat treatment. T6-treated wheels consistently exhibited superior mechanical performance while simultaneously presenting higher residual stresses, which could be effectively mitigated by optimized artificial aging or stress-relief annealing.

The study establishes a clear link between casting parameters, heat treatment schedules, microstructural evolution, mechanical properties, and residual stress development. Key insights include:

1. Optimal Heat Treatment Strategy: T6 solution treatment followed by 120–150 minutes of artificial aging (Options #2 and #3) achieves the best balance of mechanical performance and residual stress minimization.
2. Critical Region Focus: The hub and spoke areas require special attention due to their susceptibility to stress accumulation and potential cracking.
3. Residual Stress Management: Extended aging or stress-relief annealing effectively reduces residual stresses, enhancing long-term durability.
4. Quality Control: Ensuring compliance with chemical composition specifications and maintaining uniform casting and heat treatment practices are essential for reliable wheel performance.

These findings provide actionable guidance for industrial wheel production, contributing to improved safety, performance, and service life.

While comprehensive, the study has several limitations:

- Only a single wheel design and LPDC process were examined; results may vary for other geometries or casting methods.
- Residual stress measurements were localized; full-field 3D mapping could provide more complete understanding.
- Industrial handling and production variations were partially simulated, leaving some uncertainty regarding real-world process effects.

Future research could expand upon this study in several ways:

1. Alternative Geometries and Alloys: Investigate wheels of different designs or alternative Al-Si-Mg alloys to generalize findings.
2. Advanced Residual Stress Mapping: Employ non-destructive methods such as X-ray or neutron diffraction for full-field stress characterization.
3. Predictive Modeling: Develop integrated simulation models linking casting, heat treatment, and mechanical performance for process optimization.
4. Service Performance Evaluation: Examine fatigue life, crack initiation, and long-term behavior under operational conditions.
5. Environmental and Thermal Effects: Study the impact of temperature cycles and external loading on residual stress evolution and mechanical properties.

In summary, this research provides a comprehensive understanding of how casting and heat treatment influence the microstructure, mechanical performance, and residual stresses of AlSi11Mg aluminum wheels. T6 treatment, when properly optimized, enhances mechanical properties while residual stress management strategies ensure structural reliability. The study contributes both to the academic knowledge base and to practical industrial applications, offering guidance for safer and more durable wheel production. Future work will continue to refine these insights and broaden their applicability across the automotive sector.

REFERENCES

Abdelaziz, M. H., Samuel, A. M., Doty, H. W., Valtierra, S., & Samuel, F. H. (2019). Effect of additives on the microstructure and tensile properties of Al–Si alloys. *Journal of Materials Research and Technology*, *8*(2), 2255–2268. https://doi.org/10.1016/j.jmrt.2019.03.003

Akbari, S., Taheri-Behrooz, F., & Shokrieh, M. M. (2014). Characterization of residual stresses in a thin-walled filament wound carbon/epoxy ring using incremental hole drilling method. *Composites Science and Technology*, *94*, 8–15. https://doi.org/10.1016/j.compscitech.2014.01.008

Akdeniz, Y. (2012). *Taşlama sonrası kalın camsı metalde oluşan kalıntı gerilmenin delik delme yöntemiyle incelenmesi* [Master's thesis]. İstanbul Teknik Üniversitesi.

Al Circle. (2023). *Future of aluminium in transportation sector: An industry analysis with forecasts to 2027*. https://www.alcircle.com/specialreport/1336/future-of-aluminium-in-transportation-sector-an-industry-analysis-with-forecasts-to-2027

Alipooramirabad, H., Kianfar, S., Paradowska, A., & Ghomashchi, R. (2024). Residual stress measurement in engine block—an overview. In *International Journal of Advanced Manufacturing Technology* (Vol. 131, Issue 1, pp. 1–27). Springer Science and Business Media Deutschland GmbH. https://doi.org/10.1007/s00170-024-13071-3

Al-Olabi, G. A. (1994). *Residual stresses and heat treatments for metallic welded components* [Doctoral dissertation]. Dublin City University.

Altınel, A. İ. (1999). *The mechanical properties of some cast aluminium alloys (Sr modified AlSi11Mg)* [Master's thesis]. Dokuz Eylül University.

Alzyod, H., & Ficzere, P. (2022). Using the photostress method to determine the residual stresses. *International Journal of Engineering and Management Sciences (IJEMS)*, *7*(2). https://doi.org/10.21791/IJEMS.2022.2.2

Arabul, E., & Lunt, A. J. G. (2022). A novel low-cost DIC-based residual stress measurement device. *Applied Sciences*, *12*(14). https://doi.org/10.3390/app12147233

Ashkenazi, D. (2019). How aluminum changed the world: A metallurgical revolution through technological and cultural perspectives. *Technological Forecasting and Social Change*, *143*, 101–113. https://doi.org/10.1016/j.techfore.2019.03.011

Askeland, D. R., Fulay, P. P., & Wright, W. J. (2011). *The science and engineering of materials* (6th ed.). Cencage Learning.

ASTM. (2008). *E 837 – 08 Standard Test Method for Determining Residual Stresses by the Hole-Drilling Strain-Gage Method*. www.astm.org,

ASTM. (2020). *E837 − 20 standard test method for determining residual stresses by the hole-drilling strain-gage method* (pp. 1–7). ASTM International. https://doi.org/10.1520/E0837-20

Aydın, Y. N., Özaydın, O., & Akış, A. (2021). Static Analysis of the Slotted Upper Plate of Low Pressure Casting Machine. *Celal Bayar University Journal of Science*, *17*(1), 35–41. https://doi.org/10.18466/cbayarfbe

Baldi, A. (2016). Using optical interferometry to restart the ring-core method. *Experimental Mechanics*, *56*(7), 1191–1202. https://doi.org/10.1007/s11340-016-0163-0

Beder, M., Akçay, S. B., Varol, T., & Çuvalcı, H. (2024). The effect of heat treatment on the mechanical properties and oxidation resistance of AlSi10Mg alloy. *Arabian Journal for Science and Engineering*, *49*(11), 15335–15346. https://doi.org/10.1007/s13369-024-08971-1

Belte, A. G. (n.d.). *Einfluss der Wärmebehandlung auf die Betriebsfestigkeit von Zylinderköpfen*. Retrieved December 3, 2025, from http://www.belte-ag.de/download/symlink/Fachvortrag_Magdeburg_06.02.2007.pdf

Brown, D. W., Holden, T. M., Clausen, B., Prime, M. B., Sisneros, T. A., Swenson, H., & Vaja, J. (2011). Critical comparison of two independent measurements of

residual stress in an electron-beam welded uranium cylinder: Neutron diffraction and the contour method. *Acta Materialia*, *59*(3), 864–873. https://doi.org/10.1016/j.actamat.2010.09.022

Brown, J. R. (1999). *Foseco non-ferrous foundryman's handbook* (11th ed.). Butterworth-Heinemann.

Buffington, J. (2012). The beverage can in the United States: Achieving a 100% recycled aluminum can through supply chain innovation. *JOM*, *64*(8), 923–932. https://doi.org/10.1007/s11837-012-0381-6

Cai, Z., Mayr, P., Fernandez, R., Robbe, S., Usmial, E., Lefebvre, F., To, L., Schajer, G. S., Withers, P. J., & Roy, M. J. (2024). Residual stress determination of cast aluminium benchmark components using strain relief techniques. *Experimental Mechanics*, *64*(3), 441–452. https://doi.org/10.1007/s11340-024-01033-5

Campbell, J. (2011). *Complete casting handbook: Metal casting processes, metallurgy, techniques and design* (1st ed.). Elsevier.

Carrera, E., Rodríguez, A., Talamantes, J., Valtierra, S., & Colás, R. (2007). Measurement of residual stresses in cast aluminium engine blocks. *Journal of Materials Processing Technology*, *189*(1–3), 206–210. https://doi.org/10.1016/j.jmatprotec.2007.01.023

Cione, F. C., Rossi, J. L., Souza, A. C., Delijaicov, S., & Colosio, M. A. (2012). Residual stresses measurements using strain gages: Aluminum wheels. *Materials Science Forum*, *727–728*, 1925–1930. https://doi.org/10.4028/www.scientific.net/MSF.727-728.1925

Cione, F. C., Souza, A., Martinez, L., Rossi, J., Betini, E. G., Rola, F., & Colosio, M. A. (2016). Measurements of residual stresses in aluminum wheels using the techniques of XRD, strain gages and FEA simulation: A comparison. *Int. J. Mater. Manf.*, *9*(3). https://doi.org/10.4271/2016-01-0426

Cullity, B. D., & Stock, S. R. (2014). *Elements of X-Ray Diffraction* (3rd ed.). Pearson Education Limited.

Dahle, A. K., Tondel, P. A., Paradies, C. J., & Arnberg, L. (1996). Effect of grain refinement on the fluidity of two commercial Al-Si foundry alloys. *Metallurgical And Materials Transactions A*, *27A*, 2305–2313.

Davis, J. R. (2001). *Alloying: Understanding the basics – Aluminum and aluminum alloys*. ASM International. https://doi.org/10.1361/autb2001p351

Dege, B. (2013). *TiN ince filmlerde bias voltajına bağlı olarak kalıntı gerilme değişiminin incelenmesi* [Master's thesis]. İstanbul Teknik Üniversitesi.

Demir, C., Menteşe, B., & Togay, M. A. (2007). *Alüminyum ısıl işleminde su verme uygulamaları ve kalıntı gerilime etkisi*.

Dieter, G. E. Jr. (1961). *Mechanical Metallurgy* (R. F. Mehl & M. B. Bever, Eds.). McGraw-Hill Education.

Duan, J. (2016). *Development of a numerical optimization methodology for the aluminum alloy wheel casting process* [Doctoral dissertation, University of British Columbia]. https://doi.org/10.14288/1.0300014

Duygun, İ. K. (2017). *Al–Si alaşımlarında stronsiyum modifikasyonu ile döküm kalitesi arasındaki ilişkinin karakterizasyonu* [Master's thesis]. İstanbul Üniversitesi.

ECCS. (2015). *The European Convention for Constructional Steelwork: History and achievements 1955–2015*. www.steelconstruct.com

Ekmekçi, B. (2004). *Theoretical and experimental investigation of residual stresses in electric discharge machining* [Doctoral dissertation]. Middle East Technical University.

Elmahti, Ü., Kaya, A. Y., Özaydın, O., & Yayla, P. (2023). Impact test analysis of aluminum alloy wheels under different temperature. *International Journal of Metalcasting*, *17*(2), 1129–1138. https://doi.org/10.1007/s40962-022-00845-2

European Aluminium Association. (2011). *Applications – chassis & suspension – wheels*.

Flaman, M. T. (1982). Brief investigation of induced drilling stresses in the center-hole method of residual-stress measurement. *Experimental Mechanics*, *22*, 26–30. https://doi.org/10.1007/BF02325700

Ghasemi, A. R., Taheri-Behrooz, F., & Shokrieh, M. M. (2014). Determination of non-uniform residual stresses in laminated composites using integral hole drilling method: Experimental evaluation. *Journal of Composite Materials*, *48*(4), 415–425. https://doi.org/10.1177/0021998312473858

Gökelma, M., Önen Tüzgel, R., Kaya, A. Y., & Özaydın, O. (2023). A study on recyclability of AlSi7Mg0.3 machining waste. *Black Sea Journal of Engineering and Science*, *6*(3), 240–244. https://doi.org/10.34248/bsengineering.1282159

Grand Review Research. (n.d.). *Alloy wheels market (2025 - 2033)*. Retrieved December 5, 2025, from https://www.grandviewresearch.com/industry-analysis/alloy-wheels-market-report

Grubisic, V. (2017). Air Tightness Control of Passenger Car Wheels. *Engineering*, *09*(02), 171–180. https://doi.org/10.4236/eng.2017.92008

Guo, J., Fu, H., Pan, B., & Kang, R. (2021). Recent progress of residual stress measurement methods: A review. *Chinese Journal of Aeronautics*, *34*(2), 54–78. https://doi.org/10.1016/j.cja.2019.10.010

Gupta, M. K., & Singhal, V. (2022). Review on materials for making lightweight vehicles. *Materials Today: Proceedings*, *56*, 868–872. https://doi.org/10.1016/j.matpr.2022.02.517

Güven, O. (2005). *Alüminyum silisyum magnezyum döküm alaşımlarının yapı incelemesi* [Master's thesis]. İstanbul Teknik Üniversitesi.

Hacini, L., Van Lê, N., & Bocher, P. (2009). Evaluation of residual stresses induced by robotized hammer peening by the contour method. *Experimental Mechanics*, *49*(6), 775–783. https://doi.org/10.1007/s11340-008-9205-6

Heger, J., Hartmann, G., & Bodenburg, M. (2019). Integration of manufacturing aspects into the development of heavy-duty engine cast components. In Wolfgang

Siebenpfeiffer (Ed.), *Heavy-Duty-, On- und Off-Highway-Motoren 2018* (pp. 225–237). Springer. https://doi.org/10.1007/978-3-658-25889-4_14

Hibbeler, R. C. (2014). *Mechanics of Materials* (Ninth). Pearson.

Hosseinzadeh, F., Hossain, S., Truman, C. E., & Smith, D. J. (2014). Measurement and prediction of residual stresses in quenched stainless steel components. *Experimental Mechanics*, *54*(7), 1151–1162. https://doi.org/10.1007/s11340-014-9890-2

Işık, S. B., Zeren, M., & Atamay, K. (2020). Simulation of Aluminum Alloy Automobile Wheel Production by High Pressure Die Casting. *Kocaeli Üniversitesi Fen Bilimleri Dergisi*, *3*(1), 125–132. http://dergipark.gov.tr/koufbd

Jarco, A. (2017). Effect of soft annealing treatment on impact strength and hardness of the EN AC-AlSi11 alloy. *Archives of Foundry Engineering*, *17*(3), 55–58. https://doi.org/10.1515/afe-2017-0090

Jarco, A., & Pezda, J. (2021). Effect of heat treatment process and optimization of its parameters on mechanical properties and microstructure of the AlSi11(Fe) alloy. *Materials*, *14*(9). https://doi.org/10.3390/ma14092391

Javadi, Y., Akhlaghi, M., & Najafabadi, M. A. (2013). Using finite element and ultrasonic method to evaluate welding longitudinal residual stress through the thickness in austenitic stainless steel plates. *Materials and Design*, *45*, 628–642. https://doi.org/10.1016/j.matdes.2012.09.038

Jiang, Q., Zhao, Z., Xu, Z., Sun, J., Chen, X., Su, B., Zhao, Z., & Jiang, W. (2022). Effect of residual stresses on wheel fatigue life and experimental validation. *Machines*, *10*(10). https://doi.org/10.3390/machines10100924

Johnson, E. M., Watkins, T. R., Schmidlin, J. E., & Dutler, S. A. (2012). A benchmark study on casting residual stress. *Metallurgical and Materials Transactions A: Physical Metallurgy and Materials Science*, *43*(5), 1487–1496. https://doi.org/10.1007/s11661-011-0907-5

Kandil, F. A., Lord, J. D., Fry, A. T., & Grant, P. V. (2001). *A review of residual stress measurement methods: A guide to technique selection*.

Karabulut, C., Malkoç, G., Kaya, A. Y., Özaydın, O., & Yayla, P. (2024). Influence of different Fe levels on mechanical properties of AlSi7Mg0.3 aluminum casting alloys. *International Journal of Metalcasting*, *18*(4), 3081–3094. https://doi.org/10.1007/s40962-023-01227-y

Kaufman, J. G. (2000). *Introduction to aluminum alloys and tempers*. ASM International. https://doi.org/10.1361/iaat2000p023

Kaufman, J. G., & Rooy, E. L. (2004). Aluminum Alloy Castings: Properties, Processes, and Applications. In *Aluminum Alloy Castings: Properties, Processes, and Applications* (pp. 1–6). https://doi.org/https://doi.org/10.31399/asm.tb.aacppa.t51140001

Kaya, A. Y. (2024). *The effects of manganese concentration on the mechanical properties of A356 aluminum alloy wheels produced by low pressure die casting* [Master's thesis]. İzmir Institute of Technology.

Kaya, A. Y., Özaydın, O., Dokumacı, E., & Armakan, E. (2019). Farklı döküm aşamalarındaki sıvı metal akışkanlığının incelenmesi. *2nd National Foundry Congress by Tudoksad Academy*, 215–221.

Kaya, A. Y., Özaydın, O., Yagci, T., Korkmaz, A., Armakan, E., & Culha, O. (2021). Effect of chip amount on microstructural and mechanical properties of A356 aluminum casting alloy. *Archives of Foundry Engineering*, *21*(3), 19–26. https://doi.org/10.24425/afe.2021.136108

Kempen, K., Thijs, L., Van Humbeeck, J., & Kruth, J. P. (2012). Mechanical properties of AlSi10Mg produced by selective laser melting. *Physics Procedia*, *39*, 439–446. https://doi.org/10.1016/j.phpro.2012.10.059

Khan, M. A. A., & Sheikh, A. K. (2018). A comparative study of simulation software for modelling metal casting processes. *International Journal of Simulation Modelling*, *17*(2), 197–209. https://doi.org/10.2507/IJSIMM17(2)402

Kim, Y. H., Ryou, T. K., Choi, H. J., & Hwang, B. B. (2002). An analysis of the forging processes for 6061 aluminum-alloy wheels. *Journal of Materials Processing Technology*, *123*, 270–276.

Kip, M., Gören, A., Korkut, T. B., & Özaydın, O. (2025). Design and manufacturing modifications in rear swing arm of solar-powered electric vehicle. *Australian Journal of Mechanical Engineering*, 1. https://doi.org/10.1080/14484846.2025.2498862

Kırmızıgöl, S. F., Özaydın, O., & Acarer, S. (2024). Improving heat transfer and compressed air consumption in low pressure die casting of aluminum wheels. *Applied Thermal Engineering*, *251*. https://doi.org/10.1016/j.applthermaleng.2024.123598

Kutsal, U., Arslan, Y., Özaydın, O., Akyildiz, Y., Kaya, A. Y., & Ertugrul, O. (2024). Heat treatment simulation of aluminum alloy wheels and investigation of process steps. *International Journal of Metalcasting*, *18*(2), 1556–1572. https://doi.org/10.1007/s40962-023-01132-4

Li, K., Xiao, B., & Wang, Q. (2008). Residual stresses in as-quenched aluminum castings. *International Journal of Materials and Manufacturing*, *1*(1), 725–731. https://doi.org/10.2307/26282709

Li, P., Maijer, D. M., Lindley, T. C., & Lee, P. D. (2007a). A through process model of the impact of in-service loading, residual stress, and microstructure on the final fatigue life of an A356 automotive wheel. *Materials Science and Engineering: A*, *460–461*, 20–30. https://doi.org/10.1016/j.msea.2007.01.076

Li, P., Maijer, D. M., Lindley, T. C., & Lee, P. D. (2007b). Simulating the residual stress in an A356 automotive wheel and its impact on fatigue life. *Metallurgical and Materials Transactions B: Process Metallurgy and Materials Processing Science*, *38*(4), 505–515. https://doi.org/10.1007/s11663-007-9050-5

Li, X., Liu, J., Wu, H., Miao, K., Wu, H., Li, R., Liu, C., Fang, W., & Fan, G. (2024). Research progress of residual stress measurement methods. *Heliyon*, *10*(7). https://doi.org/10.1016/j.heliyon.2024.e28348

Lipiński, T., & Szabracki, P. (2015). Mechanical properties of AlSi9Mg alloy with a sodium modifier. *Solid State Phenomena*, *223*, 78–86. https://doi.org/10.4028/www.scientific.net/SSP.223.78

Long, A., Thornhill, D., Armstrong, C., & Watson, D. (2013). Stress correlation between instrumentation and simulation analysis of the die for high pressure die casting. *International Journal of Metalcasting*, *7*(7), 27–41.

Macherauch, E. (1987). Introduction to residual stress. *Advances in Surface Treatments*, *4*, 1–35.

Magmasoft. (2015). *MAGMAwheel module simulation of wheel casting*. MAGMA Gießereitechnologie GmbH.

Magnier, A., Scholtes, B., & Niendorf, T. (2017). Analysis of residual stress profiles in plastic materials using the hole drilling method – Influence factors and practical aspects. *Polymer Testing*, *59*, 29–37. https://doi.org/10.1016/j.polymertesting.2016.12.025

Mantle, A. L., & Aspinwall, D. K. (2001). Surface integrity of a high speed milled gamma titanium aluminide. *Journal of Materials Processing Technology*, *118*, 143–150.

Masláková, K., Trebuňa, F., Frankovský, P., & Binda, M. (2012). Applications of the strain gauge for determination of residual stresses using ring-core method. *Procedia Engineering*, *48*, 396–401. https://doi.org/10.1016/j.proeng.2012.09.531

Mazzolani, F. M. (2004). Competing issues for aluminium alloys in structural engineering. *Progress in Structural Engineering and Materials*, *6*(4), 185–196. https://doi.org/10.1002/pse.178

Menne, R. J., Weiss, U., Brohmer, A., Egner-Walter, A., Weber, M., & Oelling, P. (2007). Implementation of casting simulation for increased engine performance and reduced development time and costs: Selected examples from FORD R&D engine projects. *28. Internationales Wiener Motorensymposium*.

Menteşe, E. B., Aydoğan, F., & Saklakoğlu, N. (2019). AlSi10Mg alaşımlı döküm parçalar için ısıl işlem prosesinde optimizasyon çalışmaları. *2. Ulusal Döküm Kongresi*, 223–231.

Neuser, M., Grydin, O., Frolov, Y., & Schaper, M. (2022). Influence of solidification rates and heat treatment on the mechanical performance and joinability of the cast aluminium alloy AlSi10Mg. *Production Engineering*, *16*(2–3), 193–202. https://doi.org/10.1007/s11740-022-01106-1

Olson, M. D., DeWald, A. T., & Hill, M. R. (2022). Measurement layout for residual stress mapping using slitting. *Experimental Mechanics*, *62*(3), 393–402. https://doi.org/10.1007/s11340-021-00791-w

Özaydın, O. (2019). *Alternatif alaşımlı jant malzemesi ile mekanik özellikleri iyileştirilmiş ürün geliştirilmesi* [Master's thesis]. İstanbul Teknik Üniversitesi.

Özaydın, O. (2022). Analysis of the stress-relief heat treatment of aluminium alloy wheels. *27th IFHTSE Congress & European Conference on Heat Treatment 2022*, 34–40.

Özaydın, O., Armakan, E., & Kaya, A. (2018). The Mechanical Properties of Sr Modification on Aluminium Casting Alloys. *ICETI 2nd International Conference on Environmental Technology and Innovations*.

Özaydın, O., Armakan, E., Kaya, A. Y., & Gören, A. (2019). Yapay yaşlandırma şartlarının jantın darbe özelliklerine etkisi. *2nd National Foundry Congress by Tudoksad Academy*, 371–377.

Özaydın, O., & Çatal, Y. (2019a). Evaluation of cooling channel design and coolants of an aluminium alloy wheel mold using casting simulation. *ICENS 5th International Conference on Engineering and Natural Sciences*.

Özaydın, O., & Çatal, Y. (2019b). Examination of the effects of heat treatment shape distortion on aluminium alloy wheels using FEA. *5th International Conference on Engineering and Natural Sciences*.

Özaydın, O., Çatal, Y., & Kaya, A. Y. (2022). Design and analysis of various cooling conditions of an aluminium wheel mold. *La Metallurgia Italiana*, 56–60. https://doi.org/10.36146/2022_03_56

Özaydın, O., & Dikicioğlu, A. (2023). Product development of alternative alloy wheel material with improved mechanical properties. *International Journal of Metalcasting*, *17*(3), 2085–2102. https://doi.org/10.1007/s40962-022-00914-6

Özaydın, O., Dokumaci, E., Armakan, E., & Kaya, A. (2019). The effects of artificial ageing conditions on A356 aluminum cast alloys. *ECHT Heat Treatment and Surface Engineering for Automotive*, 1–10.

Özaydın, O., Gören, A., Dokumacı, E., & Gençer, G. M. (2025). İnceleme: Döküm Alüminyum Alaşımlarında Kalıntı Gerilme Ölçüm Yöntemleri, Nedenleri ve Önleme Çalışmaları. *Dicle Üniversitesi Mühendislik Fakültesi Mühendislik Dergisi*, *16*(4), 983–999. https://doi.org/10.24012/dumf.1697102

Özaydın, O., & Kaya, A. (2019). Influence of different Si levels on mechanical properties of aluminium casting alloys. *European Journal of Engineering and Natural Sciences*, *3*(2), 165–172.

Özaydın, O., Kaya, A., Armakan, E., Yağcı, T., & Çulha, O. (2019). Investigation and characterisation of inclusions in aluminium cast alloys for the automotive industry. *Foundry Trade Journal*, 340–343.

Özaydın, O., Kaya, Y., & Dışpınar, D. (2021). Effect of Li additions and holding time on the mechanical properties of the AlSi9Mg alloys. *International Journal of the Italian Association for Metallurgy*, *113*, 19–24. https://doi.org/10.36146/2021_11_19

Pedersen, L., & Arnberg, L. (2001). The effect of solution heat treatment and quenching rates on mechanical properties and microstructures in AlSiMg foundry alloys. *Metallurgical And Materials Transactions A*, *32A*, 525–532.

Pezda, J. (2022). Optimization of heat treatment parameters of AlSi7Mg alloy. *Materials*, *15*(3). https://doi.org/10.3390/ma15031163

Polmear, I. (2006). *Light alloys from traditional alloys to nanocrystals* (4th ed.). Elsevier.

Prime, M. B. (2001). Cross-sectional mapping of residual stresses by measuring the surface contour after a cut. *Journal of Engineering Materials and Technology*, *123*(2), 162–168. https://doi.org/10.1115/1.1345526

Ramana, P. V., Madhusudhan Reddy, G., Mohandas, T., & Gupta, A. V. S. S. K. S. (2010). Microstructure and residual stress distribution of similar and dissimilar electron beam welds - Maraging steel to medium alloy medium carbon steel. *Materials and Design*, *31*(2), 749–760. https://doi.org/10.1016/j.matdes.2009.08.007

Reid, R. G., & Paskaramoorthy, R. (2009). A novel method to measure residual stresses in unidirectional GFRP. *Composite Structures*, *8*(3), 388–393. https://doi.org/10.1016/j.compstruct.2008.04.015

Rheinfelden Alloys, G. (2016). *Primary aluminum casting alloys*. https://rheinfelden-alloys.eu/wp-content/uploads/2017/01/Handbook-Primary-Aluminium-Casting-Alloys_RHEINFELDEN-ALLOYS_2016_EN.pdf

Rigdahl, M. (2006). Calculation of residual thermal stresses in injection molded amorphous polymers by the finite element method. *International Journal of Polymeric Materials and Polymeric Biomaterials*, *5*((1–2)), 43–57. https://doi.org/https://doi.org/10.1080/00914037608072388

Robinson, J. S., & Redington, W. (2015). The influence of alloy composition on residual stresses in heat treated aluminium alloys. *Materials Characterization*, *105*, 47–55. https://doi.org/10.1016/j.matchar.2015.04.017

Rossini, N. S., Dassisti, M., Benyounis, K. Y., & Olabi, A. G. (2012). Methods of measuring residual stresses in components. *Materials and Design*, *35*, 572–588. https://doi.org/10.1016/j.matdes.2011.08.022

Sanders, R. E. (2001). Technology innovation in aluminum products. *JOM*, *53*, 21–25. https://doi.org/https://doi.org/10.1007/s11837-001-0115-7

Scafidi, M., Valentini, E., & Zuccarello, B. (2011). Error and uncertainty analysis of the residual stresses computed by using the hole drilling method. *Strain*, *47*(4), 301–312. https://doi.org/10.1111/j.1475-1305.2009.00688.x

Schajer, G. S. (2010). Relaxation methods for measuring residual stresses: Techniques and opportunities. *Experimental Mechanics*, *50*, 1117–1127. https://doi.org/10.1007/s11340-010-9386-7

Shokrieh, M. M., & Ghasemi K., A. R. (2007). Determination of calibration factors of the hole drilling method for orthotropic composites using an exact solution. *Journal of Composite Materials*, *41*(19), 2293–2311. https://doi.org/10.1177/0021998307075443

Sigworth, G. K., & Kuhn, T. A. (2007). Grain Refienement of Aluminum Casting Alloys. *International Journal of Metalcasting*, *1*, 3140.

Smith, M., Levesque, J. B., Bichler, L., Sediako, D., Gholipour, J., & Wanjara, P. (2017). Residual stress analysis in linear friction welded in-service Inconel 718 superalloy via neutron diffraction and contour method approaches. *Materials Science and Engineering: A*, *691*, 168–179. https://doi.org/10.1016/j.msea.2017.03.038

Snapmaker. (n.d.). *Snapmaker Artisan 3-in-1 3D Printer*. Retrieved January 9, 2026, from https://snapmaker.com.tr/urunler/snapmaker-artisan-3-u-1-arada-yazici

Tabatabaeian, A., Ghasemi, A. R., Shokrieh, M. M., Marzbanrad, B., Baraheni, M., & Fotouhi, M. (2022). Residual stress in engineering materials: A review. In *Advanced Engineering Materials* (Vol. 24, Issue 3). John Wiley and Sons Inc. https://doi.org/10.1002/adem.202100786

Tarkun, D. (2015). *AlSi7Mg T6, AlSi7Mg ve AlSi11Mg alaşımlarının binek araç jant malzemesi olarak kullanılabilirliklerinin araştırılması* [Master's thesis]. İstanbul Teknik Üniversitesi.

The Aluminum Association, Inc. (2009). *International alloy designations and chemical composition limits for wrought aluminum and wrought aluminum alloys*. www.aluminum.org

Trebuna, F., Simcak, F., Bocko, J., Sarga, P., Trebuna, P., Pastor, M., & Mihok, J. (2008). Quantification of residual stresses in the weld by the hole-drilling method. *Metalurgija*, *2*(47), 133–137.

Vaz, C. R., Shoeninger Rauen, T. R., & Rojas Lezana, álvaro G. (2017). Sustainability and innovation in the automotive sector: A structured content analysis. *Sustainability*, *9*(6). https://doi.org/10.3390/su9060880

Vishay. (2005). *Surface preparation for strain gage bonding* (pp. 1–8). Vishay Micro-Measurements. www.vishaymg.com

Vuksanović, D., Asanović, V., Šćepanović, J., & Radonjić, D. (2021). Effect of chemical composition and T6 heat treatment on the mechanical properties and fracture behaviour of Al-Si alloys for IC engine components. *Journal of Mining and Metallurgy, Section B: Metallurgy*, *57*(2), 195–207. https://doi.org/10.2298/JMMB190510014V

Wang, H., Kim, D. K., Woo, W., Choi, S. H., Lee, S. Y., & Hwang, S. K. (2020). A new contour method for rapid evaluation of the cross-sectional residual stress distribution in complex geometries using a 3D scanner. *Journal of Mechanical Science and Technology*, *34*(5), 1989–1996. https://doi.org/10.1007/s12206-020-0420-0

Warmuzek, Małgorzata. (2015). *Aluminum-silicon casting alloys : atlas of microfractographs*. ASM International.

Williams, J. C., & Starke, E. A. (2003). Progress in structural materials for aerospace systems. *Acta Materialia*, *51*(19), 5775–5799. https://doi.org/10.1016/j.actamat.2003.08.023

Wong, W., & Hill, M. R. (2013). Superposition and destructive residual stress measurements. *Experimental Mechanics*, *53*(3), 339–344. https://doi.org/10.1007/s11340-012-9636-y

Wu, T., Tinkloh, S. R., Tröster, T., Zinn, W., & Niendorf, T. (2020). Determination and validation of residual stresses in CFRP/metal hybrid components using the incremental hole drilling method. *Journal of Composites Science*, *4*(3), 1–19. https://doi.org/10.3390/jcs4030143

Wyatt, J. E., Berry, J. T., & Williams, A. R. (2007). Residual stresses in aluminum castings. *Journal of Materials Processing Technology*, *191*(1–3), 170–173. https://doi.org/10.1016/j.jmatprotec.2007.03.018

Yang, H., Cui, Y., Qin, F., Lin, T., & Zheng, Y. (2025). Fatigue failure analysis and life prediction of forged 6061 aluminum alloy wheel hubs based on precipitate size effects and multiaxial stress modeling. *Engineering Failure Analysis*, *182*. https://doi.org/10.1016/j.engfailanal.2025.110181

Zanchini, M., Longhi, D., Mantovani, S., Puglisi, F., & Giacalone, M. (2023). Fatigue and failure analysis of aluminium and composite automotive wheel rims: Experimental and numerical investigation. *Engineering Failure Analysis*, *146*. https://doi.org/10.1016/j.engfailanal.2023.107064

Zhan, Y., Liu, C., Kong, X., & Lin, Z. (2017). Experiment and numerical simulation for laser ultrasonic measurement of residual stress. *Ultrasonics*, *73*, 271–276. https://doi.org/10.1016/j.ultras.2016.08.013